Dry and thermal processing of PEO-based solid electrolytes for all solid-state batteries

Vom Fachbereich Produktionstechnik

der

UNIVERSITÄT BREMEN

Zur Erlangung des Grades
Doktor der Ingenieurswissenschaften (Dr.-Ing.)
genehmigte

Dissertation

Katharina Platen, Master of Science

Gutachter: 1. Prof. Dr.-Ing. habil. Matthias Busse, Universität Bremen

2. Prof. Dr. rer. Nat. Bernd Mayer, Universität Bremen

Tag der mündlichen Prüfung: 17.12.2024

Danksagung

Diese Arbeit entstand während meiner Tätigkeit in der Arbeitsgruppe Elektrische Energiespeicher am Fraunhofer Institut für Fertigungstechnik und Angewandte Materialforschung (IFAM).

Ich möchte mich bei Prof. Dr.-Ing. habil. Matthias Busse dafür bedanken, dass ich die vorliegende Arbeit in der Arbeitsgruppe elektrische Energiespeicher am IFAM anfertigen konnte und für sein Gutachten dieser Arbeit.

Des Weiteren danke ich Prof. Dr. rer. Nat. Bernd Mayer für die Übernahme und Erstellung des zweiten Gutachtens.

Ich bedanke mich bei Dr. Frederieke Langer und Dr. Julian Schwenzel für die Bereitstellung dieses interessanten Themas. Ein besonderer Dank gilt Dr. Frederieke Langer für die kompetente Betreuung und fachlichen Unterstützung während der gesamten Zeit meiner Arbeit.

Den Kollegen der Arbeitsgruppe elektrische Energiespeicher des IFAMs danke ich für die Unterstützung und Diskussionsbereitschaft bei meinen experimentellen Arbeiten.

Ein besonderer Dank gilt meinen Eltern und meinen Geschwistern, die mich ermutigt haben, den Schritt der Promotion zu gehen und stets die richtigen Worte in jeder Situation gefunden haben. Mein letzter Dank gilt meiner Freundin Michelle für ihre liebevolle und motivierende Unterstützung zu jedem Zeitpunkt dieser Arbeit.

Kurzfassung

Die wachsende Weltbevölkerung und der damit zunehmende Energiebedarf sowie die Notwendigkeit Energie zu speichern, ist ein Prozess, der nicht aufhaltbar ist und dem sich Wissenschaft, Industrie und Politik gemeinsam stellen müssen. Das heißt, es müssen neue elektrische Energiespeicher entwickelt werden oder bestehende dahingehend optimiert werden, dass diese zukünftig den Energiebedarf decken können. Energiespeicher der nächsten Generation, wie zum Beispiel Festkörperbatterien, gewannen aufgrund ihrer hohen Energie- und Leistungsdichte in den letzten Jahrzehnten immer mehr an Aufmerksamkeit. Durch den Austausch des organischen, leichtflüchtigen Flüssigelektrolyten durch eine ionisch leitende Alternative wird nicht nur die Sicherheit dieser Batteriezelle erhöht, sondern auch die Umsetzung neuer Batteriedesigns, z.B. wie dem bipolaren Stapeln, ermöglicht. Festkörperelektrolyte können in drei Materialklassen unterteilt werden: Oxide, Sulfide und Polymere. Für alle drei Materialklassen wurden in der Vergangenheit viele Materialien hinsichtlich ihrer chemischen, strukturellen und elektrochemischen Eigenschaften untersucht. Obwohl vielversprechende Materialien für die einzelnen Materialklassen identifiziert wurden, ist die Materialverfügbarkeit sowie das geringe Wissen über deren Verarbeitung im großen Maßstab dafür verantwortlich, dass Festkörperbatterien noch nicht kommerzialisiert wurden. Anders als oxidische und sulfidische Materialien sind Polymere bereits im größeren Maßstab erhältlich. Somit kann der Fokus der Forschung stärker auf die Skalierbarkeit der Verarbeitung zu Festkörperelektrolyten gelegt werden. Darüber hinaus bieten Polymere ein weites Spektrum an lösemittelbasierten und lösemittelfreien Verarbeitungsmethoden. Aufgrund der einfachen Skalierbarkeit und der Möglichkeit der Trockenverarbeitung ist die Extrusion eine vielversprechende Verarbeitungsmethode.

Um die Beziehung zwischen Verarbeitung und Produktqualität besser verstehen zu können, wurde eine Vorgehensweise zur Untersuchung kleinerer Materialmengen über einen Laborkneter bis hin zu größeren Materialmengen über einen Doppelschneckenextruder entwickelt. Das in dieser Arbeit verwendete Polymer Poly(ethylenoxid) (PEO) ist eines der bekanntesten Polymersysteme für die Verwendung in einem polymerbasierten Festkörperelektrolyten.

Das verwendete Lithiumsalz ist Lithiumbis(trifluoromethylsulfonyl)imid (LiTFSI) und wird mit PEO in einem molaren Verhältnis von 20:1 (EO:Li) verarbeitet. Die durchgeführten Knetexperimente zeigen das sensitive Materialverhalten von PEO während thermischer und mechanischer Beanspruchung. Die maximale Verarbeitungstemperatur von 90 °C wurde durch Versuche bei unterschiedlichen Drehzahlen ermittelt danach degradiert das Polymer durch Kettenspaltung. Bei niedermolekularem PEO (M_w= 100 000 g mol^{-1}) gaben dabei die Prozessparameter Drehmoment und Massetemperatur nur Aufschluss über das Aufschmelzen des Polymers, jedoch nicht über das Degradationsverhalten. Die Degradation konnte durch Bestimmung der Kettenlänge mittels Gelpermeationschromatographie nachgewiesen werden. Die Sensitivität für die Degradation steigt mit zunehmendem Molekulargewicht. Sodass bei einem Molekulargewicht von 600 000 g mol^{-1} bereits anhand der Prozessparameter das Degradationsverhalten zu erkennen ist. Dies zeigte sich z.B. bei einer Drehzahl von 20 min^{-1} als starken Abfall von 19 % im Drehmoment und in einer starken Zunahme der Massetemperatur bis zu 160 °C. Für das Leitsalz konnten zwei Einflüsse identifiziert werden. Zum einen wirkt es als Weichmacher und zum anderen als Verstärker der Degradation von hochmolekularem PEO. Darüber hinaus werden auch die thermischen Eigenschaften von PEO und dessen Kristallinität durch Zugabe des Leitsalzes beeinflusst. Die mittels Differenzkaloremetrie ermittelten Glasübergänge verschob sich um bis zu 26 °C zu höheren Temperaturen. Des Weiteren ließ sich über diese Messmethode die Schmelzenthalphie und damit den Kristallisationsgrad bestimmen, der durch Zugabe des Leitsalzes von 70 % auf 28 % sank. Anhand der Polarisationsmikroskopie konnte die Größe der Sphärolithe und der Einfluss des Molekulargewichtes auf die Kristallgröße bestimmt werden. Dabei zeigte der PEO:LiTFSI-Elektrolyt mit niedermolekularem PEO Sphärolithe <10 µm deutlich kleinere als hochmolekulares PEO. Die Übertragbarkeit der Knetversuche auf den Doppelschneckenextruder wurde für niedermolekulares PEO als Ausgangsmaterial dargestellt, weil es weniger unter thermischer und mechanischer Beanspruchung degradiert. Mit Hilfe der Extrusionsversuche können Beziehungen zwischen Prozessparametern, wie die Wahl des Schneckenaufbaus und der Schneckengeschwindigkeit, und der Produktqualität untersucht werden. Sowohl die Extrusion der vorgemischten Pulver als auch die Extrusion mit der automatisierten und unabhängigen Materialzufuhr beider Pulver lieferten funktionsfähige PEO:LiTFSI-Elektrolyte, deren Leitfähigkeiten mittels elektrochemischer Impedanzspektroskopie im Bereich von 10^{-4} S cm^{-1} bei 80 °C ermittelt wurde. Vor allem der Schneckenaufbau beeinflusst dabei die Mischgüte des Elektrolyten. Hierbei zeigten der Schneckenaufbau mit Knetelementen für beide Extrusionsversuche die besten Ergebnisse.

Bereits die Prozessparameter Drehmoment und Druck zeigten den stabilsten Prozess mit einer Schwankung von bis zu <0.55 N m und <1 bar. Zur Bewertung der Durchmischung wurde eine Methode mittels Digitalmikroskopie und die Verwendung des RGB-Modells entwickelt. Auch hier zeigte der Schneckenaufbau B die beste Durchmischung mit den hellsten Elektrolyt-Strängen. Zur Bestimmung des Schmelzpunktes wurde eine Messmethode mittels dynamisch mechanischer Analyse entwickelt. Der ermittelte Schmelzpunkt sinkt im ersten Extruder-Setup von 65 °C auf 54 °C und im zweiten Extruder-Setup von 65 °C auf 43 °C. Auch die starke Abnahme des Schmelzpunktes zeigt die bessere Einarbeitung des Leitsalzes in die Polymermatrix durch die Knetelemente. Zusammenfassend kann aus den Ergebnissen der beiden Extrusionsversuche der Extrusionsprozess für einen Polymerelektrolyten auf Basis von PEO eines Molekulargewichtes von 100 000 g mol^{-1} und einer molaren Zusammensetzung von 20:1 (EO:Li) bei 90 °C für eine Schneckengeschwindigkeit von 15 rpm unter Verwendung von Knetelementen ausgelegt werden.

Abstract

The growing world population and the resulting increase in energy demand, as well as the need to store energy, is an unstoppable process that science, industry, and politics need to address together. This means that new electrical energy storage systems must be developed, or existing ones need to be optimized to meet future energy needs. Next-generation energy storage systems, such as all solid-state batteries (ASSBs), have attracted increasing attention in recent decades due to their high energy and power density. Replacing the organic, highly volatile liquid electrolyte with an ionically conductive alternative not only increases the safety of these battery cells, but also enables the implementation of new battery designs, such as bipolar stacking. Solid-state electrolytes can be divided into three classes of materials: oxides, sulfides, and polymers. For all three classes, many materials have been investigated in the past for their chemical, structural and electrochemical properties. Although promising materials have been identified for each material class, the availability of materials and the lack of knowledge on how to process them on a large scale are reasons why solid-state batteries have not yet been commercialized. In contrast to oxide and sulfide materials, polymers are already available on a large scale. This means that research can focus more on scalability for processing into solid state electrolytes. In addition, polymers offer a wide range of solvent-based and solvent-free processing methods. Extrusion is a promising processing method due to its easy scalability and the possibility of dry processing.

In order to better understand the relationship between production and product quality, a procedure is developed from the investigation of smaller material quantities using a laboratory kneader to larger material quantities using a twin-screw extruder. The polymer used in this work, poly (ethylene oxide) (PEO), is one of the best-known polymer systems for use in a polymer-based solid-state electrolyte. The lithium salt used was lithium bis(trifluoromethylsulfonyl)imide (LiTFSI) and was processed with PEO in a molar ratio of 20:1 (EO:Li). The kneading experiments show the sensitive material behavior of PEO under thermal and mechanical stress. The maximum processing temperature of 90 °C was determined by experiments at different kneading speeds, above which the polymer degrades by chain scission. In the case of low molecular weight PEO (M_w= 100,000 g mol^{-1}), the process parameters torque and melt temperature only provided information on the melting of the polymer, but not on the degradation behavior. Degradation could be detected by determining the chain length using gel permeation chromatography. The sensitivity to degradation increases with increasing molecular weight. At a molecular weight of

600,000 g mol^{-1}, degradation can already be seen in the process parameters. For example, at a kneading speed of 20 min^{-1}, the torque dropped by 19 % and the mass temperature increased up to 160 °C. Two effects of the conducting salt were identified. First, it acts as a plasticizer, and second, it enhances the degradation of high molecular weight PEO. In addition, the thermal properties of PEO and its crystallinity are also affected by the addition of the conducting salt. The glass transition temperatures determined by differential scanning calorimetry were shifted to higher temperatures by up to 26 °C. This method was also used to determine the melting enthalpy and thus the degree of crystallization, which decreased from 70 % to 28 % when the conducting salt was added. Polarization microscopy was used to determine the size of the spherulites and the influence of molecular weight on crystal size. The PEO:LiTFSI electrolyte with low molecular weight PEO showed spherulites <10 µm significantly smaller than the high molecular weight PEO. The transferability of the kneading experiments to the twin-screw extruder has been demonstrated for low molecular weight PEO as starting material because it degrades less under thermal and mechanical stress. The extrusion experiments are used to investigate relationships between process parameters, such as the choice of screw design and screw speed, and product quality. Both the extrusion of the premixed powders and the extrusion with automated and independent material feed of both powders yielded functional PEO:LiTFSI electrolytes whose conductivities were determined by electrochemical impedance spectroscopy in the range of $10^{-}4$ S cm^{-1} at 80 °C. In particular, the screw design influences the mixing quality of the electrolyte, with the screw design with kneading elements showing the best results for both extrusion experiments. The process parameters torque and pressure already showed the most stable process with a process error down to <0.55 N m and <1 bar, respectively. A method using digital microscopy and the RGB model was developed to evaluate the mixing. Again, screw design B showed the best mixing with the lightest electrolyte strings. A method using dynamic mechanical analysis measurement was developed to determine the melting point, which decreased from 65 °C to 54 °C in the first extruder setup and from 65 °C to 43 °C in the second extruder setup. The strong decrease of the melting point also shows the better incorporation of the conductive salt into the polymer matrix by the kneading elements. Overall, from the results of the two extrusion experiments, the extrusion process for a PEO-based solid-state electrolyte with a molecular weight of 100,000 g mol^{-1} and a molar ratio of 20:1 (EO:Li) at 90 °C can be designed using kneading elements at a screw speed of 15 rpm.

Table of Contents

Abbreviations and Symbols

aq.	aqueous
ASSB	All-solid-state battery
BMKW	German Federal Ministry of Economics and Climate Protection
BMW	German Federal Ministry for the Environment, Nature and Nuclear Safety
CPE	Composite polymer electrolyte
d	Polydispersity
d_o	Outer diameter
d_i	Inner diameter
DEC	Diethyl carbonate
D_{li}	Diffusion coefficient of lithium
DSC	Differential scanning calorimetry
EDX	Energy dispersive X-ray spectroscopy
EIS	Electrochemical impedance spectroscopy
exo	exothermic
GPC	Gel permeation chromatography
IFF	International Flavors & Fragrances Inc.
K	Crystallinity
KFT	Karl Fischer Titration
KSG	Federal Climate Protection Law

L/D	Length to diameter
LiTFSI	Lithiumbis(trifluoromethylsulfonyl)imide
LMP	Lithium Metal Polymer
Mn	Average molecular weight
M_w	Molecular weight
PEG	Poly (ethylene glycol)
PEO	Poly (ethylene oxide)
PEO100k	Poly(ethylene oxide) with a molecular weight of 100.000 g mol^{-1}
PEO600k	Poly(ethylene oxide) with a molecular weight of 600.000 g mol^{-1}
SE	Solid electrolyte
SEI	Solid electrolyte interface
SEM	Scanning electron microscopy
SPE	Solid polymer electrolytes
Tg	Glass transition temperature
T_m	Melting temperature
WSR	Water soluble resin

List of Figures

List of Tables

Introduction

There are approximately 8 billion people in the world today. By 2050, the world's population is expected to grow to 9.7 billion [1]. Consequently. the demand for energy will also increase (48 % in 2050) [2]. Currently, 80 % of the world's energy needs are met by fossil fuels [2]. In addition, the energy demand from stationary storage is estimated to reach 100 GWh in 2030 and even 180 GWh in 2045 [3]. Mobile storage, such as EVs, has a demand of 130 – 160 GWh (2020) [4]. It is time for industry, politics, and science to work together to find new ways to meet the energy needs in a sustainable way. The need to meet energy demand is demonstrated by the rethinking of climate policy in Germany. In 2021, the German Bundestag passed a new Federal Climate Protection Law (KSG) that enhances Germany's greenhouse gas reduction target for 2030 to minus 65 % compared to 1990. By 2040, the target must be reduced to 88 % in order to achieve partial carbon neutrality by 2045. The new KSG will also provide € 8 billion for climate change mitigation, of which € 6.5 billion will go to industry, energy and buildings [5]. In this context, the German Federal Ministry of Economics and Climate Protection (BMWK) and the German Federal Ministry for the Environment, Nature Conservation and Nuclear Safety (BMW) have developed a new funding guideline "Electric Mobility", which aims to strengthen cooperation and the contribution of research and development (R&D) [6]. The R&D projects are intended to fundamentally develop the energy and climate-policy potential of e-mobility and contribute to strengthening the competitive position of German industrial sectors, taking into account the goal of reducing transport-related CO_2 emissions by 42 % by 2030 through the use of EVs. In order to achieve this goal, the government will also provide subsidies to consumers, which will only apply to pure EVs from 2023, in order to make the purchase of such vehicles more lucrative [7]. The most valuable component in an EV is its battery. The German government's goal is to locate battery cell production in Germany and Europe to be less dependent on third countries. The battery cells “Made in Germany“ [8] should have the following properties:

- high energy density and performance at competitive prices,
- a long service life and a high number of charging cycles, and
- sustainable and environmentally responsible production and disposal.

In order to lay the foundation stone for a battery cell "Made in Germany", the Swedish company Northvolt, among others, is being supported in the construction of a gigafactory in Heide. This gigafactory promises an annual production volume of 60 GWh [9]. In addition,

the European Battery Alliance estimates the market potential for automotive batteries produced in Europe at up to € 250 billion by the middle of the next decade [8].

The battery cells currently used in EVs are lithium-ion batteries (LIB) with liquid organic electrolytes. Conventional LIBs offer a gravimetric energy density of 260 Wh kg^{-1} and will reach their physiochemical limit in the future [10]. In addition, the liquid, volatile and flammable electrolyte is an environmental and safety risk factor. This is motivating research and industry to look for suitable alternatives that will not only offer better performance in the future, but also higher safety in their application and environmentally friendly production. One such alternative is the all-solid-state battery (ASSB).

The ASSB is the next generation technology, where the classical liquid electrolyte is replaced with an ion-conducting solid. The solid electrolyte (SE), which is a component of the ASSB, not only provides a path for ion migration from electrodes, but it also separates the electrodes to avoid short circuit [11]. The SE seems to be promised to suppress Li dendrite formation due to its mechanical stability [10,12,13]. This offers the use of metallic Li as anode, which leads to a higher capacity and cell voltage than conventional LIBs. In addition, the use of SE offers the possibility of new cell designs, such as bipolar stacking. This improves the gravimetric and volumetric energy density compared to conventional LIBs due to less inactive materials, i.e. cell housing. In general, the SE materials are classified into organic (polymers) and ceramics (oxides and sulfides). The current challenge is to scale up the production and manufacturing process of the SE. While the manufacturing technologies for the anode and the cathode materials of conventional LIBs can be adapted to ASSBs, suitable manufacturing technologies must be found to processed in large quantities while maintaining the SE properties (mechanical strength). This is essential for successful commercialization of ASSBs and to replace LIBs in the future. While the material availability in case of oxide and sulfide materials is still an issue to overcome, the little knowledge of scaled production routes still hinders the commercialization of ASSBs. Polymers are already available in larger quantities but are also promised to improve the safety of the battery cell, due their nonvolatile and less flammable material properties [14]. In addition, polymers provide a malleable and elastic nature and are able to compensate large volume changes in the active materials in the electrodes during discharging and charging [15]. In general, there are two main issues to consider for successful upscaling: the manufacturability and the costs [16]. Polymer electrolytes show a wide range of processing techniques, that are divided in general into solvent-based and solvent-free production. Typical solvent-based techniques are solution

casting [11,17–23], spin-coating [11], tape casting [11], screen printing [11] and dip-coating [11]. These solvent-based techniques have drawbacks that make them unfavorable for industrial production. Firstly, there is many processing steps required, such as the pre-mixing of the components, the preparation of a homogenous slurry and a drying step to remove the toxic and hazardous solvent. Secondly, the residual solvents can have a negative effect on the electrochemical performance of the SE [24]. Reducing or even eliminating the use of solvents offers great potential for improving the entire process, both economically and environmentally. Therefore, solvent-free processing techniques, like hot-pressing [11,25–27] and extrusion [28–30] are desired.

For SEs to have a chance to replace conventional liquid electrolytes and thus drive ASSB production, the shift from fundamental research to production should now occur. Thus, now the focus of well investigated SEs needs to be taken on their production in larger scale while maintaining their properties. For the thermal processing of polymer-based SEs, thermoplastic properties are required. One of the most studied polymer for SE is the thermoplastic poly(ethylene oxide) (PEO) [31–35]. PEO has a melting temperature (T_m) around 65 °C depending on the molecular weight (M_w) [36]. Furthermore, PEO has the ability to dissolve alkali metal salts, such as lithium bis(trifluoromethylsulfonyl)imide (LiTFSI), forming a (PEO)-Li-salt complex [37]. Therefore, the effect of process parameters on the properties of PEO-based SEs needs to be more investigated. As known from literature LiTFSI has an effect on the thermal properties and crystallization behavior of PEO [31,33,34,38]. In case of thermal processing, LiTFSI acts as plasticizer that enhances flowability of PEO.

The solvent-free processing technique is already implemented industrially. The Japanese company APB Corporation, founded in 2018, presented an “All Polymer Battery”, where even the metal current collector is replaced by a polymeric material, and which is the first large-area bipolarly stacked battery [39]. The used processing technique is powder coating [40]. In addition, the French company Blue Solutions S.A.S from Bolloré also successfully implemented their solvent-free processing technique in industrial scale. They commercialized an ASSB (Blue Solutions’ LMP®) based on lithium metal foil as anode, solid electrolyte consisting of polyethylene oxide (PEO) and a lithium salt and a $LiFePO_4$-cathode [41]. For all three battery components the extrusion process is used [42].

Aim

Despite the successful implementation and commercialization of this polymer-based ASSB, little is known scientifically about the process itself and its effects, or about the SE.

Thus, the aim of this thesis is therefore to investigate the relationship between the dry process of polymer-based SEs using melt extrusion and the material behavior with respect to the upscaling of polymer-based SEs. Therefore, a concept is developed from the investigation of small quantities using a laboratory kneader to the investigation of larger quantities in kilo-scale using a twin-screw extruder. The knowledge gained from this thesis should allow the concept to be applied to other systems in the future, such as the production of composite cathodes.

This thesis is divided into three parts. In the first part, the principals of LIBs and ASSBs are presented. The main focus is on polymer-based SE and their production. In particular, the extrusion process is explained, which is the basis for the following chapters. In the second part of the thesis the experimental setup is explained. In addition to the sample preparation and the characterization methods used in this thesis, the performance of the kneading and extrusion experiments is also described. The third part is divided into three sections. The first section deals with the kneading experiments performed to determine the polymer and the processing window for the extrusion process. For this purpose, two different molecular weights (M_w) of PEO are investigated for their thermal stability during kneading and the influence of the conducting salt (LiTFSI) on the thermal processing. The knowledge gained from the kneading experiments is then transferred to the extrusion experiments (section two and three). Several influences on product quality are investigated. Firstly, the influence of screw geometry and screw speed on process and product quality was investigated. Secondly, the influence of material addition to the process was evaluated. Therefore, the extrusion experiments of a premixed PEO:LiTFSI powder batch in a molar ratio of 20:1 (EO:Li) are compared with the extrusion of PEO and LiTFSI powders through two feeders. The thesis concludes with a summary of the results and an outlook for future work.

I Theory and state of research

1. Secondary batteries based on Lithium-ions

1.1 Lithium-ion batteries

LIBs have become an indispensable part of modern life. Since the 1990s, LIBs are a constant companion in mobile consumer devices, such as mobile phones and notebooks, but also battery power tools. Today, LIBs become important in their key role for electric mobility (e-bikes or EVs). In general, there are two types of existing LIBs. The primary battery, a battery that can only be discharged once, and the secondary battery, a battery that is rechargeable. So, the reactions that take place in the cell during discharge are reversible. The first primary, non-aqueous LIB using Lithium-manganese oxide ($LiMnO_2$) was commercialized by Sanyo company in the 1970s [43]. In the early 1980s, research began to develop and understand the function of lithium intercalation processes in different materials. That was the starting point of secondary LIB. In 1985, the first rechargeable LIB with an energy density of 60 – 65 Wh kg^{-1} at a discharge rate of C/3 (800 mA) was developed by MOLICEL® (Moli Energy Ltd. (Canada)) using Li metal anode and Molybdenum disulfide cathode [44,45]. However, these batteries exhibited safety problems due to dendrite formation on the anode side. Increasing research in the field of intercalation materials for anode and cathode has helped to overcome these problems. In 1973, *GOODENOUGH et al.* first proposed lithium cobalt oxide ($LiCoO_2$) as cathode material (3.9 V vs. Li^+/Li) that is later patented [46]. About the same time *ARMAND* and co-workers found out that polymer electrolytes allow the use of graphite (C_6) as intercalated anode material. The use of intercalating materials on both electrode sides lead to the first commercialization of LIB by Sony, in 1991 [43].

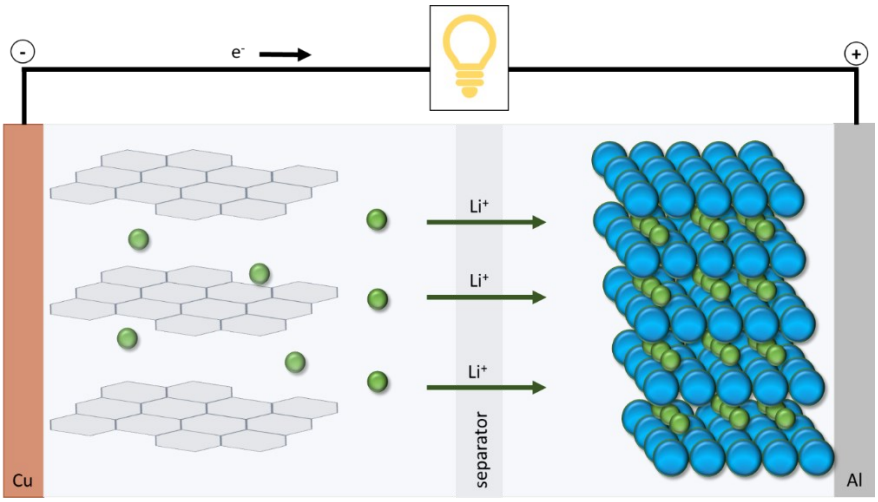

Figure 1: Scheme of LIB cell using LCO as cathode, liquid electrolyte, and graphite as anode during discharge process showing Li-ions migration and electron flow from the anode to the cathode.

Figure 1 shows the typical structure of this battery. In general, it consists of graphite as intercalating anode, a liquid electrolyte ($LiPF_6$ in propylene carbonate and diethyl carbonate (PC:DEC, 1:1) and layered $LiCoO_2$ (LCO) as Li intercalation cathode [43]. A microporous separator prevents the direct contact between the anode and the cathode and by that a short circuit of the cell. Current collectors for this type of battery are aluminum metal for the cathode and copper metal for the anode.

The operating principle of such a battery is describe as follows: during discharge, Li-ions de-intercalate from the graphite anode (negative electrode) and migrate through the electrolyte to the cathode (positive electrode), where they are intercalated by the active materials. At the same time, electrons flow over an external circuit from the negative to the positive electrode generating current. During charging, this process is exactly reversed, with Li-ions migrating from the cathode to the anode. This principle is also known as “rocking chair” principle.

$$Li_{1-x}CoO_2 + Li_xC_6 \underset{charge}{\overset{discharge}{\rightleftharpoons}} LiCoO_2 + C_6 \qquad (1.1)$$

Today’s LIBs reach energy densities of 665 - 770 Wh l^{-1} and 260 - 265 Wh kg^{-1} for volumetric and gravimetric energy densities, respectively [10,47].

Anode:

The use of intercalating graphite as anode material is still state of the art due to the formation of Lithium dendrites when Li metal is used. The reaction that happens during discharge is defined as follows [48]:

$$LiC_6 \rightarrow Li^+ + e^- + 6C \quad (1.2)$$

The maintaining stability of graphite in the absence of Li allows almost complete discharge. Furthermore, it is cheap and relatively light reaching theoretical capacity of 372 mA h g^{-1} [49]. However, it is just a fraction of the capacity that is reached with Li (3860 mA h g^{-1}). Another drawback is the formation of a solid electrolyte interface (SEI) during the first charge due to a side reaction of graphite and the electrolyte. This leads to capacity loss and reduces the lifetime of LIBs. Alternative materials for anodes are lithium titanium oxide ($Li_4Ti_5O_{12}$ / LTO), tin (Sn-) or silicon (Si-) composites. LTO is also known as a "zero strain" material showing almost no volume change during the de-/intercalation of lithium. LTO shows superior thermal stability and is used for high power application, whereas it is already commercialized. Due to its high potential of ~1.55 V vs. Li/Li^+ and low capacity of 175 mA h g^{-1} the energy density stays low [49]. Despite some advantages of Sn- and Si-composite anodes such as high theoretical capacity and proper operating window, the drawback of very large volume changes during cycling prevail, which limits the cycle life and hinders their commercialization [50].

Electrolyte and separator:

The electrolyte is an important component of a LIB without which Li-ion transport is not possible. Electrolytes must provide a good ionic conductivity and at the same time be electronic insulator. The standard material, that is used for example for the LCO-cell from Sony, is a liquid electrolyte consisting of a lithium salt ($LiPF_6$) dissolved in organic carbonate solvents like EC, DEC, DMC or PC [51–55]. The use of volatile and flammable liquid organic solvents has some safety concerns. Further, $LiPF_6$ can react with atmospheric moisture or water residues in the electrolytes forming poisonous and corrosive hydrofluoric acid (HF) [56]. The separator of a LIB is a microporous membrane that has the function to prevent direct contact between the anode and cathode so that no short circuits occur. The separator must also allow the diffusion of Li-ion. A typical thickness of the separator is around 15 – 30 µm [44] and materials that are used are for example non-woven polypropylene

(SAFT, France) or cellulosic separator, such as filter paper and Celgard® separator of porous propylene (Honeywell, USA and P.R. Mallory and Co. Inc., USA) [43].

Cathode:

In general, a cathode of LIB consists of active material, carbon, and polymer binders (e.g., PVDF). The active materials of a cathode are electronic insulators, so carbon is needed as an electron conductor. Cathode materials are divided into two groups: conversion materials and transition metal oxide intercalation materials. The latter material group is considered in more detail below. Layered LCO has been one of the most widely used active materials for cathodes since its introduction by Sony. Drawback of LCO is that only 50 % of lithium can be used due to stability issues of the crystal that can lead to oxidation processes with the electrolyte and thermal runaway. The reaction during discharge is describe as follow:

$$2Li_{0.5}CoO_2 + Li^+ + e^- \rightarrow 2LiCoO_2 \quad (1.3)$$

The development of battery research toward large scale and high-power application makes the research and further development of other intercalating materials for cathodes indispensable.

Depending on the crystal structure of the active material the Li^+ diffusion occurs in different dimensions. Olivine type materials like lithium iron phosphate ($LiFePO_4$, LFP), with a theoretic specific capacity of 170 mA h g^{-1}, have 1D channels for Li^+ diffusion. LFP has remarkable thermal stability, a good compatibility with many electrolytes, no O_2 evolution and there is no health risk. However, LFP has low ionic conductivity and small redox potential against lithium (3.5 V vs. Li^+/Li). The above mentioned layered LCO (theoretical specific capacity of 274 mA h g^{-1}) provide 2D Li^+ diffusion. 3D conductors are spinel type materials like lithium manganese oxide ($LiMn_2O_4$, LMO) with a theoretical specific capacity of 181 mA h g^{-1}. Although LMO can be discharged with high current (> 5 C) and shows a high potential (4.7 V vs. Li^+/Li), it performs very badly during cycling showing a constant loss in capacity, especially at temperature above 50 °C. The diffusion property of the active material defines the cathode performance and is characterized by its diffusion coefficient (D_{Li}). A high volumetric energy density can be reached with high D_{Li} since fewer additive materials, such as carbon as an electron conductor, are needed due to larger particle size of active materials.

1.2 All solid-state Batteries

The present increasing demand and requirements on energy supply regarding EVs push conventional LIBs to its limits. As already mentioned, state-of-the-art LIBs reach their limit in gravimetric energy density with 265 $Wh\,kg^{-1}$ [47]. That is quite low compared to the gravimetric energy density of a fuel cell that reaches 1000 $Wh\,kg^{-1}$ [57]. To remain competitive LIBs and especially their energy density needs to be improved. In addition to their limited energy density, other drawbacks related to safety issues play a crucial role in the need to improve LIBs. Liquid electrolytes are flammable, and they are susceptible to react with the electrode material affecting the cell performance and its lifetime. While the use of lithium metal as anode improves the cell performance and thus its competitiveness with fuel cells, the reactivity of the liquid electrolyte with lithium metal, which forms irreversible dendrites, still prevents its use. The dendrites can grow uncontrollably through the electrolyte. A critical size is reached when dendrites penetrate the separator and touch the cathode, resulting in a short-circuit.

Many approaches have been undertaken to enable the use of lithium metal as anode material. One of these approaches is shown in Figure 2. ASSB is a new generation battery technology where the liquid electrolyte is replaced with an ion-conducting solid, the so-called solid electrolyte (SE). Using SE makes the battery completely solid. Typical components used as SE are classified into three groups: polymers, sulfides, and oxides. These organic and inorganic material replace both the liquid electrolyte providing the path for ion migration from the electrodes and the porous separator avoiding short-circuit [11]. Compared to liquid electrolytes SEs have a higher mechanical stability and are believed to suppress Li dendrite formation [10,12,13]. The use of lithium metal as anode leads to a battery with a higher capacity and cell voltage than conventional batteries. In addition, the use of non-volatile and less flammable materials as SE improves the safety of such a battery. There is no problem with leakage when the battery gets damaged, and no following burning of the battery. Further, the working window is larger than of liquid electrolytes due to no phase transition of the solid material. One major drawback of ASSBs is their low ionic conductivity compared to conventional LIBs.

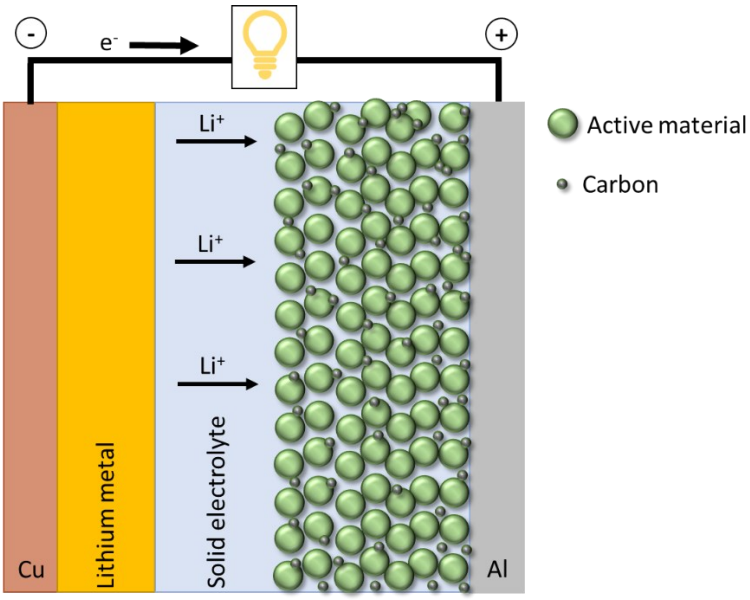

Figure 2: Scheme of ASSB cell with lithium metal as anode, solid electrolyte and composite cathode during discharge process showing Li^+ migration and electron flow from the anode to the cathode.

Another challenge with ASSB is the interfacial contact of the components. Whereas conventional LIBs provide a good contact between the cathode and liquid electrolyte because the electrolyte can easily penetrate the porous cathode material. The use of only solid components makes this contact challenging. To improve the interfacial contact between both materials, a composite cathode of cathode materials and SE as catholyte seems to be promising. For use as a catholyte, the solid electrolyte must be electrochemically stable with respect to the active material of the cathode. In selecting the components for the composite cathode, care has been taken to ensure that no chemical or electrochemical reaction of the components occurs during the manufacture or use. In general, to achieve a high volumetric energy density, the solid content of inactive material such as SE, pores, and carbon black is kept as low as possible. In general, cathodes for LIBs are produced using slurry-based methods such as doctor blading, dried and then calendered to reduce the overall porosity of the cathode. During the cell assembly, the cathode is then infiltrated with the liquid electrolyte, which penetrates through the pores of the cathode and ensures good contact with the active materials. Conversely, for composite cathodes with a polymeric SE, the SE must be added during the cathode production since the SE also functions as a binder and an ionic conductor. In the best case, the composite cathode produced does not have pores. The use of a thermoplastic polymer as a catholyte allows the above-mentioned solvent-based production method to be replaced by a solvent-free method, such as extrusion. For PEO-based systems for example, LFP is the preferred active material because its voltage plateau of 3.4 V against

lithium is below the decomposition voltage of the polymer electrolyte (3.8 V vs. Li/Li^+ [58–60]).

2. Solid-state electrolytes

This chapter describes the requirements that SEs must meet for use in ASSBs to be competitive with conventional LIBs and to have the chance to even replace them in the future. The focus of this work is on polymer-based SEs, which are describe in detail in chapter 2.1.

In general, to be used as SE materials, the materials must not only be available, cost-effective, and environmentally benign, but also provide **ionic conductivity** ($\sigma_{Li} > ^{10^{-4}}$ S cm^{-1}, [61]) for the transport of Li-ions during the discharging and charging over the operation temperature range of a battery cell (-40 < T < 60 °C, [61]). At the same time these materials must be **electronically insulating** ($\sigma_e < 10^{-10}$ S cm^{-1}, [61]) to prevent short circuit. To avoid any side reaction during the use of the battery, the electrolyte materials must be **chemically stable** against the other battery components (anode and cathode). Further, the materials must have a good **mechanical stability** to compensate volume changes of the active materials during charge and discharge. Further, it is suggested that the **shear modulus** of the SE material has to be twice the shear modulus of Li (G= 4.2 GPa, [62]) to suppress Li dendrite growth. In addition, battery cells with high voltage cathodes and Li metal with high operating voltages make a **wide electrochemical window** (up to 5 V) necessary to avoid electrolyte degradation. Due to temperature changes during operation and production the **thermal properties** of SE materials are also an important material property that must be considered for the use as SE material. To ensure good interfacial contact between SE and cathode or anode during use, the thermal expansion coefficient should be compatible with each other. Otherwise, fracture or loss of contact may occur at the interfaces. To maintain material properties during the battery operation, SE materials should be thermally stable in the operating temperature range. In addition to all the mentioned material properties, SE material must **improve the safety** of the working battery cell by being non-flammable and non-explosive, have a **low toxicity** and most importantly **be producible** on larger scale to be competitive with conventional LIBs.

Inorganic materials such as oxides and sulfides are promising SE materials that are believed to meet the above-mentioned requirements for the use in ASSBs. Oxide materials are a promising material class due to their high shear modulus (up to 7.3 higher than Li, [63]) and their high chemical, electrochemical and thermal stability. Due to their rigid and brittle bodies, they have a nonflexible nature leading to a poor interfacial contact with the electrode material. Oxide materials reach Li-ion conductivity up to 10^{-3} S cm^{-1} under ambient temperature [13]. Oxide electrolytes are roughly divided into two groups: crystalline group

(NASICON-(LAGP, LATP), perovskite- (LLTO) and garnet-type (LLZO) electrolytes) and amorphous/glass group ($Li_2O–MO_x$ (M= Si, B, P, etc.) and LiPON) [64]. A major drawback to why oxide materials have not yet found their way to industrialization is the high cost for large-scale production.

In contrast to oxides, sulfidic materials show a high chemical reactivity with the electrode materials and behave sensitive towards moisture generating harmful H_2S gas. Further, they only provide a narrow electrochemical window. Nevertheless, they reach Li-ionic conductivity up to 10^{-2} S cm^{-1} at ambient temperature due to its easy densification. Sulfidic materials provide also good interfacial contact to the electrode materials. But grain boundaries are still an issue that can lead to a decrease in Li-ionic conductivity [13]. The most famous sulfidic materials are $L_{10}GeP_2S_{12}$ (LGPS) and $Li_9P_3S_{12}$ (LPS) [65]. The industrialization of sulfide-based electrolytes has not yet been realized due to their low availability and the associated high raw material prices.

2.1 Polymer-based solid electrolytes

Polymer-based solid electrolytes are a promising material group, which was first discovered by FENTON and co-workers in 1973 [37] and recently gained much attention over the last years, especially due to their high capability of large-scale production. Further beneficial features of polymer-based SE are the design and size flexibility, the improvement of safety due to leakage prevention, fire resistance and automatic extinction, high reliability for impact and vibration and improvement of cyclicity due to the decrease of the interfacial impedance of the electrode and the electrolyte [66]. Polymer-based SEs can be classified in five groups depending on their physical conditions [67]:

1. **Conventional polymer-salt complex or dry polymer-based SE:** This type of polymer electrolyte consists of a mixture where polar polymer participates by the solvation of ionic salt by complexation. Examples of high molecular weight polymers with the capability of dissolving ionic salts are poly (ethylene oxide) (PEO) and poly (propylene oxide) PPO [68,69]. They are generally prepared by conventional solution casting or hot-press technique. The PEO-based SE is more described in detail in the following chapter 2.1.2.
2. **Plasticized polymer-salt complex:** These polymer-based SEs are modified by the addition of liquid plasticizers, like low molecular weight poly (ethylene glycol) (PEG)

[70,71] or dimethyl sulfoxide (DMSO) [72,73] to improve the ionic conductivity by decreasing the crystallinity of the polymer host. Drawback is the loss in mechanical strength and in the chemical stability against the electrode material (anode).

3. **Polymer gel electrolyte:** Compared to the plasticized polymer-salt complex, polymer gel electrolytes have a large amount of organic solvent or plasticizer forming a stable gel. Typical polymer hosts are PEO [74,75], poly (vinylidene fluoride) (PVDF) [76,77], poly (acrylonitrile) (PAN) [78] and poly (methyl methacrylate) (PMMA) [79–81] using low-evaporating solvents, like ethylene carbonate (EC) [77,79,82], propylene carbonate (PC) [77,79], etc., as plasticizers. Benefits and drawbacks are like that of plasticized polymer-salt complex.
4. **Rubbery electrolyte:** This polymer-based SE differs in the mixing ratio of polymer to salt. Here a large amount of salt is mixed with a small amount of polymer providing a low glass transition temperature to maintain rubbery state at room temperature [83]. Beside using a large amount of salt, synthetic rubbers can be used to provide the rubbery state [84–86].
5. **Composite polymer electrolyte (CPE):** CPEs are a two-phase composite solid electrolyte system. A small fraction of micro/nano-size inorganic/organic filler particle (Al_2O_3 [87], SiO_2 [88] or TiO_2 [89]) is dispersed into the polymer host. The modification by filler particle enhances the ionic conductivity, the mechanical stability, and the interface activity [90].

Typical Li-salts for polymer electrolytes are LiX, with X= ClO_4, CF_3SO_3, BF_4, AsF_6, $C_2NO_4F_6S_2$ etc. [33,34,67,91,92].

2.1.1 Li-ion transport mechanism in polymer-based solid electrolytes

In the previously mentioned polymer electrolyte systems, where the polymer host can dissociate lithium salts, Li-ion transport occurs within the amorphous region of the polymer. PEO-based SEs are due to their ability to dissolve a variety of metal ions, one of the most investigated polymer-based SE-system. The Li-ion transport mechanisms in PEO-based SEs are well described [93–95]. BRUCE and co-workers found that PEO shows a helical structure with repeating units of seven monomer groups in two turns of the helix [96]. During the complexation, Li^+ is wrapped by PEO chains and coordinates with three ether oxygens from the polymer chain [97,98]. Li-ion transport mechanism in PEO-based SEs is a combination of intra and inter segmental Li^+ hopping [99]. While Li-ions move along the polymer chain in

intra segmental Li^+ hopping, Li-ions are transported by jumping from one polymer segment to another in inter segmental Li^+ hopping, as shown in Figure 3.

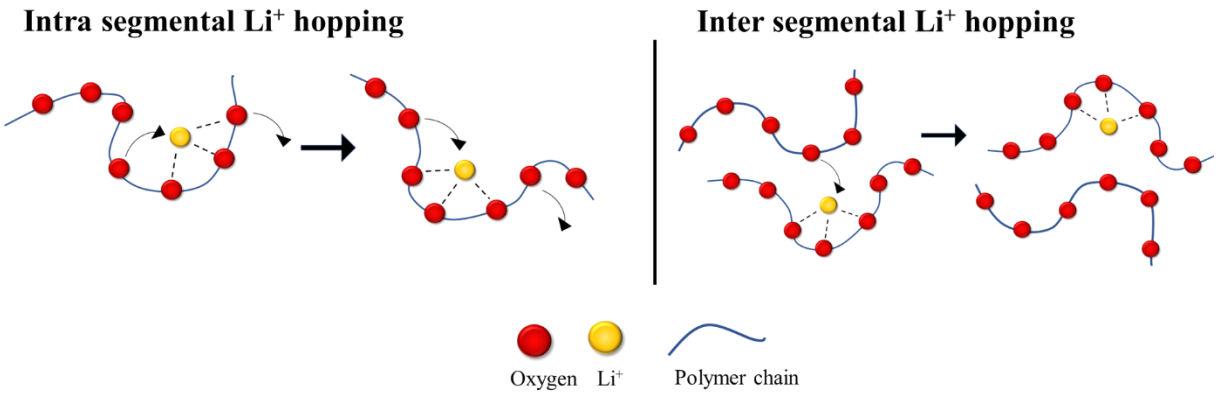

Figure 3: Scheme of Li^+ transport in polymer electrolyte exemplary for PEO-LiX-electrolyte, Li^+ hopping along the PEO segment (left) and Li^+ hopping from one PEO segment to another (right); inspired by [93].

The motion of polymer chains and by that the Li^+ mobility within the polymer chains is strongly affected by:

- molecular weight of the polymer,
- glass transition temperature (T_g),
- degree of crystallinity,
- functional side-groups within the polymer unit and
- choice and concentration of Lithium salt.

Furthermore, the ion mobility within the polymer chain can be influenced by solvent residuals. On the one hand, these residuals act as a plasticizer improving the polymer chain mobility. And on the other hand, the greater affinity of Li^+ to polar solvents increases the ion mobility within the polymer matrix [24]. Since the electrochemical properties are affected by solvent residues e.g., water, it is important prepare the sample carefully by drying before use. Moreover, a solvent-free processing method prevents a misinterpretation of the electrochemical properties and eliminates a costly drying step after production.

2.1.2 Poly (ethylene oxide)-based electrolytes

Within the scope of this work, dry polymer-based SE, and the potential for upscaling its processing is considered. The famous polymeric material for research works with regard to electrochemical properties and performance for the use as a polymer-based SE is the polyether poly (ethylene oxide) (PEO), which has the property of dissolving various alkali

salts [37]. The melting temperature (T_m) of PEO is around 65 °C depending on its molecular weight [100]. There are already a number of lithium salts that have been investigated as conductive salt for PEO-based SEs, such as Lithium perchlorate ($LiClO_4$) [101], Lithium bis(trifluoromethanesulfonyl)imide ($LiN(CF_3SO_2)_2$, LiTFSI) [33,34], Lithium hexafluorophosphate ($LiPF_6$) [102–104], Lithium tetrafluoroborate ($LiBF_4$) [105,106], Lithium bis(pentafluoroethanesulfonyl)imide ($Li[N(SO_2C_2F_5)_2]$, LiBETI) [107–110] and Lithium triflate ($LiCF_3SO_3$, LiTf) [111] due to their highly de-located negative charge. Moreover, due to their low lattice energies they are easy to dissolve. The Li-salt concentration of PEO-based SE is generally referred to as a ratio n of ethylene oxide (EO) monomer units to Li-ions. Generally, it is described as $P(EO)_nLiX$ (X= anion) or EO:Li. The optimum lithium salt concentration to achieve the best ionic conductivity depends on the used lithium salt [111].

The most extensively studied lithium salt is LiTFSI due to the high flexibility of the anion, which reduces the crystallinity of PEO. The highly delocalized charge distribution of $TFSI^-$ increases the dissociation and solubility. Further, it increases the stability of SE due to its excellent thermal, chemical and electrochemical stability [33]. PEO-LiTFSI electrolytes reach a moderately high ionic conductivity of $(4 \pm 2) \times 10^{-4}$ S cm^{-1} at 60 °C. The ionic conductivity highly depends on M_w of PEO. While lower M_w PEO has high ionic conductivity, its mechanical strength suffers due to short polymer chains making it unsuitable for use as SE. At M_w greater than 2×10^3 g mol^{-1}, the ionic conductivity becomes independent of the polymer chain lengths [94]. Hence, it is always a trade-off between sufficiently high ionic conductivity and the required mechanical strength for application as SE. Research efforts have been made to improve both the ionic conductivity and the mechanical stability of the polymer electrolytes. This improvement can be achieved by co-polymerization [112,113], blending [18,114], cross-linking [115] or formation of composite systems [109,116–122]. By adding ceramic fillers such as SiO_2 [109,118,122] or Al_2O_3 [119,120] to the composite systems, the mechanical strength of the SPE can be improved.

3. Production of all-solid-state batteries

Due to their promising performance, commercialization of ASSBs is still an important aspect that research and industry are intensively working on. While ASSBs components are readily produced at laboratory or pilot scale, the missing knowledge about their series production makes it difficult to upscale their production and implement defined process chains. Further, the production chain of ASSBs highly depends on the solid electrolyte material. As shown in Figure 4, the production of ASSBs can generally be divided into three sections: electrode and electrolyte production, cell assembling and cell finalization [123].

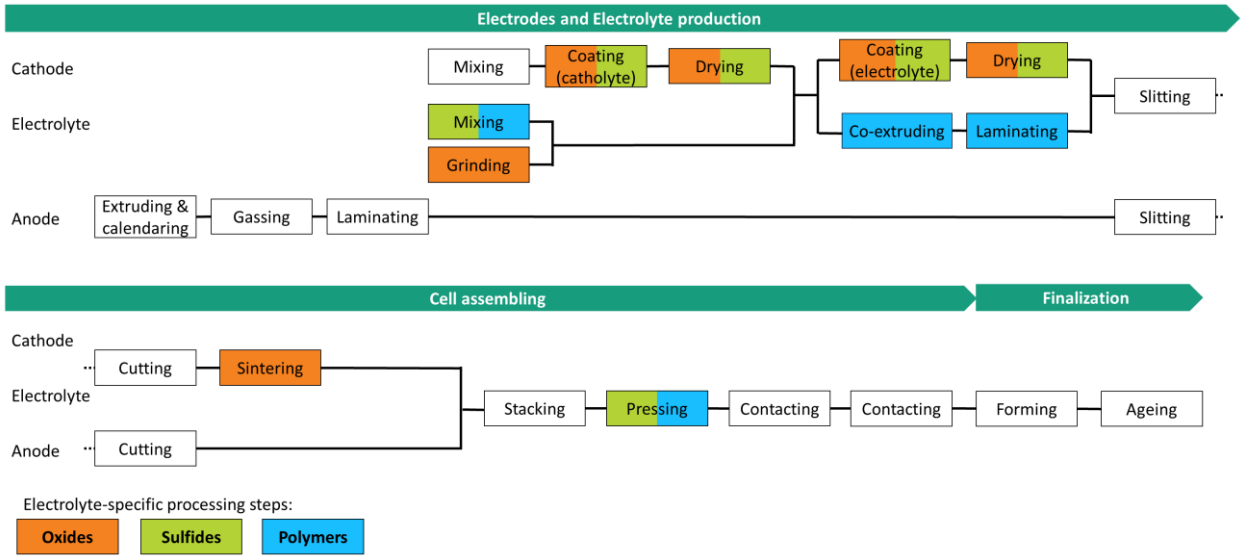

Figure 4: Flow chart of ASSB production under consideration of electrolyte-specific processing steps; inspired by [123].

Beside the manufacturability of the ASSB components, the production costs play an important role to make ASSBs competitive. The use of reactive and hygroscopic materials makes it necessary that a multitude of the process steps need to be carried out in an inert atmosphere (> 13,000 US$ m^{-3} [124]) or under dry room conditions (~2,000 US$ m^{-3} [124]).

Further, the use of Li metal as anode material increases raw material cost to about 50 – 130 $ kg^{-1} compared to natural graphite (8 – 11 US$ kg^{-1}) [125]. In general, Li metal anode is produced by extrusion with subsequent rolling process to define the surface roughness and thickness of the metal foil. The lamination with the current collector can be performed in a dry room by applying an additional passivating layer [123,124]. In addition, also the processing costs will increase. Slicing methods used for graphite anodes, such as

mechanical cutting, cannot be used for lithium metal and must be replaced with more expensive laser cutting.

As presented in Figure 4 the production of the electrolyte and further production steps, such as the joining of the cathode and electrolyte during component production, as well as steps during the cell assembly, such as the sintering of the oxidic materials or necessary pressing of polymeric or sulfidic ASSB cells, depend on the material used. This work focuses on the production of polymer-based SE, which will be briefly discussed in chapter 3.1.

Compared to the anode production, the cathode and electrolyte production requires more process steps depending on the electrolyte material. The most important processing step, which has a decisive effect on the cell performance, is the mixing of the components [124]. The mixing process can be performed solvent-based by mixing slurries with a planetary batch mixer or dry using a ball mill. The main difference is that for oxides this step can be carried out in ambient environment, while for sulfides a dry or an inert environment is required due to the possible generation of harmful H_2S with water in air [126–130].

After mixing, the cathode slurry is coated onto an aluminum foil. The next step is to coat the electrolyte on top of the cathode to form a cathode-separator assembly that can be calendered and slit after drying [124]. For the drying of oxide-electrolytes, care must be taken when selecting the sintering temperature due to the relatively low decomposition temperature of typical SEs like $LiNi_{0.5}Mn_{1.5}O_4$ (LNMO) and $Li_7La_3Zr_2O_{12}$ (LLZ) at 600 °C [131,132]. Because of the possible formation of Li_2CO_3 on the surface, the cathode-oxide assembly must be slit under dry or inert environment [131].

In general, the material costs represent 75 % of the manufacturing costs, where cathode production constitute 49.5 % [133]. The manufacturing costs include processing steps such as mixing, coating, and drying and final drying, which are the most cost sensitive process steps. Therefore, dry coating processes would be desirable in order to reduce production costs [133].

The cell assembly of an ASSB cell, e.g. in a format of a pouch cell, can be similar performed like that of LIBs. The components are layered and then conducted with ultrasonic or laser welding [133]. The cell is then placed in an electric insulating housing made of aluminum-polymer foil to protect the cell against environmental influences.

3.1 Production of polymer-based electrolytes

As mentioned earlier, it is becoming increasingly important to make the shift from fundamental research to production of ASSB components. Thus, existing laboratory-scale processing methods must be evaluated for their suitability for mass production while maintaining the material properties. Only when this shift is successfully accomplished ASSBs will have a chance to replace conventional LIBs in future.

In addition to the manufacturability of polymer-based SEs, production costs are an important aspect to be considered in terms of scaling up the process [16]. In general, the production of polymer-based SEs can be divided into solvent-based and solvent-free production methods. Current solvent-based production methods are solution casting [11], spin coating [11], tape-casting [11], screen printing [11], dip coating [11] and current solvent-free production methods are hot-pressing [11,25–27] and extrusion [28–30]. Drawbacks of solvent-based methods are firstly, the multitude of necessary processing steps, i.e. pre-mixing of the solid components, preparing of a homogeneous slurry where the components are fully dissolved and a drying step to eliminate the solvent. And secondly, as mention earlier, residuals of solvents affect the electrochemical performance of the polymer-based SE [24].

Due these drawbacks production methods without the need of any solvents are preferable. As described in SCHNELL et al. [16] melt processing can be used as mixing step. The conductive salt is dissolved directly in the polymer melt without the need of any solvents. For this mixing method the polymer needs to be thermoplastic. The extrusion process can realize this method at larger scale. The continuity of the process gives a perspective to easily scale up the processing of thermoplastic SEs from laboratory scale to industrial series production. The use of an extruder with multiple feeder reduces the production cost of slurry mixing ($7,396,000 per year (7.91 %), [134]) by eliminating the pre-mixing step. The extrusion process is described in more detail in the following chapter.

The solvent-free and thermal processing route of polymer-based SEs with PEO as polymer component has become increasingly important in recent years [30,35,36,135]. Studies up to this point focused on the thermal stability of high-M_w PEO (M_w= 600k – 4M) during processing as SE or polymer-based composite-cathode using a laboratory kneader or extruder and the material stability during storage. High-M_w PEO shows sensitivity towards the process parameters, e.g. high temperature or kneading speed. CROWLEY and co-workers

investigated the thermal stability of high-M_w PEO (M_w= 1M) using hot-melt extrusion for tablets for pharmaceutical application [35,36]. In their works, they stated that the stability of high-M_w PEO depends on both the storage and process parameters, as well on the M_w. Further, they recommend using low-M_w PEO (M_w= 100k) as processing aid to reduce degradation effects of high-M_w PEO. The studies of FROBOESE et al. [30] and APPETECCHI et al. [135] focus on battery applications and investigate PEO as SE and as catholyte in composite cathodes, respectively. In [30], the authors investigate the kneading behavior of PEO600k for different kneading speeds, device temperatures and filling degrees using SiO_2 as a filling additive and LiTFSI as the conductive salt. In [135], the authors describe the fabrication and characterization of LMO composite cathodes depending on different weight ratio.

3.2 Twin-screw extrusion

The extrusion is a widely used process in plastics technology and industry to plasticize polymer compounds, e.g. in powder or granule form, by means of shear and temperature, and to continuously produce defined semi-finished products. Extrusion is used, for example, in the production of films, window profiles and pipe profiles. In addition, the mixing of several components can be influenced by the choice of extruder (single or twin-screw) and its screw design. In general, the structure of an extruder screw (Figure 5) is identical regardless of its mode of operation. In principle, a screw consists of a screw root with a surrounding flight with a defined flight width. The distance between the flights of the screw flight is called the flight pitch. The ratio between the screw diameter and the length of the screw element is referred to as the L/D ratio. The L/D ratio of the screws defines among others the residence time of the material. The higher the L/D ratio, the greater the residence time.

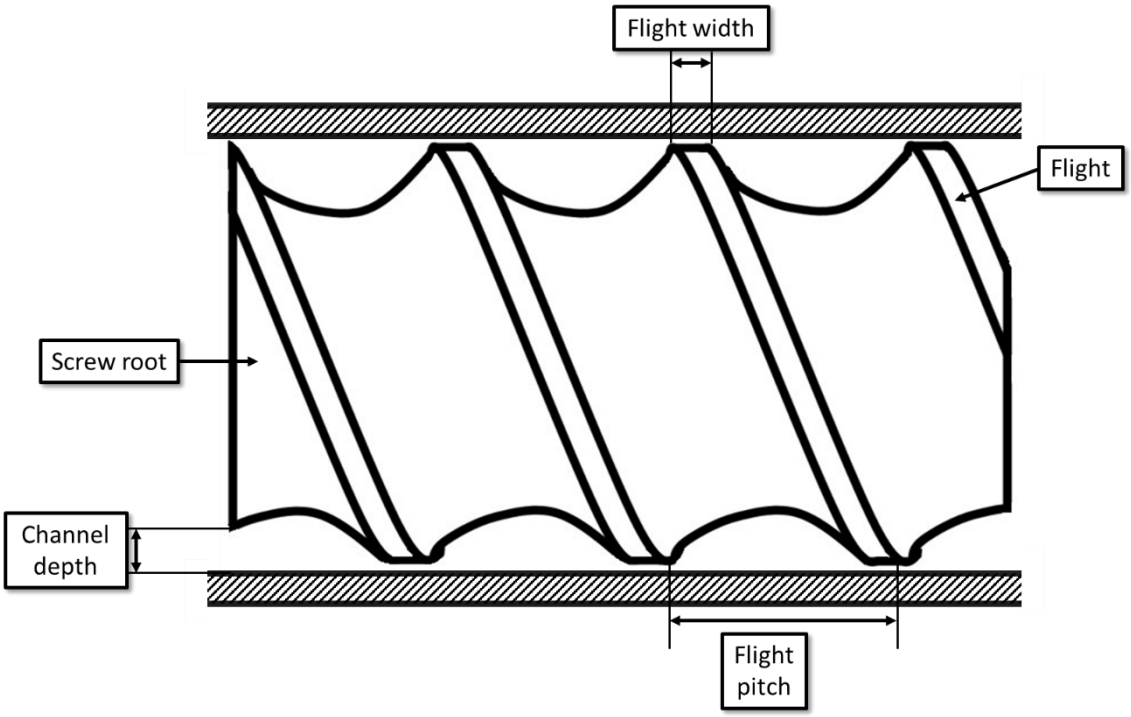

Figure 5: Sketch of a general structure of an extruder screw.

In principle, the homogenization of a mixture is achieved by the energy input in combination with the mixing principle. Parameters such as shear, temperature and time are decisive for the energy input. Mixing is determined by, among other things, recirculation, back flow mixing and shearing. The extruder used in this thesis is a twin-screw extruder, which is therefore described in more detail below. There are several types of twin screw extruders. As Figure 6 shows a distinction is made between counter-rotating, where the screws have different rotation direction, and co-rotating, where the screws have the same rotation direction, as well as between non-intermeshing and intermeshing. Intermeshing screws have no gap between the screw flight and the screw root, while non-intermeshing screws have a gap, and the screws are not in contact.

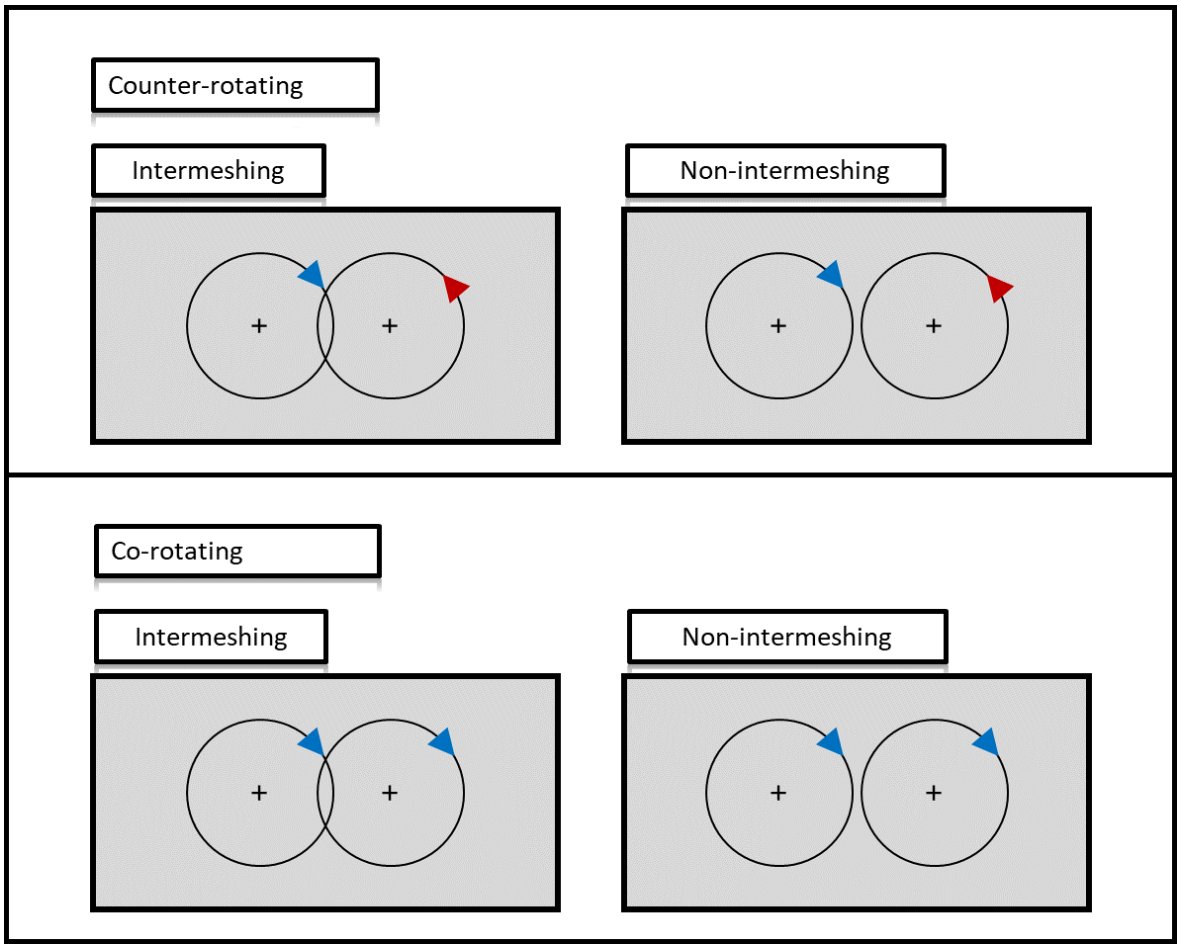

Figure 6: Sketch of twin screw extruder types divided by rotation and screw alignment.

In this thesis, a co-rotating and close intermeshing twin-screw extruder is used. This means that the screw flights of one screw scrape the screw root of the other screw. This area is called the intermesh area. Due to the displacement effect, the mass is transferred from one screw to the other in an 8-figure shape. There is forced support in the gusset area. Outside the gusset area, drag flow predominates, which mainly depends on the friction conditions between the mass and the screw surface, as well as between the mass and the barrel surface. Figure 7 shows the important areas within the barrel for mass transport and their predominating flows.

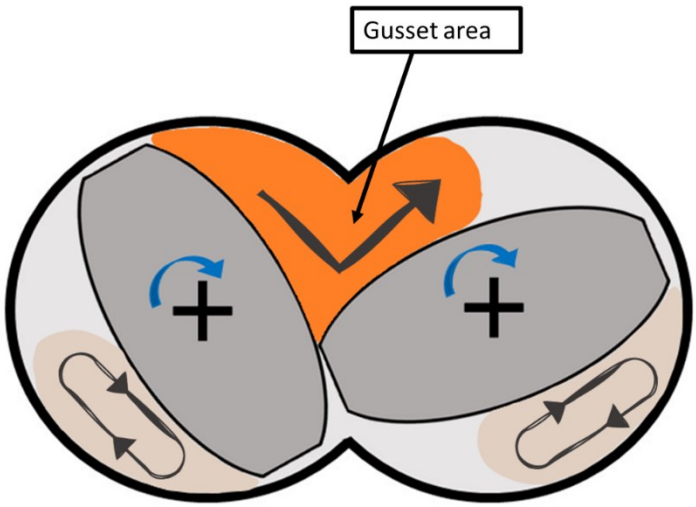

Figure 7: Sketch of material transport within the barrel of a co-rotating intermeshing twin-screw extruder and the predominating flows. Orange area= gusset area, where the flow occurs due to forced support and beige area= outside the gusset area, where drag flow predominates.

If, in addition to conveying elements, the screw configuration contains kneading elements (shearing parts) or mixing parts (web openings), the homogenization of the mixture is greatly affected. In kneading elements, several individual disks are arranged one behind the other at a defined angle to each other. This results in improved mixing in the area of the kneading elements, causing the mass to experience significantly higher shear. Mixing elements, on the other hand, are designed having no shear-intensive areas along the element. Mixing should be accomplished by the backflow of material through the existing grooves. Therefore, best mixing is achieved when the mixing elements are working against pressure, i.e. when they are fully filled.

Due to its continuity and upscaling potential, extrusion has become increasingly important in the battery community in recent years. Among others, extrusion is used for slurry mixing of conventional LIB cathodes [136–138]. In the processing of conventional electrode materials, research is also focused on switching from solvent-based processing to solvent-less and even to dry processing for next generation electrodes [139].This would not only eliminate toxic and hazardous solvents (NMP) [140,141], such as those used in cathode production, and its recovery. It would also eliminate the subsequent drying step after the slurries are applied to the current collectors and the associated meter-long drying ovens. This would mean a significant cost and energy reduction in the production of electrodes (cost per year: coating & drying: 13,984,000 $ (14.96 %); solvent recovery: 4,296,000 $ (4.60 %) – energy consumption per cell: coating 0.18 kWh (1.36 %); drying & solvent recovery: 6.22 kWh

(46.84 %) [134]). There are already initial attempts to dry mix the electrode components using extrusion [142,143].

Extrusion is also a promising candidate for dry processing of ASSB components. As discussed in the previous chapter 3.1, extrusion is particularly used for the dry processing of polymer-based SEs and polymer-based composite cathodes [29,138]. Extrusion has also become established on an industrial scale by the Bolloré company. They use extrusion to produce all the components (Li metal anode, polymer electrolyte and LFP cathode) of their commercially available LMP® battery [41,42]. However, implementation of this process is still in its infancy because little is known scientifically about the interaction between product quality and process parameters. In addition, this relationship is highly dependent on the choice of materials, but also on the choice of process parameters used, making it difficult to define the optimal process and transfer it directly to other systems.

II Experimental

4. Production of polymer-based solid electrolytes

The aim of this thesis is to find suitable process parameters for the dry and thermal production of polymer-based SE while maintaining the properties of the polymeric material. Figure 8 shows the flow chart of the production steps of polymer-based SE used for this thesis. To investigate the thermal behavior of the polymeric material and the influence of the addition of Li-salt on the material stability during the thermal process kneading experiments are examined. The results are then transferred to the melt extrusion process to produce homogeneous polymer-based SEs. For further characterization all samples need to be post-processed by hot-pressing. In the following, each process step is explained in more detail in this chapter.

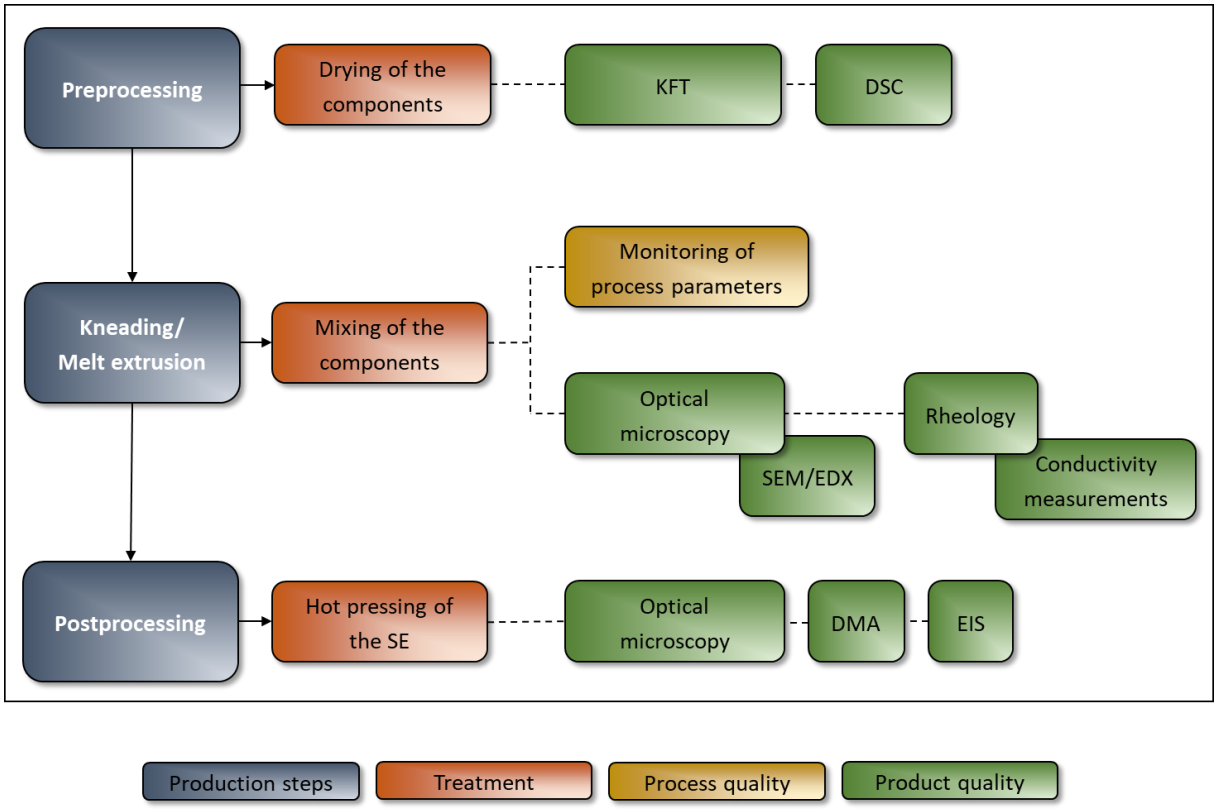

Figure 8: Flow chart of the production steps in the production of polymer-based solid electrolytes used in this thesis.

4.1 Materials

In this thesis PEO, *DuPont/IFF*, is used as thermoplastic polymer matrix and LiTFSI as conductive salt to produce polymer-based SE. For the kneading experiments, LiTFSI was supplied by *Solvionic* and for the extrusion experiments it was supplied by *Carbolution Chemicals GmbH*. To investigate the influence of molecular weight of the polymer on the thermal processability of PEO and to make sure that the ionic conductivity of the produced electrolytes behaves independent of the molecular weight, molecular weight > 2 x 10^3 g mol^{-1} is chosen for this thesis. Therefore, PEO100k (Polyox WSR N10) and PEO600k (Polyox WSR 205) are used for low-M_w and high-M_w PEO, respectively.

Since the coordination of Li-ions occurs through the ether-bridge of the polymer, the molar ratio between the ether-group of the PEO-monomer (EO) and the Li-ion (Li) is used for the mixing ratio of the polymer electrolyte [44]. It is stated as EO:Li and is calculated as follows:

$$\frac{n_{EO}}{n_{Li}} = \frac{m_{EO} * M_{LiTFSI}}{m_{LiTFSI} * M_{EO}} \qquad \text{Eq. (3.1)}$$

The solid electrolytes investigated for this work have a constant molar ratio of 20:1 (EO:Li), since this composition shows relatively high ionic conductivity at elevated temperature [144]. Further, since the stickiness increases with increasing LiTFSI concentration [33,145], the chosen composition simplifies the handling during thermal processing and the extraction of the polymer electrolyte.

4.1.1 Sample preparation

All sample preparations are performed in an Argon filled glovebox (O_2 < 0.1 ppm; H_2O < 0.1 ppm). To ensure the atmosphere within the box and to prevent any influence of water residues on the process behavior of the polymer electrolyte, all components are dried under vacuum for 12 hours before use. LiTFSI was dried at 120 °C and PEO at 50 °C due to its low melting temperature ~65 °C.

As mentioned earlier in this chapter, all samples need to be post-processed by hot-pressing. Therefore, a uniaxial hydraulic press HLP20, *HÖFER Presstechnik GmbH*, placed in a glovebox is used. Figure 9 shows a scheme of sample preparation for the post processing by

hot-pressing. The samples are placed between to Silicon coated PP sheets. To define the thickness of the SE, PP sheet with a thickness of 280 µm is used as spacer. The press matrix is put into an Aluminum bag and fixed with two steel plates. The prepared samples are then pressed at 90 °C with a pressing force of 10 – 12 kN for 5 minutes.

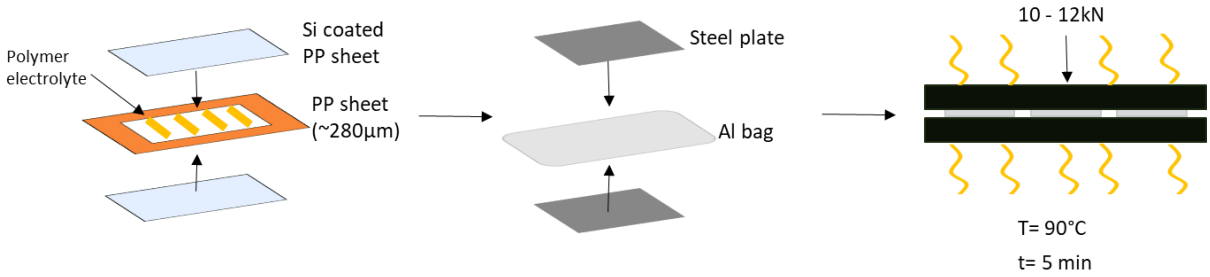

Figure 9: Scheme of sample preparation for hot-pressing with a hydraulic press in a glovebox.

4.2 Kneading experiments

To investigate the thermal processing behavior of PEO and $(PEO)_{20}$LiTFSI-electrolytes, a Plasti-Corder/Lab-Station, *Brabender*, with kneading equipment was used (s. Figure 10).

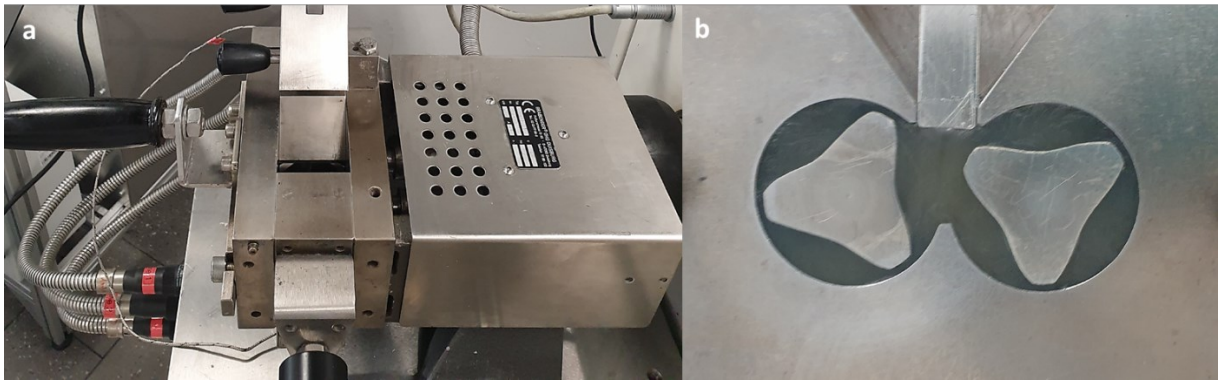

Figure 10: Laboratory kneader (Brabender) in lateral view (a) and polymer filled kneading chamber with roller blades (b).

The laboratory kneader has a sample volume of 50 mL. For the kneading experiments, roller blades were used. Adjustable process parameters are the applied device temperature and kneading speed of the roller blades. For process monitoring and to investigate the influence of the process parameters, torque and mass temperature were constantly measured over the whole kneading time. The kneading experiments were carried out at a device temperature of 90 and 100 °C and with kneading speeds of 5, 10, 15 and 20 min^{-1} for neat PEO and 5 and 20 min^{-1} for $(PEO)_{20}$LiTFSI-electrolytes. For examination of the influence of lithium salt on

the thermal processing behavior, PEO was first melted under process conditions. After 20 minutes of kneading, the polymer has been completely and homogeneous melted. LiTFSI was then added to the polymer melt.

4.3 Extrusion of PEO-based solid electrolytes

To produce PEO based solid electrolytes, a continuous and scalable melt extrusion process was chosen. Figure 11 shows the used co-rotating twin-screw extruder, *ThreeTec*, with two feeders in an Argon filled glovebox (O_2 and H_2O < 1 ppm). The twin-screw extruder consists of five heating zones and an assembled 3 mm string nozzle. The length to diameter (L/D) ratio of a single screw element is 36/24 mm. The total screw length is 576 mm. The screw design can be varied with conveying, kneading and mixing elements. The maximal screw speed that can be applied is 300 rpm. The extruder also has two feeders for material addition. Feeder 1 (s. Figure 11b) consists of a twin-screw and is suitable for feeding poorly flowing powders and granules. The maximum filling volume of feeder 1 is ~ 9 L. Feeder 1 can add the material through the zero position of the barrel in front of the first heating zone. Feeder 2 (s. Figure 11 b) consists of a single screw and is suitable for the feeding of free-flowing powders and granules. The maximum filling volume is ~ 5 L and the material can be added through the filling positions at heating zones 2 and 3.

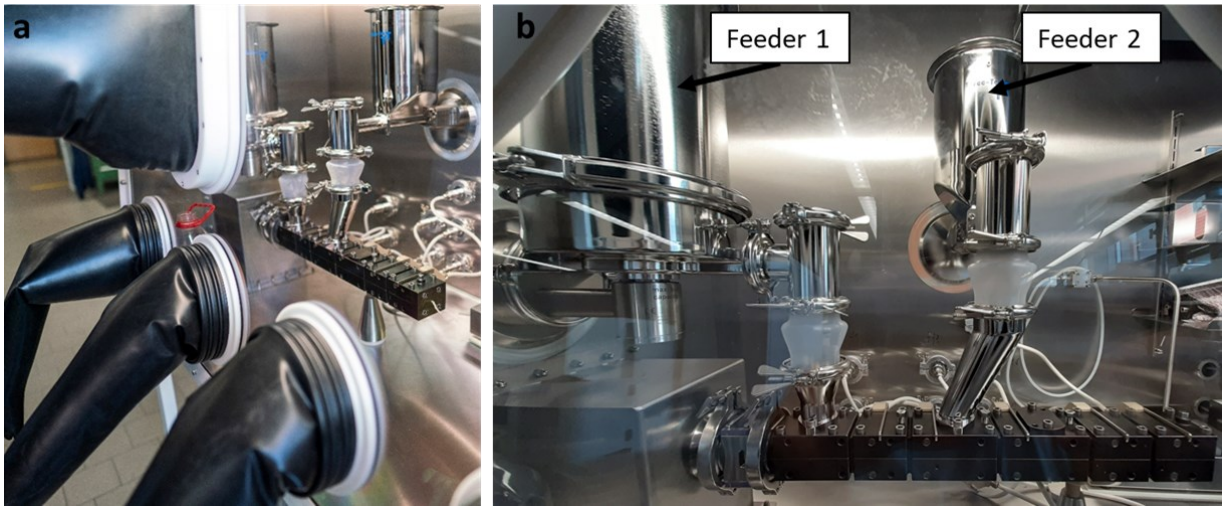

Figure 11: Twin-screw extruder with two feeders in an Argon filled glovebox.

Extrusion experiments are performed with two extruder setups to investigate the effects of various setups on the mixing behavior of PEO and LiTFSI. The first setup (E1) was the extrusion of a pre-mixed batch of PEO and LiTFSI powder that was fed through the first

filling position (s. chapter 4.3.1). For the second extruder setup (E2) the two powders were added separately to the extrusion process by using both feeders (s. chapter 4.3.2). In order to find the optimal screw design for the production of PEO-based SE, three different screw designs for both extruder setups are considered. The screw can be designed with conveying, kneading and mixing elements (s. Figure 12) which are placed between the heating zone 3 and 4. During the extrusion process parameters such as pressure at the extruder die, actual screw speed, torque and barrel temperature are continuously measured.

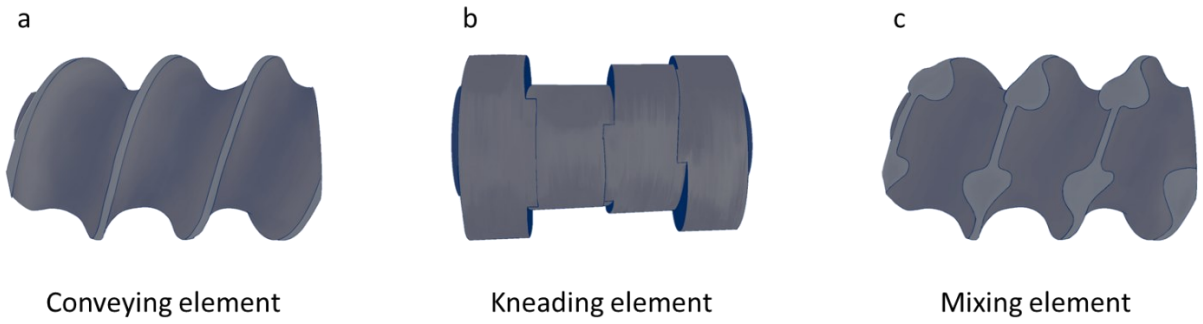

Figure 12: Scheme of the three screw elements used for this thesis - a: conveying element; b: kneading element; c: mixing element.

To determine the material output in kg h^{-1}, the amount of material coming out of the extruder in one minute was weighed. The material output was determined for all screw geometries and screw speeds used in this thesis using a triple measurement. The material outputs as a function of screw geometry and screw speed are listed in Table 1.

Table 1: Material output of extruder dependent on screw design and screw speed.

Screw design	Screw speed [rpm]	Material output [g min^{-1}]	Material output [g h^{-1}]
A	5	8 ± 0	480
	10	16 ± 0	960
	15	27 ± 0	1,620
B	5	4 ± 0	240
	10	11.3 ± 0.5	680
	15	15.3 ± 0.5	920
C	5	4.7 ± 0.5	282
	10	10 ± 0	600
	15	16 ± 0	960

4.3.1 Extrusion of pre-mixed PEO_{20}LiTFSI powder batch

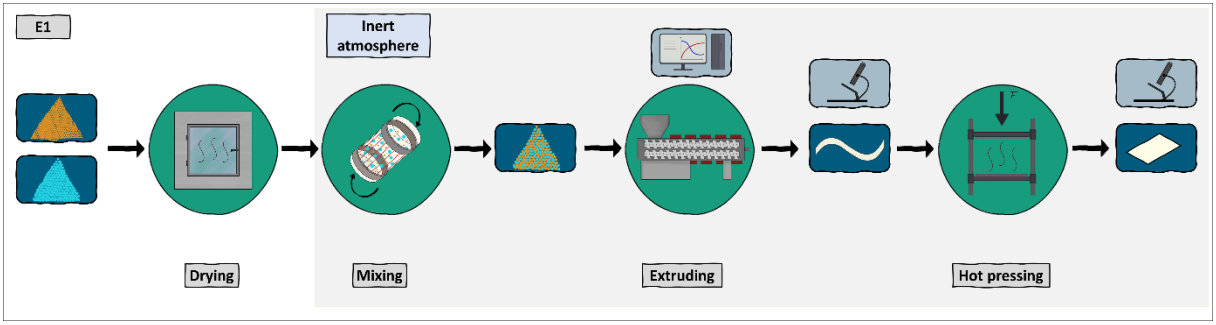

Figure 13. Flow chart of production of PEO_{20}LiTFSI-electrolytes by extruding a pre-mixed powder batch in the first extruder setup (E1).

As in Figure 13 presented, for the first extruder setup (E1) the powder batches are prepared by pre-mixing PEO and LiTFSI in a ratio of 20:1 (EO:Li). The powder is mixed for 30 minutes

with a TURBULA®, *Willy A. Bachofen AG*, to obtain a homogeneous mixture. During mixing, a small amount of heat is generated between the powder particles, making the mixture too sticky for the use of the automated feeders. Hence, the pre-mixed powder was added to the extrusion process through the first feeder (s. Figure 14) by hand. To ensure the reproducibility of the extrusion, care was taken to make sure that the material addition was continuous and that only material was added that the screws could take.

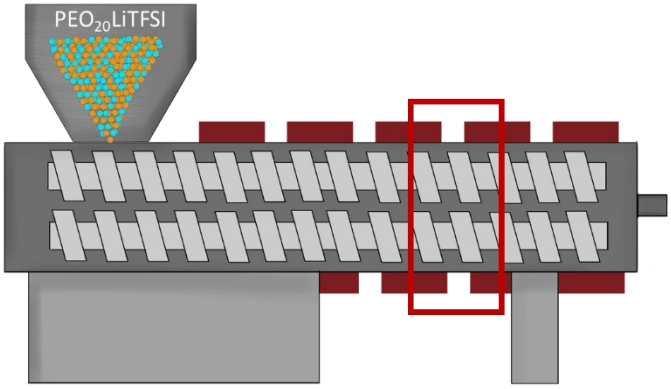

Figure 14: Scheme of extruder setup E1 for the extrusion of pre-mixed PEO_{20}LiTFSI powder batch.

The extrusion experiments are performed for all three screw designs with a constant barrel temperature of 90 °C and screw speeds of 5, 10 and 15 rpm.

4.3.2 Extrusion of PEO_{20}LiTFSI-electrolytes using two feeders

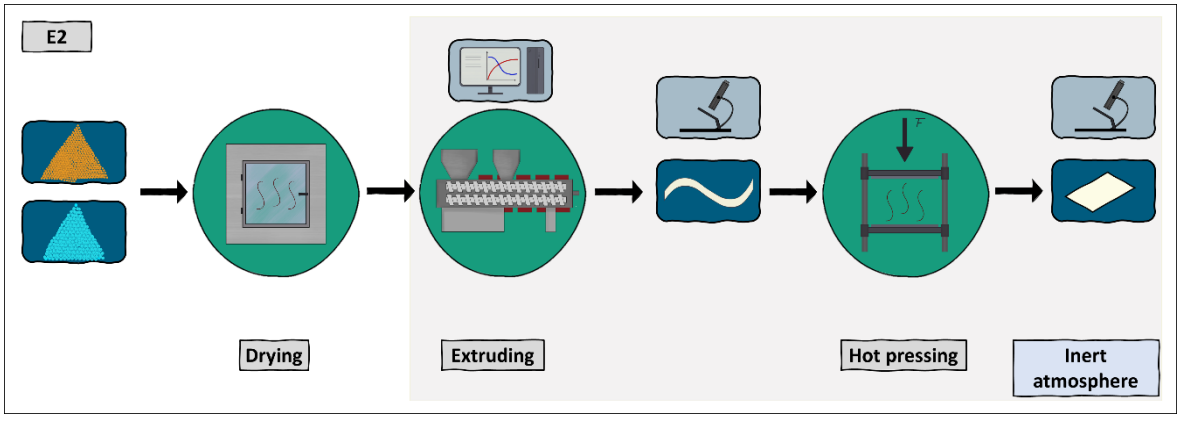

Figure 15: Flow chart of production of PEO_{20}LiTFSI-electrolytes by extruding the components using two feeders in the second extruder setup (E2).

For the second extruder setup (E2) PEO and LiTFSI powder are added separately to the extrusion process. The separate material addition eliminates the pre-mixing step in the experimental setup as shown in Figure 15. PEO and LiTFSI powder were filled directly after drying in the first feeder and second feeder, respectively (s. Figure 16). Similar to the kneading experiments, PEO was first melted before LiTFSI was added to the process.

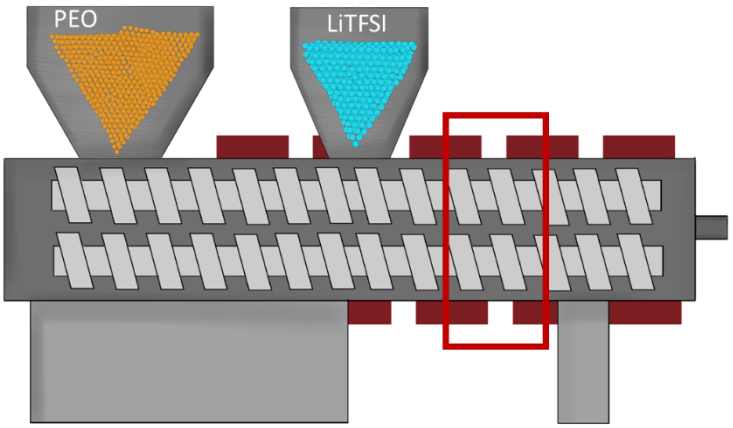

Figure 16: Scheme of extruder setup E2 for the extrusion of PEO_{20}LiTFSI-electrolytes using two feeders.

To automate the process, it is necessary to determine the device characteristic curve for each feeding unit depending on the used material. The device characteristic curve specifies the screw speed of the feeding unit at which a defined material output is added to the process. This makes it possible to add the material fully automated to the process. The device characteristic curves, as illustrated in Figure 17, is determined by measuring the material output at different applied screw speeds.

a b

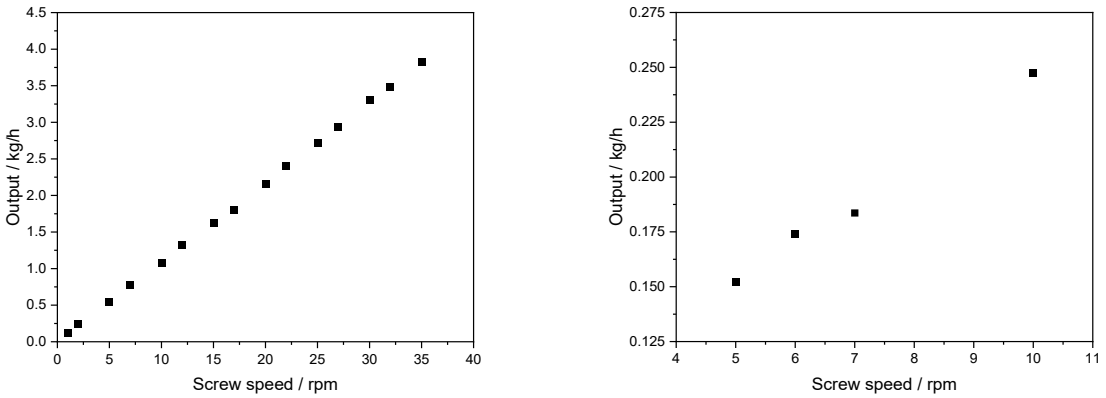

Figure 17: Device characteristic curve for a: 1st feeder for PEO powder and b: 2nd feeder for LiTFSI powder.

For comparison all extrusion experiments are performed at a constant barrel temperature of 90 °C and screw speeds of 5, 10 and 15 rpm.

5. Characterization methods

5.1 Pre-characterization

5.1.1 Differential scanning calorimetry

Differential scanning calorimetry (DSC) is used to measure the heat flow within a sample occurring during thermal treatment. With DSC endothermic (e.g. glass transition and melting) and exothermic (crystallization) effects can be detected. These physical transitions can be then quantitatively determined. For this thesis, a heat flow DSC is used. Here, the sample and the reference are placed in the same furnace and heated simultaneously.

DSC measurements are examined to determine the thermal properties of PEO depending on its molecular weight and the addition of Li-salt. For this work, a DSC Discovery, *TA Instruments*, was used. For sample preparation, PEO powder and a mixture of PEO and LiTFSI powder are filled in Aluminum crucibles. To overcome the thermal history of the polymeric material and to ensure the dissolution of LiTFSI into the polymeric matrix, all samples are heated up to 120 °C at a heating rate of 10 K min^{-1}. Prior cooling, the sample is held at 120 °C for one minute and is then cooled down to -80 °C at a cooling rate of 10 K min^{-1}. The thermal properties, such as glass transition temperature (T_g), melting temperature (T_m) and crystallinity (K), were then determined in a second heating run from -80 – 180 °C with a heating rate of 10 K min^{-1}. The sample was equilibrated at -80 °C for one minute prior to the start of the second heating cycle.

5.1.2 Karl Fischer Titration

Karl Fischer titration (KFT) is a quantitative method for determining the water content in ppm of a substance. The optimal reaction rate of a KFT, in which water is titrated with a buffer solution, is between pH 5.5 and 8.

KFT was carried out to determine the water content of the PEO and LiTFSI before and after drying the materials. For this thesis, a 330S Coulometric KF Titrator, *Mettler Toledo*, was used. Therefore, 0.5 g of each sample is placed in a vial and the exact weight is recorded. A

triple measurement is made for each sample. KFT was examined dry at a temperature of 180 °C.

5.2 Product characterization

5.2.1 Optical microscopy

Optical microscopy is one of the easiest and fastest imaging method to get an idea about the morphological surface structure of the sample. The resolution is limited by the wavelength (λ) of the visible light (λ= 400 – 800 nm). For optical microscopy, two kinds of light source can be used: incident and transmitted light. The use of transmitted light with a polarizing filter makes it possible to see crystals and internal stresses within the polymeric material.

For microscopic observation, a digital microscope VHX7000, *Keyence*, with a polarizing filter was used. For sample preparation, the kneaded $(PEO)_{20}$LiTFSI-electrolytes were hot-pressed to different layer thicknesses. For the characterization of the homogeneity of the kneaded $(PEO)_{20}$LiTFSI-electrolytes, the samples were pressed to a layer thickness of 100 µm. For observation of the crystal growth of the polymeric material samples were hot-pressed to a layer thickness of 10 µm. Observations were performed with incident light and with transmitted light using polarizing filter, respectively. The kneaded neat PEO-samples were microscopically examined without any preparation. Spherulite size is determined by measuring the size of more than 10 spherulites from the central point to its edge.

The extruded samples were characterized macroscopically using incident light. Samples are cut out from the extruded string of each produced PEO-based SE. To avoid any changes in morphology and handle the samples outside the glovebox, the extruded electrolyte-strings were sealed in petri dishes.

5.2.2 Scanning electron microscopy

For supporting of the digital microscopy observations, the surface morphologies of all samples were obtained from scanning electron microscopy (SEM). During the microscopy, the surface is scanned in a raster scan pattern with a focused beam of electrons that interacts

with atoms in the sample. For imaging, emitted secondary electrons by the excited atoms and back scattered electrons from the beam are detected.

For this thesis a Phenom™ proX, *Accurion*, in an Argon filled glovebox was used. The SEM was operating with an electron beam of 10 kV. The kneaded PEO and PEO-based SE samples were sputtered with Pt/Pd before microscopic investigation. To avoid morphological changes within the PEO-based electrolytes, the samples were prepared and transferred under inert conditions.

5.2.3 EDX-Analysis

To determine the Li-salt distribution within the polymer matrix after kneading EDX-analysis was used. In EDX-analysis the atoms in the sample are excited by an electron beam and then emit X-rays of an energy specific to that element. The detected radiation then provides information about the elemental composition of the sample.

For this thesis, a Phenom™ proX, *Accurion*, coupled with SEM in an Argon filled glovebox was used. The EDX-analysis was carried out using an electron beam of 15 kV. For EDX-analysis, the same kneading samples were used as for SEM.

5.2.4 Determination of the molecular weight

5.2.4.1 Gel permeation chromatography

Gel permeation chromatography (GPC) is a technique to determine the molecular weight distribution of polymers. Before testing, the polymer is dissolved in a suitable solution by forming polymeric coils. The dissolved polymer is then introduced to the mobile phase and flows through the GPC column. The higher the molecular weight, the larger the coils formed, and the shorter the retention time due to less interaction with the pores in the GPC column.

GPC was performed to determine the molecular weight of the kneaded PEO and PEO-based SE samples. The measurements were carried out externally. All samples are dissolved in a 0.05 % (aq.) NaN_3 solution. For this thesis, the number average molecular weight M_n and the

polydispersity are examined for evaluation of polymer stability during processing. The polydispersity is a measure for the width of a molecular mass distribution and is calculated as follows:

$$d=\frac{M_w}{M_n} \tag{2.2}$$

5.2.4.2 Rheology measurements

The viscosity (η) of the dissolved polymer is determined by rheology measurements. The viscosity is measured as function of an applied shear rate ($\dot{\gamma}$). For polymer solution, the use of a cone-plate geometry is preferrable due the constant velocity transfer over the whole geometry. In this thesis, a correlation (s. Figure 18) is made between the determined viscosities of the kneaded samples and the determined M_w by GPC measurement. Thereby, it is possible to calculate M_w by the viscosity of the extruded PEO-based electrolyte.

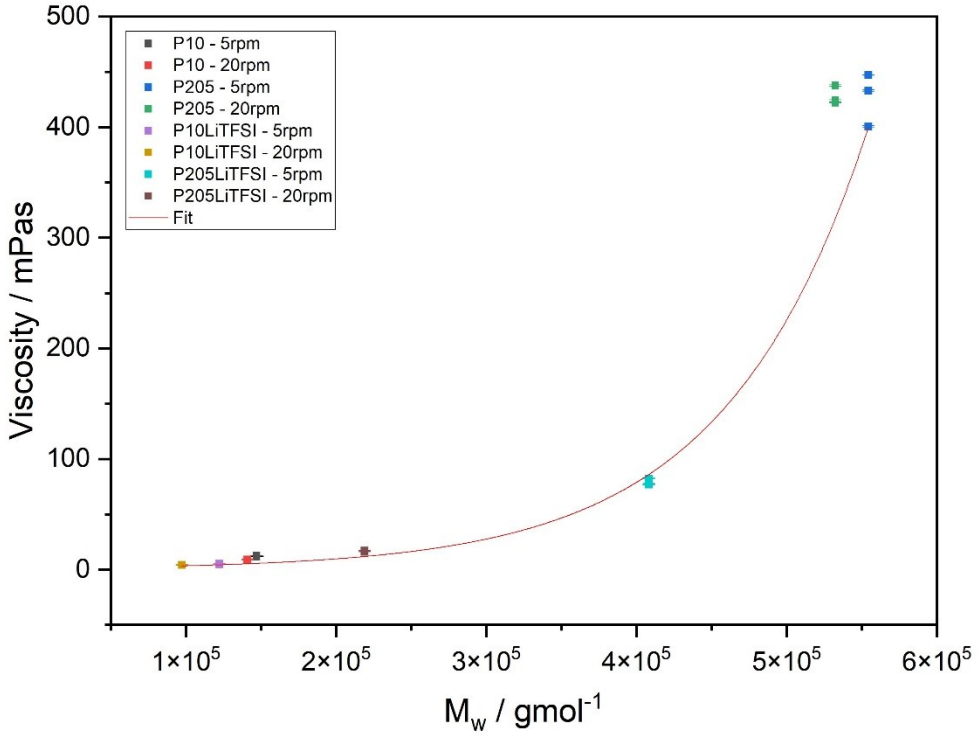

Figure 18: Viscosity (η) vs. molecular weight (Mw) for the determination of Mw by rheology measurements.

Rheology measurements are performed with rotational rheometers MCR702, *AntonPaar*, and DHR 2, *TA Instruments*, using a cone-plate geometry (50 mm/1 ° and 40 mm/1 °,

respectively). The measurements are carried out at 25 °C with a constant $\dot{\gamma}$ of 50 1 s^{-1}. The viscosity is then measured for 10 minutes. The viscosity of the kneaded samples, the extruded PEO-based electrolytes, the pristine PEO powder and the PEO_{20}LiTFSI powder is determined. The samples are dissolved in water at 5 wt %.

5.2.5 Dynamic mechanical analysis

The dynamic mechanical analysis (DMA) is a measurement method used to determine the time and temperature dependent properties of polymeric materials. The material is excited by a sinusoidal force and the corresponding response signal is time delayed due to the viscoelastic material behavior. The results obtained are the temperature-dependent storage modulus G' and loss modulus G'', where G' and G'' represent the elastic and the viscous portions of |G*|, respectively.

To determine the thermo-mechanical properties of the produced polymer electrolytes, temperature-dependent DMA is used. The PEO-based SEs were hot-pressed at 90 °C to a thickness of 1 mm and were then punched to a diameter of 25 mm. DMA measurements were performed using an oscillating rheometer MCR702, *Anton Paar*, using a 25 mm parallel plate geometry at 1 Hz and a deformation amplitude of 0.1 % in a temperature range of 20 – 100 °C with a heating ramp of 1 K min^{-1}.

5.2.6 Electrochemical impedance spectroscopy

Impedance spectroscopy is the study of a response of a system to a periodic sinusoidal excitation. For the electrochemical impedance spectroscopy (EIS) the samples are excited by a sinusoidal voltage of varying frequency and small amplitude. By the detection of the resulting current and phase shift, the complex resistance can be determined. The given impedance spectra can be fitted with an equivalent circuit.

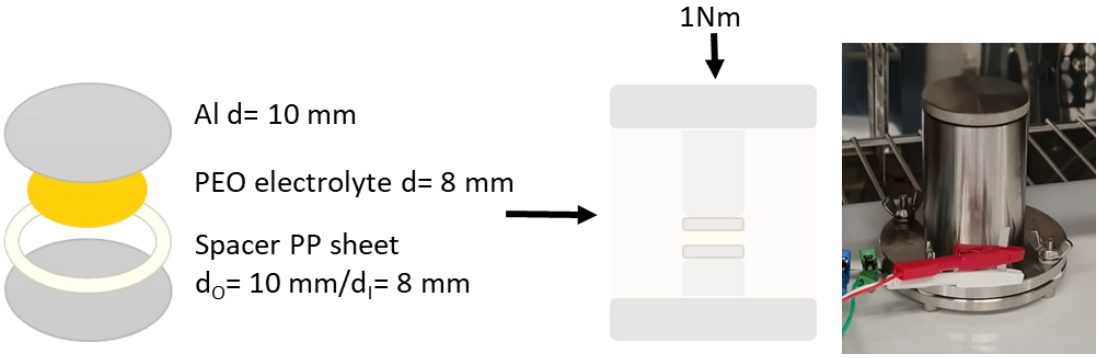

Figure 19: Assembly of PEO-based SE in a symmetric cell for electrochemical characterization with a Hohsen cell.

EIS was used to determine the Li-ion conductivity of the extruded PEO-based SEs using an Interface 1010E, *GAMRY*. For measuring, symmetric cells are tested in Hohsen cells (Figure 19). Samples are cut out from the hot-pressed PEO-based SE sheets with an 8 mm round punch and contacted with Aluminum blocking electrodes. To avoid that the electrolyte flowing away, an electronic insulating spacer (PP foil) with an inner diameter of 8 mm and an outer diameter of 10 mm is put around the electrolyte. A pressure of 1 N m was applied to the sample. The frequencies were varied between 10^6 Hz to 1 Hz with an amplitude of 10 mV. The measurements are carried out at a temperature range of 80 to 20 °C. The impedance measurement started after a delay of 55 minutes to ensure that the sample had reached the measurement temperature.

III Results and Discussion

6. Pre-characterization

This chapter deals with the pre-characterization of the used educts PEO100k, PEO600k and LiTFSI. DSC measurements are performed to determine the thermal properties of PEO and their relationship to its molecular weight and the addition of LiTFSI. The results of the DSC measurement have been published in: K. Platen, F. Langer, R. Bayer, R. Hollmann, J. Schwenzel, M. Busse: Influence of molecular weight and Lithium bis(trifluoro-2 methanesulfonyl)imide on the thermal processability of Poly(ethylene oxide) for solid-state electrolytes, Polymers, 2023, *15*(16), 3375. Further, KFT measurements are performed to choose the right drying conditions of the educts before investigations.

6.1 Thermal properties of Poly (ethylene oxide)

DSC measurements are examined to investigate the thermal properties of PEO. Further, the determined melting temperature T_m of PEO depending on its molecular weight and the addition of Li-salt is used to define the process window for thermal processing of PEO. In general, the process temperature is 30 K above the melting temperature of the polymer. Thus, the temperature is high enough to provide a good flowability of the polymer but is low enough to avoid thermal degradation and chain scissoring [146,147].

Figure 20 shows DSC curves of the 2nd heating run for PEO and PEO-based SEs. The extracted thermal properties are listed in Table 2. Thermal properties of PEO show dependencies on the molecular weight as well as of the addition of LiTFSI. The thermal property most affected by the molecular weight is the melting temperature (T_m) of the crystalline portion of the polymer. T_m is determined from the maximum of the endothermic peak. With higher molecular weight, T_m shifts to higher temperatures. PEO600k has its T_m at 65 °C, which is 4 °C higher than the T_m of PEO100k (T_m= 61 °C). The effect of the molecular weight on the thermal properties are in a good agreement with earlier works [36,148–150]. CROWLEY and co-workers investigated PEO with different molecular weights (M_w= 100.000 and M_w= 1.000.000) and found out that with decreasing molecular weight, PEO has a higher proportion of smaller crystals [36]. Therefore, smaller crystals require less energy for melting than bigger crystals in PEO with higher molecular weight. In general, it can be estimated for semi-crystalline polymers that crystal growth rate decreases with increasing molecular weight [149]. Furthermore, VRANDEČIĆ et al. describes the crystalline

phase of PEO comparing different molecular weights (M_w= 100.000 – 5.000.000). The higher the molecular weight of PEO, the lower the segmental mobility and convenient geometrical alignment within the polymer chain [150]. All those points underline the shift of T_m to higher temperature with higher M_w. For thermal processing this minor shift in T_m by 4 °C does not affect the process window of PEO. Thus, same process temperatures can be selected for both molecular weights.

The degree of crystallinity is calculated from the ratio of the experimentally determined melting enthalpy to that of a 100 % crystalline PEO as follows:

$$K = \frac{\Delta H_{m(exp.)}}{\Delta H_{(100\%\ cryst.PEO)}} \tag{6.1}$$

with $\Delta H_{(100\ \%\ cryst\ PEO)}$= 203 J g^{-1} [114]. The crystallinity of neat PEO is not influenced by the molecular weight (Table 2).

Compared to the molecular weight, the addition of LiTFSI shows minor effect on T_m. Since the thermal properties of polymer electrolytes are already investigated in other works, i.e. by MARZANTOWICZ and co-workers, EDMAN et al. and LASCAUD et al., the effect of LiTFSI and other Li-salts on the thermal properties of PEO is well understood [31,38,114,151–153]. The authors put focus on the influence of LiTFSI on the recrystallization behavior of PEO finding that with higher amount of Li-salt the recrystallization kinetics decrease. These observations were made in the 2nd heating run of a quenched sample observing a shift or even a disappearance of T_m. However, the determined T_m of salt containing PEO are in a good agreement with the results of this work [150,152]. In addition, LiTFSI obviously reduces the peak height that is directly affecting the crystallinity of the polymer electrolyte. Furthermore, for PEO-based SEs with the TFSI-anion as a crystal inhibitor, the nucleation is the limiting step for crystallization [31]. The crystallinity decreases for both molecular weights from 70 % to 28 % (Table 2).

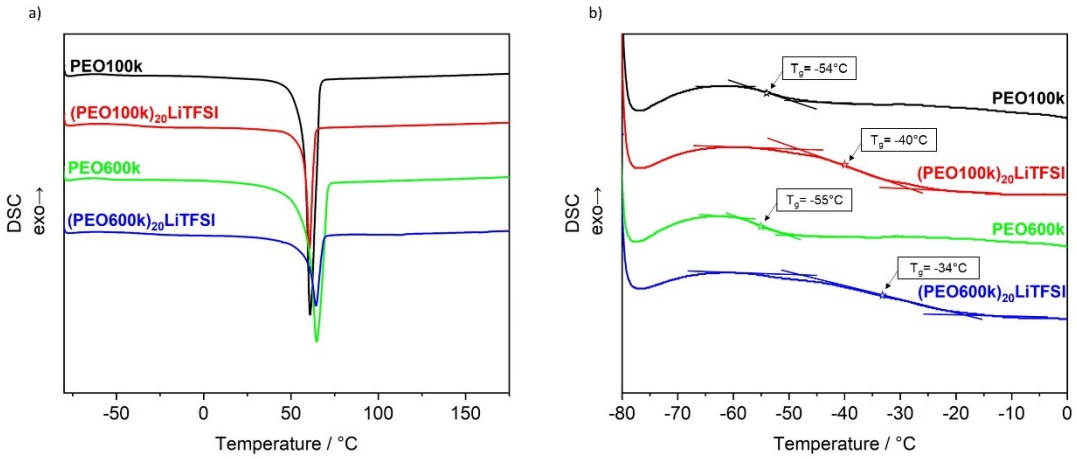

Figure 20: Complete DSC curves of neat PEO and PEO-based SEs with different molecular weights (a) and zoom to lower temperature (b); determination of the glass transition temperature (Tg), melting temperature (Tm) and crystallinity (K) from the 2nd heating run to avoid any effects of the thermal history.

As the crystallinity (K) does not change as a function of M_w, the glass transition temperature (T_g) also remains unchanged with different M_w. T_g is determined as midpoint of the endothermic step in Figure 20b). This is in a good agreement with the observation VRANDEČIĆ and co-workers made in their work [150]. T_g and K are not affected by the molecular weight. In contrast to the molecular weight, addition of LiTFSI affects primarily the amorphous region of the polymer. The addition of LiTFSI leads to a lower chain mobility of the polymeric matrix, which shifted T_g to higher temperatures ($T_{g((PEO100k)20LiTFSI)}$= -40 °C, $T_{g((PEO600k)20LiTFSI)}$= -34 °C). The Li-cation coordinates oxygen-atoms from different PEO-chains resulting in a three-dimensional physical network.

Table 2: Thermal properties of neat PEO and PEO_{20}LiTFSI-electrolytes.

Material	**Glass transition temperature Tg [°C]**	**Melting temperature Tm [°C]**	**Enthalpy of melting ΔH_m [J g^{-1}]**	**Crystallinity K [%]**
PEO100k	-54	61	142	70
$(PEO100k)_{20}$LiTFSI	-40	61	57	28
PEO600k	-55	65	142	70
$(PEO600k)_{20}$LiTFSI	-34	64	56	28

All in all, for thermal processing the minor shift in T_m by 4 °C does not affect the process window of PEO. Thus, same process temperatures can be selected for both molecular weights.

6.2 Karl Fischer Titration

In this thesis, Karl Fischer Titration is examined to determine the water content of the used materials. This is necessary to evaluate the right drying condition for each material, especially for PEO due to its low T_m. So that the materials have as less as possible water residues.

Table 3: Water content in ppm of used materials before and after drying determined by Karl Fischer Titration.

Material	**Sample preparation**	**Water content [ppm]**
PEO100k	as received	1837 ± 45
	dried at 40 °C over night	394 ± 6
	dried at 50 °C over night	358 ± 5
	storage 1 day under ambient atmosphere	1917 ± 29
LiTFSI	as received	41 ± 1

Table 3 shows the determined water content in ppm of the used PEO100k and LiTFSI before and after drying. It gets obvious that a complete drying of PEO is not possible with the chosen drying parameters. PEO has still a water content of > 350 ppm after drying it at 50 °C over night under full vacuum. However, these parameters are used for drying PEO because of the low T_m= 61°C determined by DSC (Table 2) for PEO100k. The KFT results also show the hygroscopic behavior of PEO characterize by an increase of water content of 81 % after one day under ambient atmosphere. Due to the high ppm values of PEO, LiTFSI can be used as received with a water content of 41 ± 1 ppm.

KFT-measurements show that it is not possible to eliminate the water residues in PEO due to the low drying temperature of 50 °C. In addition, due to its hygroscopic behavior, exposure of PEO to ambient atmosphere should be kept to a minimum.

7. Kneading experiments

This chapter deals with the characterization of the thermal processing behavior of PEO-based electrolytes. The focus is on the effect of the molecular weight and LiTFSI on the processing behavior of PEO. The results of these experiments are then taken to set the right process parameter and to choose the right molecular weight of PEO for the extrusion experiments. Parts of this chapter have been published in: K. Platen, F. Langer, R. Bayer, R. Hollmann, J. Schwenzel, M. Busse: Influence of molecular weight and Lithium bis(trifluoro-2 methanesulfonyl)imide on the thermal processability of 3 Poly(ethylene oxide) for solid-state electrolytes, Polymers, 2023, *15*(16), 3375.

7.1 Process characterization

7.1.1 Influence of the molecular weight of Poly (ethylene oxide)

As emerged from the DSC results (chapter 6.1), PEO100k and PEO600k can be processed with same process conditions. To ensure that the polymer is completely melted and has a good flowability during the process, process temperatures should be 30 K +T_m. In this work, the kneading experiments were carried out at process temperature of 90 and 100 °C.

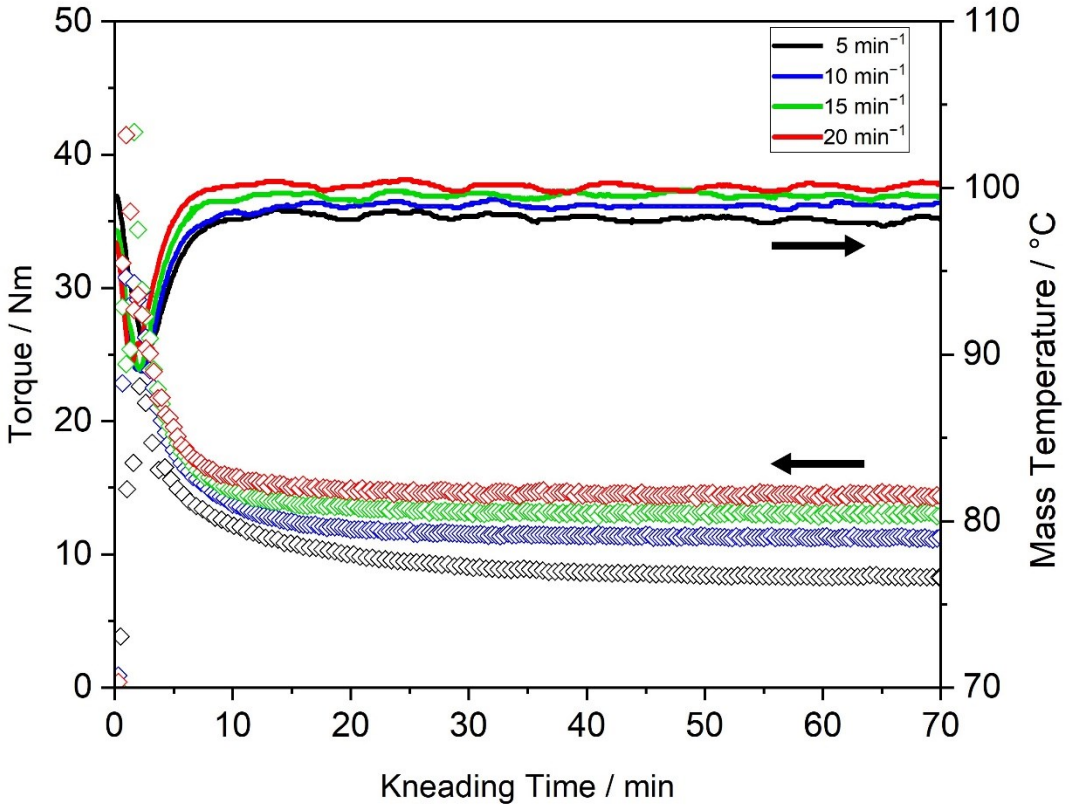

Figure 21: Kneading curves of neat PEO100k at a process temperature of 100 °C and with different kneading speeds (5-20 min^{-1}).

First, the kneading behavior of neat PEO is determined depending on the process parameters and its molecular weight. Figure 21 shows the kneading curve of PEO100k. The applied kneading temperature is 100 °C and the kneading speed varies from 5 to 20 min^{-1}. In the first 20 minutes, melting of the polymer can be observed characterized by the decrease in torque. The completion of melting is determined by the offset of the peak maximum in torque (Figure 22). The higher the applied kneading speed, the faster the polymer is completely melted. For example, at a kneading temperature of 100 °C and a kneading speed of 20 min^{-1}, the melt is completed in 4 minutes, 13 minutes faster than at a kneading speed of 5 min^{-1}. As shown in Figure 22, at the same kneading speed, the kneading temperature has little effect on the total melting time.

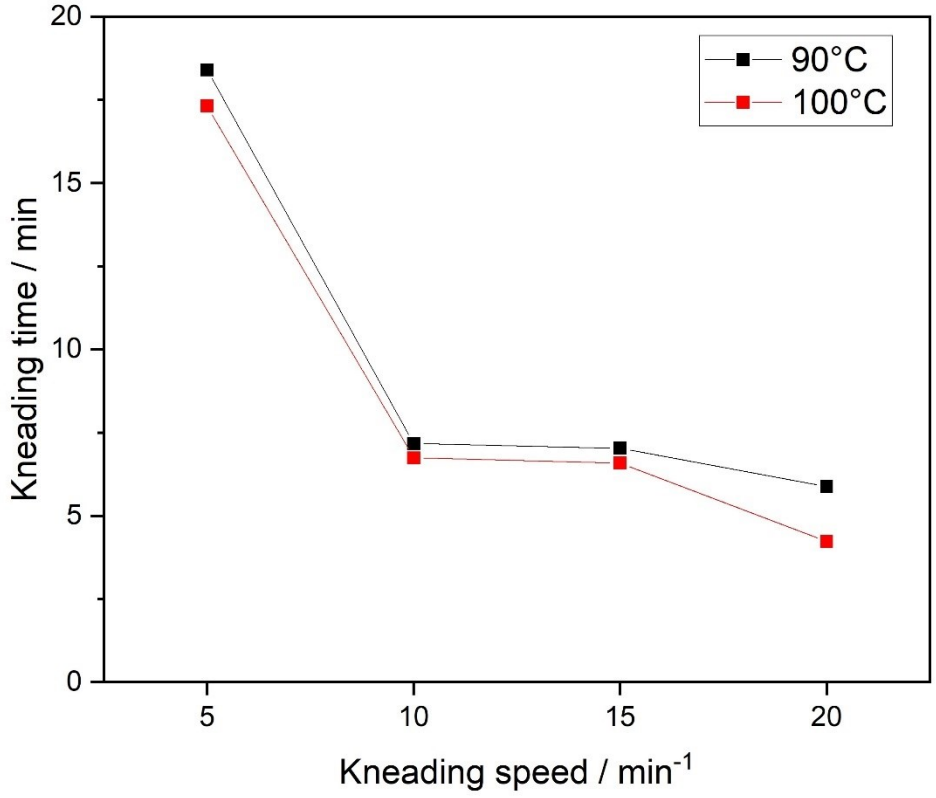

Figure 22: Completion of PEO100k melting dependent on the applied screw speed and the applied kneading temperature determined by the offset of the peak maximum in torque.

The kneading behavior of PEO is influenced by the applied process parameters. The higher the kneading speed, the higher the measured torque and mass temperature. The measured torque of the kneading experiment with 20 min^{-1} is with 14.5 ± 0.2 N m around 39 % higher than for the kneading experiment with 5 min^{-1} (8.8 ± 0.4 N m). Higher kneading speeds resulting in higher torque values are the result of entanglements of the polymeric chains during kneading. While the polymer chains have more time to reorder at a kneading speed of 5 min^{-1}, the shear effect at a kneading speed of 20 min^{-1} gives the polymer chains less time for relaxation. The presence of different levels of shear effects within the material is characterized by the difference in mass temperature. Increased shearing effects provoke a self-heating of the material that leads to higher mass temperature. The same dependencies of kneading speed on the kneading behavior can be observed at a kneading temperature of 90 °C. For the extrusion of PEO, a process temperature of 90 °C is preferred due to less heat impact on the polymer.

The determination of the completion of melting can be taken as the minimum residence time for PEO in the extruder barrel.

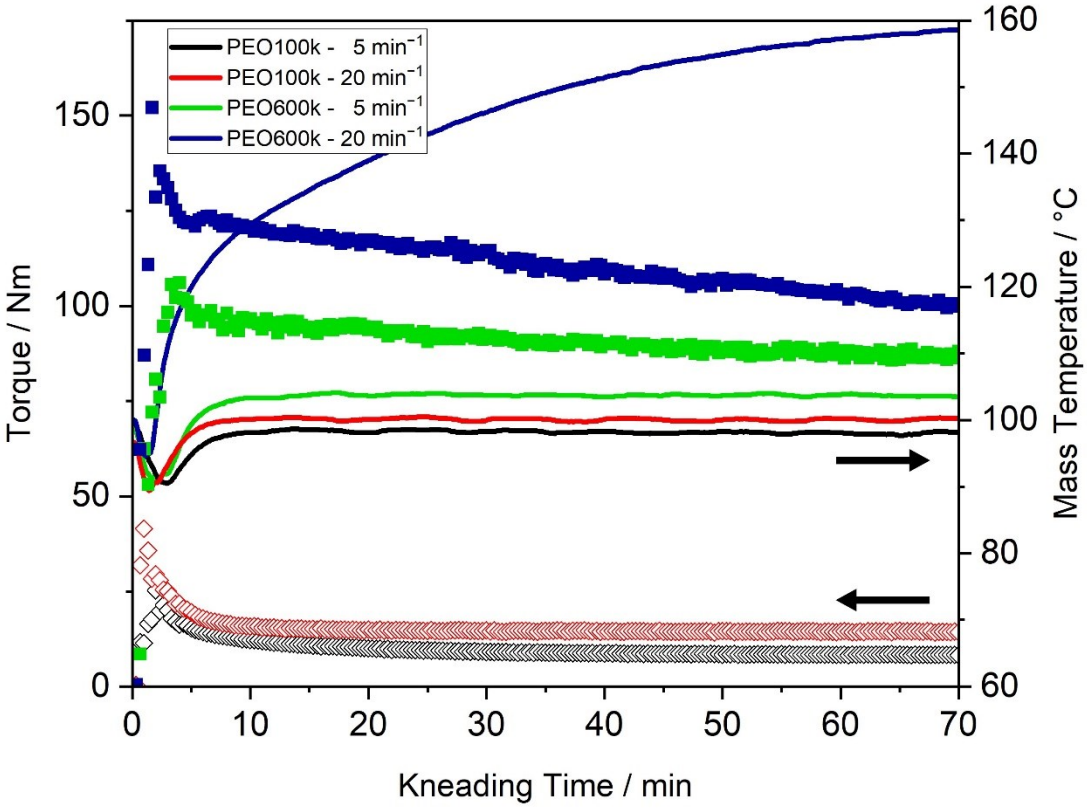

Figure 23: Comparison of kneading curve of PEO with different molecular weight (100k and 600k) at a process temperature of 100 °C and with kneading speeds of 5 and 20 min^{-1}.

Figure 23 shows the dependency of the molecular weight in the kneading behavior of PEO by comparing the kneading behavior of PEO100k with PEO600k at a kneading temperature of 100 °C and kneading speeds of 5 and 20 min^{-1}. A strong influence of molecular weight on the resulting torque is obvious. Using PEO600k clearly results in higher torque values compared to PEO100k over the entire experiment time (t= 50 min, 5 min^{-1}: PEO100k= 8 N m, PEO600k= 89 N m; 20 min^{-1}:PEO100k= 15 N m, PEO600k= 107 N m) Furthermore, even after 20 minutes, when a stable melt is obtained for PEO100k, PEO600k performs less stable characterized by the negative slope in the torque (5 min^{-1}: -0,15; 20 min^{-1}: -0,34). The mass temperature of PEO600k, especially at high kneading speed, rises to 160 °C. With higher kneading speed (20 min^{-1}), the shearing effect within the material due to longer chain lengths leads to self-heating of the polymer and by that to a higher mass temperature over time. The steady decrease in torque and the self-heating effect indicate degradation of PEO600k for a processing temperature of 100 °C. PEO is a very sensitive material to thermal, oxidative and mechanical degradation. The primary mechanism of a degradation process is chain scissoring forming lower molecular weight chains [36]. As there is no decomposition reaction observed

during the DSC measurements (s. Figure 20), the degradation of PEO600k during the kneading experiments depends not only on the device temperature. Hence, the main driving force for the degradation of PEO600k is a combination of the heat development from the device temperature, the self-heating effect of the long chains of PEO600k and the mechanical force induced by the screw speed.

The kneading behavior of PEO600k for different kneading speed, device temperature and filling degree is well described elsewhere [30]. The authors show the importance of selecting an appropriate process window to maintain the properties of PEO. However, the authors observed a reduction in the molecular weight of PEO600k for each parametric setup used, demonstrating the sensitivity of this material to the chosen process parameters.

Although kneading conditions here have been chosen considering the material sensitivity, degradation of PEO600k appears, as described earlier. Furthermore, the self-heating effect and degradation of PEO600k occurs even at 90 °C. The results of the kneading experiments show that PEO100k behaves more stable for the applied process temperatures and kneading speeds, and it is therefore more suitable for thermal processing.

7.1.2 Influence of LiTFSI on the thermal processing of PEO

For the thermal processing route of polymer-based solid electrolytes, it is important to know how the Li-salt affects the thermal properties and the processing window of the polymeric material. Figure 24 shows exemplarily the kneading curves of (PEO100k)-based and (PEO600k)-based electrolytes for a kneading speed of 20 min^{-1} and process temperatures of 90 and 100 °C. The kneading speed of 20 min^{-1} is chosen for representation, because it depicts the harshest process conditions within this work. LiTFSI is added to the process after 20 minutes of kneading PEO, since the previous experiments (s. Figure 22) confirmed that PEO is completely melted then. Furthermore, the addition of LiTFSI to the polymer melt also represents the conditions of extrusion using two feeders. For the filling of LiTFSI the kneading chamber is opened. The filling of LiTFSI is marked as starting point of the mixing of polymer with LiTFSI. For both molecular weights, we can see an effect due to the addition of LiTFSI.

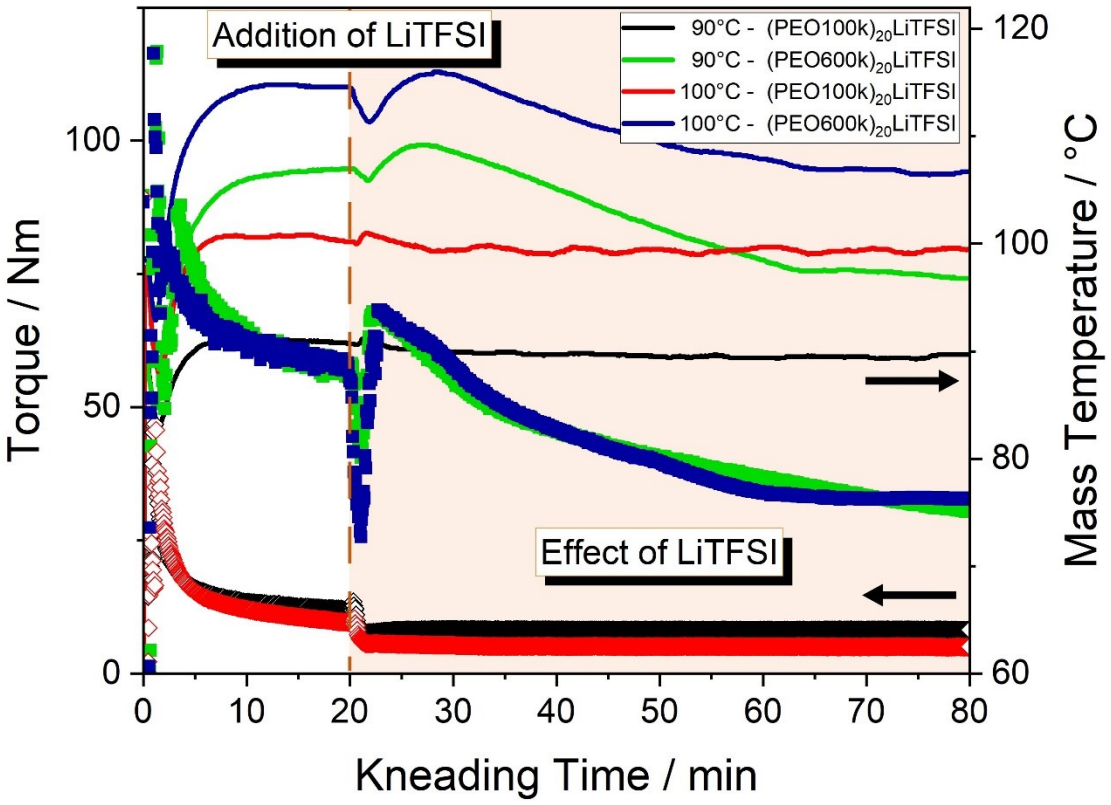

Figure 24: Effect of LiTFSI on the thermal kneading behavior of PEO with different molecular weights at a process temperature of 90 and 100 °C and with kneading speed of 20 min^{-1}.

The kneading curves of PEO100k show a step like drop in torque after the addition of LiTFSI to the process for both temperatures. The kneading curve for 100 °C shows a loss in torque of 5.5 N m. After the drop in torque, it remains constant over the remaining kneading time. There is no further effect of LiTFSI on the recorded torque of PEO100k after the addition to the polymer melt. The loss in torque shows that LiTFSI acts as a plasticizer being mixed and dissolved in the polymeric matrix. The addition of LiTFSI has a negligible impact on the mass temperature. Further the TFSI-anion is also embedded between the polymer chains. This leads to a higher chain mobility and higher flowability of the polymer during thermal processing.

Compared to the kneading curve for PEO100k at 100 °C, the kneading curve of PEO600k at 100 °C doesn't show the step like drop in torque. Instead, a minimum in the torque can be observed due the opening of the kneading chamber. The impact of opening the kneading chamber is higher for PEO600k than for PEO100k. After the filling of LiTFSI and closing the kneading chamber, the torque increases slightly compared to the values prior to opening the chamber due to the cooling effect of LiTFSI and increased volume within the chamber.

However, then the torque continuously decreases by almost 50 % within 55 minutes. In contrast to the PEO100k sample, where LiTFSI acts as a plasticizer, LiTFSI accelerates the degradation process of PEO600k. The characteristic negative slope of the torque curves increases by 51 % for the curve at 90 °C and by 40 % for the curve at 100 °C.
The mass temperature curve of (PEO600k)-based electrolytes shows a reduction in mass temperature due to the addition of the colder LiTFSI powder. In contrast to the self-heating and shearing effect as shown in Figure 23, the mass temperature of (PEO600k)-based electrolytes decreases over the kneading time. Both the decrease in mass temperature and the drop of torque indicates that the plasticizing effect of LiTFSI is overlapped by the degradation process of PEO600k. Degradation overrides the plasticizing effect, as it is assumed that the decrease of mass temperature almost to device temperature is due to smaller chains, which lead to less shearing of the polymer chains.

In summary, the kneading experiments show that PEO100k processing parameters are stable after the addition of LiTFSI. Hence, it is more suitable for the usage as electrolyte material than PEO600k. Since there is no effect of temperature and kneading speed on the polymer stability, both investigated temperature and kneading speed are suitable for the thermal process. However, low temperatures and kneading speeds are preferable for maintaining process stresses in form of shearing effects and elevated mass temperatures as low as possible.

7.2 Product characterization

7.2.1 Digital microscopy observation

Figure 25 shows microscopic images of the kneaded PEO100k and PEO600k samples that are kneaded at 100 °C and with kneading speeds of 5 and 20 min^{-1} as described earlier in this work. PEO100k samples show a smooth surface and no change of color for both kneading speeds. The shiny surface reflects the incident light and images are poor in contrast and no individual particles or shapes can be distinguished. During the extraction of the PEO100k samples after kneading, the polymer melt appears waxy and sticky. Therefore, it is assumed that the polymeric structure remains unchanged regardless of the process parameters. Compared to this, PEO600k displays a broken surface structure, especially for samples kneaded at 20 min^{-1}. In contrast to PEO100k, PEO600k appears dry and crumbly during extraction. The images depict a multitude of fracture surfaces with irregular edges. These microscopic images also indicate the described degradation process of the polymer due to self-heating and shearing effects. Here, the degradation is characterized by a change in color. The discoloration intensifies with higher kneading speed for PEO600k.

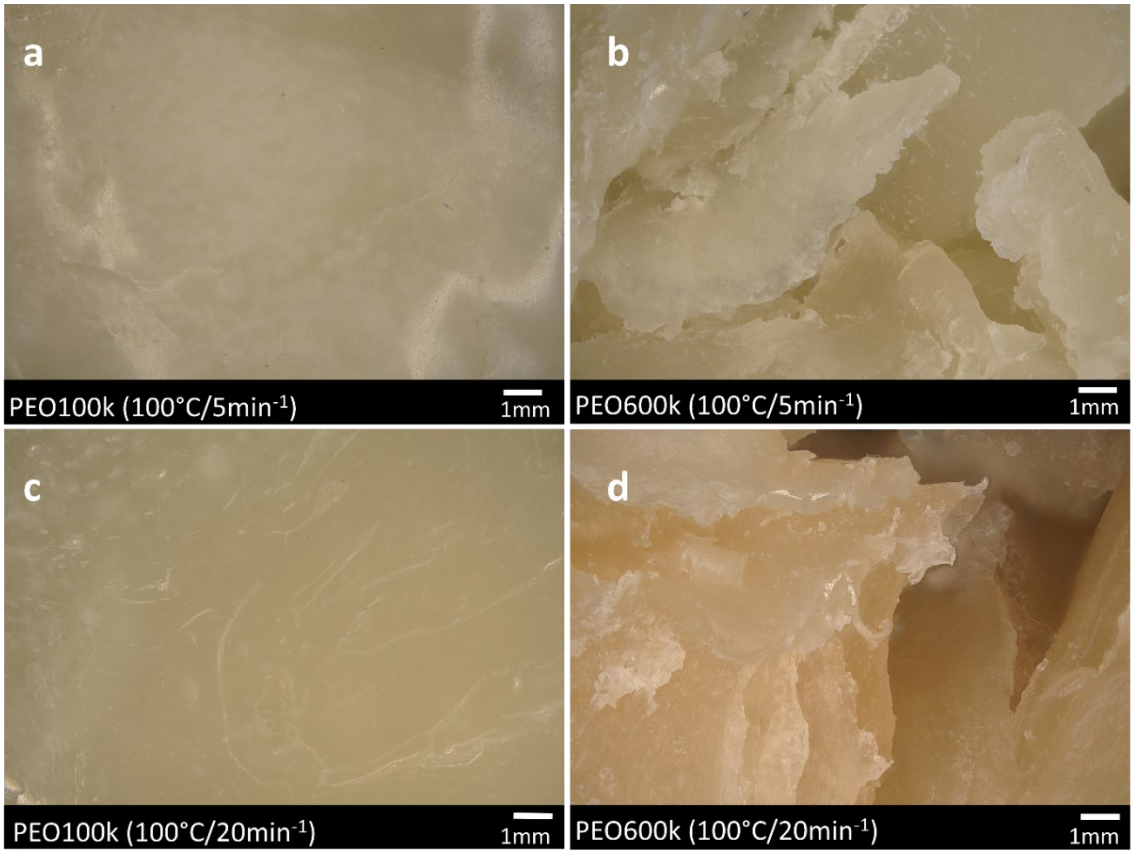

Figure 25: Microscopic images of kneaded PEO100k (a and c) and PEO600k (b and d).

Further microscopic observations are performed to investigate the homogeneity of the kneaded PEO-based electrolytes, as well as to determine the effect of LiTFSI on the crystal growth within the polymer matrix due to its importance and influence on the ionic conductivity. Figure 26 shows microscopic images of (PEO100k)-based electrolytes and (PEO600k)-based electrolytes kneaded at a process temperature of 100 °C and kneading speeds of 5 and 20 min^{-1}. For the investigation for the homogeneity and crystal growth, the kneaded sample were hot-pressed to a layer thickness of 100 and 10 µm, respectively. The images a – d, using incident light, show LiTFSI distribution in the polymer matrix depending on the molecular weight of PEO and the applied kneading speed. For both molecular weights LiTFSI is completely dissolved in the PEO matrix since no residuals of LiTFSI particles are detected. However, differences in the surface of the samples are notable. For example, the kneaded $(PEO600k)_{20}LiTFSI$ sample (Fig. 25b) appears more irregular in its surface compared to the kneaded $(PEO100k)_{20}LiTFSI$ (Fig. 25a). Overall, the morphology of the pressed samples of $(PEO100k)_{20}LiTFSI$ electrolytes appear more homogeneous than $(PEO600k)_{20}LiTFSI$. Figs. 25e – h depict the influence of molecular weight on the crystal growth. Spherulite size is determined by measuring the size from the central point of the spherulite to its edge. $(PEO100k)_{20}LiTFSI$ show spherulites with a size < 10 µm (5 rpm: 8 ± 1 µm; 20 rpm: 6 ± 1 µm) independent of the kneading speed. Instead, $(PEO600k)_{20}LiTFSI$ show larger spherulites (5 rpm: 30 ± 9 µm; 20 rpm: 30 ± 8 µm) for both kneading speeds. Crystal growth appears unaffected by the applied kneading speed, comparing the spherulite size dependent on the kneading speed for both electrolytes. In addition, DSC results from chapter 6.1 show that T_m slightly increases with molecular weight and by that higher temperature is needed to melt the polymer crystals. From correlating spherulite size and melt temperature to the molecular weight, the molecular weight plays a key role for crystal growth. These findings are in accordance with previous studies [36,149].

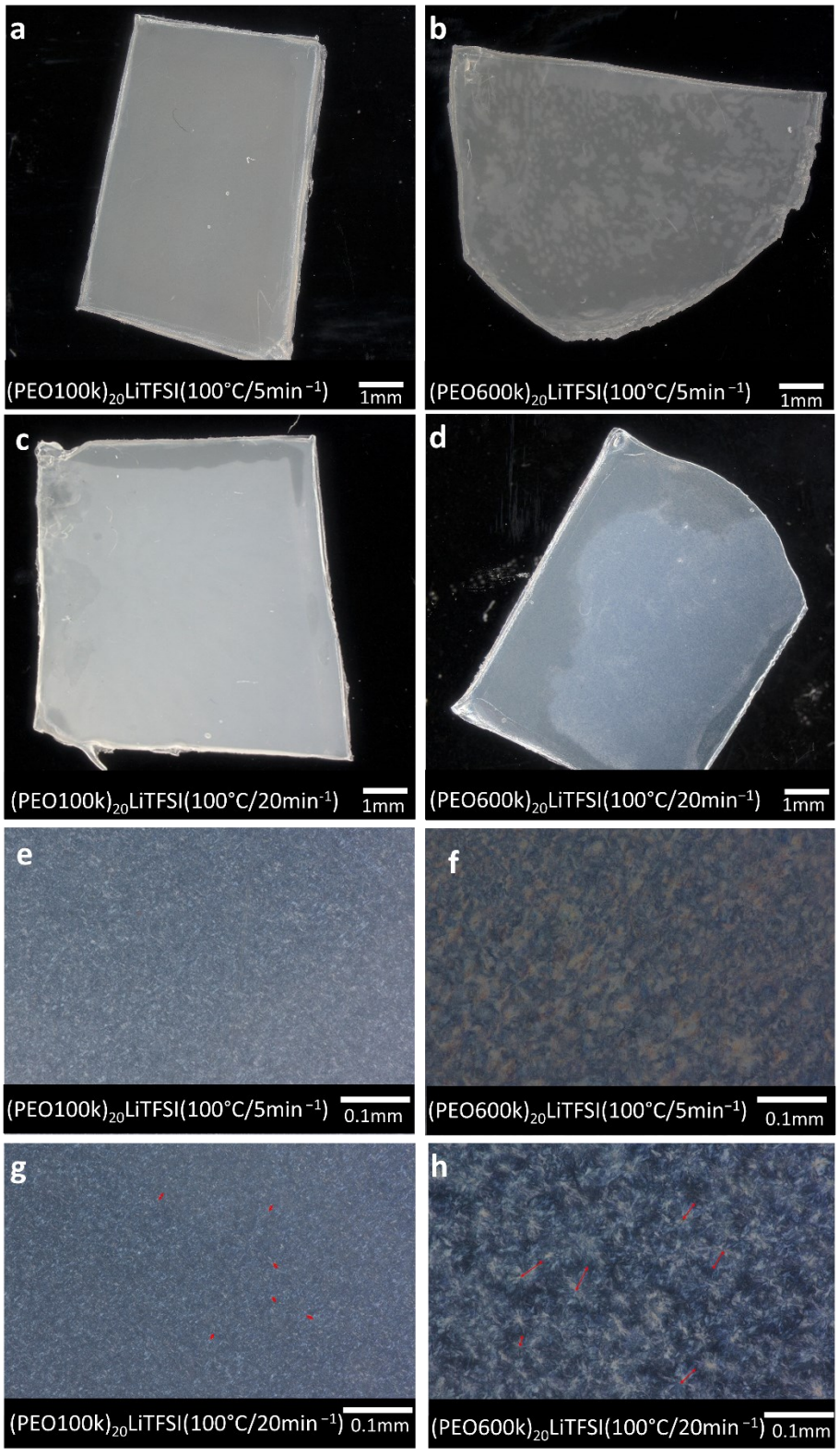

Figure 26: Microscopic images of kneaded polymer-electrolytes: a, b, e and f: $(PEO100k)_{20}LiTFSI$ and $(PEO600k)_{20}LiTFSI$ kneaded at 100 °C with a kneading speed of 5 min^{-1}, hot-pressed for microscopic investigation to a layer thickness of 100 µm and 10 µm, respectively; c, d, g and h: $(PEO100k)_{20}LiTFSI$ and $(PEO600k)_{20}LiTFSI$ kneaded at 100 °C with a kneading speed of 20 min^{-1}, hot-pressed for microscopic investigation to a layer thickness of 100 µm and 10 µm, respectively.

7.2.2 Scanning electron microscopy and EDX analysis

Figure 27 shows SEM images of PEO100k and PEO600k samples that are kneaded at 100 °C and with kneading speeds of 5 and 20 min^{-1}. The PEO100k sample kneaded with 5 min^{-1} (Fig. 26a) shows a smooth surface as already described earlier. The sample kneaded with 20 min^{-1} (Fig. 26b) shows a slight change in surface roughness. Both kneaded PEO600k samples (Fig. 26c+d) show a broken surface structure that becomes stronger with increasing kneading speed. Compared to PEO100k, these samples are more damaged after kneading, supporting the assumption of degradation of the polymer that was made for the digital microscopy images.

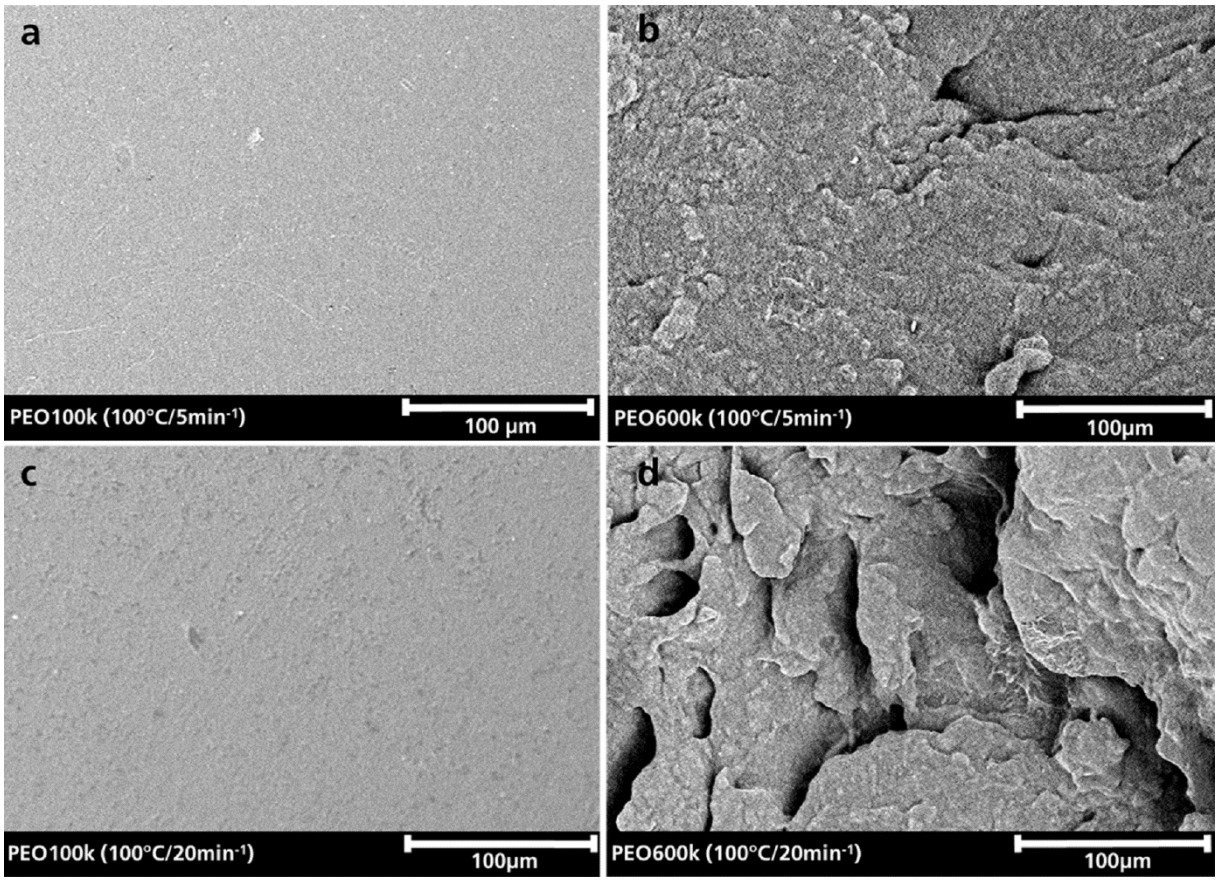

Figure 27: SEM images of kneaded PEO100k (a and c) and PEO600k (b and d).

Figure 28 depicts EDX mapping of the kneaded $(PEO100k)_{20}LiTFSI$ (a and b) and $(PEO600k)_{20}LiTFSI$ (c and d) at 100 °C and with kneading speed of 5 and 20 min^{-1}. The mapping shows for all kneaded electrolytes that LiTFSI is well distributed within the polymeric matrix characterized by the detection of Fluorine (F) and Sulfur (S). Nevertheless, the distribution shows dependency of the applied kneading speed and the molecular weight. With increasing kneading speed, the distribution becomes less homogeneous. Same dependence can be observed with increasing molecular weight. (PEO100k)-based electrolyte shows the best and homogeneous LiTFSI distribution for kneading speed of 5 min^{-1}.

Although EDX can be used to map the fluorine and sulfur atoms and thus to determine the mixing quality of the kneaded samples and the distribution of the LiTFSI in the polymer. The 15 kV electron beam used is too high. The penetration depth of the beam is so deep that it destroys the surface of the samples to be investigated. As a result, elemental analysis cannot be performed accurately, and SEM and EDX are not used for extrusion experiments.

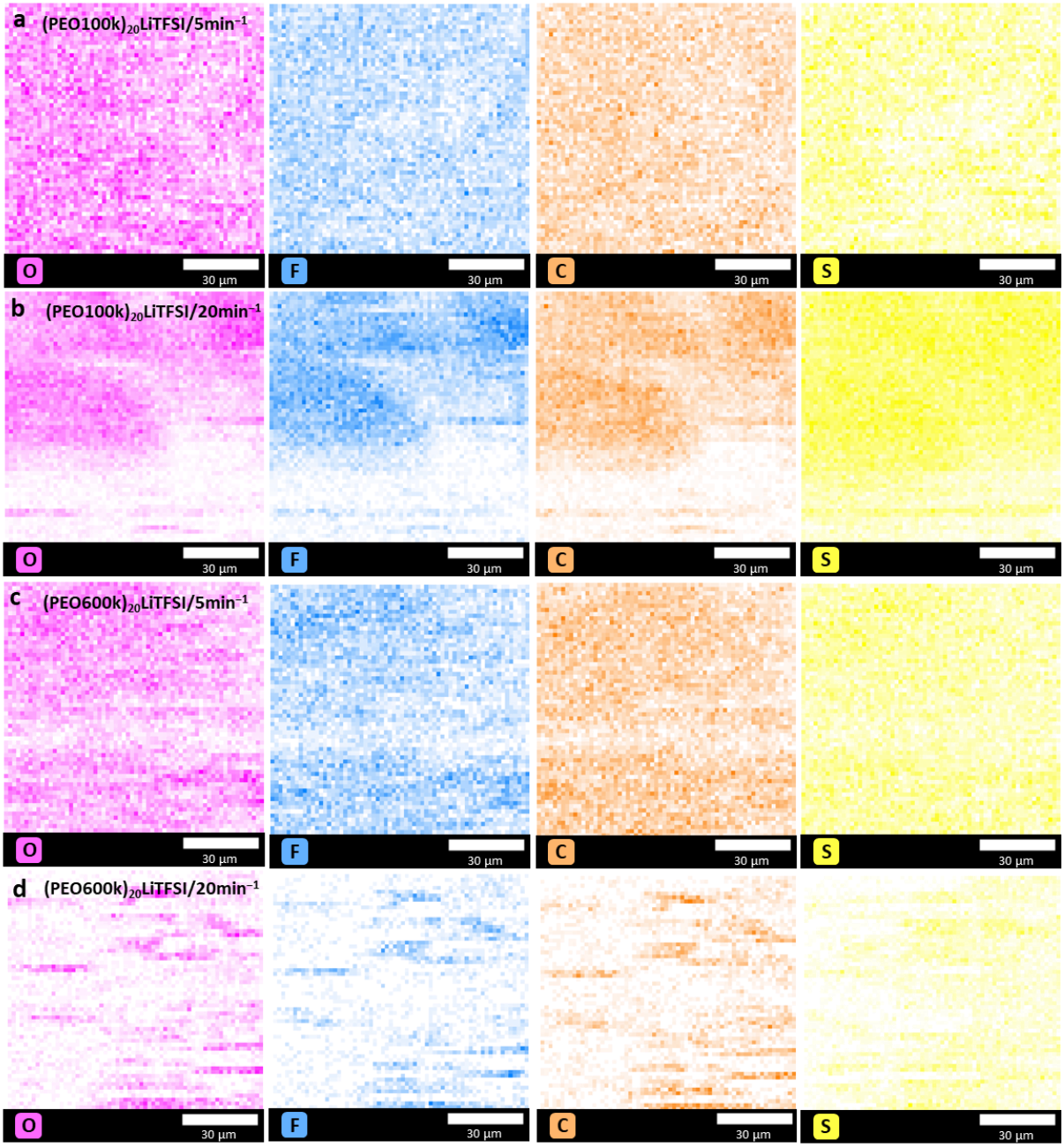

Figure 28: EDX mapping of kneaded $(PEO100k)_{20}LiTFSI$ (a and b) and $(PEO600k)_{20}LiTFSI$ (c and d) at 100 °C.

7.2.3 Gel permeations chromatography

Table 4: GPC results of kneaded neat PEO and PEO-based electrolytes.

	PEO100k				**PEO600k**			
	5 min^{-1}		20 min^{-1}		5 min^{-1}		20 min^{-1}	
	M_n [g mol^{-1}]	d	M_n [g mol^{-1}]	d	M_n [g mol^{-1}]	d	M_n [g mol^{-1}]	d
kneaded	26,300	5.61	26,500	5.32	159,800	3.47	168,700	3.16
+LiTFSI	21,600	5.67	21,500	4.52	159,800	2.58	90,800	2.42

Table 4 shows the number average molecular weight M_n and the polydispersity d for kneaded PEO and $(PEO)_{20}$LiTFSI at 100 °C with kneading speeds of 5 and 20 min^{-1}. M_n of kneaded PEO100k show no significant dependency on the applied kneading speed. The decrease in the polydispersity from 5.61 for low kneading speed to 5.32 for high kneading speed implies a decrease in the molecular weight of the sample kneaded at 20 min^{-1}. This is not detected in the kneading curve as a loss in torque (Figure 21). As the GPC measurement is a direct measure of the retention time in the GPC column, which is directly influenced by the molecular weight of the polymer, it is more sensitive to results. The torque of the kneader, on the other hand, is only a measure of the energy required to maintain the kneading speed, which is influenced by the resistance of the material. Therefore, it provides only indirect information about degradation processes.

Comparing the results of M_n of neat PEO100k with M_n of $(PEO100k)_{20}$LiTFSI, it is noticeable that the addition of LiTFSI shifts M_n to lower values. This implies that all chain lengths are affected by chain scissoring during the process. The correlation between the applied screw speed and d is not further affected by LiTFSI. Regarding the significant decrease in M_n for $(PEO600k)_{20}$LiTFSI from 168,700 to 90,800 at a kneading speed of 20 min^{-1}, it is obvious that the addition of LiTFSI amplifies the degradation of long polymer chains. This amplification of degradation can be a result of the strong Lewis base properties of the TFSI-anion. NIE and co-workers reported the gas generation mechanism of PEO in a full cell at 4.2 V [59]. They highlighted that the TFSI-anion attacks the polymer main chain under the formation of an extremely strong HTFSI acid, which can further attack PEO resulting in chain scission.

7.3 Conclusion

In this chapter, the influence of process parameters, molecular weight, and the addition of conductive salt on the thermal processing behavior of PEO is investigated. The results clearly indicate that care must be taken in the thermal processing of PEO. The following conclusions can be drawn from the kneading experiments:

- A combination of thermal and mechanical load affects the thermal stability and the kneading behavior of PEO during thermal processing.
- PEO100k is more stable during the kneading time and shows the most homogenous LiTFSI distribution at low kneading speed.
- PEO600k is more sensitive to thermal and mechanical load. Degradation occurs due to self-heating and shear effects.
- GPC results show that for both PEO samples, degradation occurs simultaneously with softening of the polymer due to the addition of LiTFSI.
- LiTFSI acts as a plasticizer to improve the flowability of PEO and it intensifies the degradation of long chains of PEO.

Overall, PEO600k is significantly more sensitive and unstable to the addition of LiTFSI during thermal processing than PEO100k. Therefore, PEO100k is preferred for the thermal production of PEO-based solid electrolytes.

8. Extrusion of pre-mixed PEO_{20}LiTFSI powder batch

This chapter presents the results of the first extruder setup, where PEO and LiTFSI powders are first mixed in a molar ratio of 20:1 (EO:Li) using a TURBULA® mixer and are then added to the extrusion process. The extrusion experiments are performed for all three screw designs with a constant barrel temperature of 90 °C and screw speeds of 5, 10 and 15 rpm. Parts in this chapter have been published in: K. Platen, F. Langer, J. Schwenzel: Influence of Screw Design and Process Parameters on the Product Quality of PEO:LiTFSI Solid Electrolytes Using Solvent-Free Melt Extrusion, Batteries 2024, 10(*6*), 183.

8.1 Process characterization

The process parameters are continuously monitored after the extruder is started and the barrel is filled. After reaching a steady state material output, the torque and pressure values are extracted from the last 10 minutes of extrusion as described in chapter 4.3.

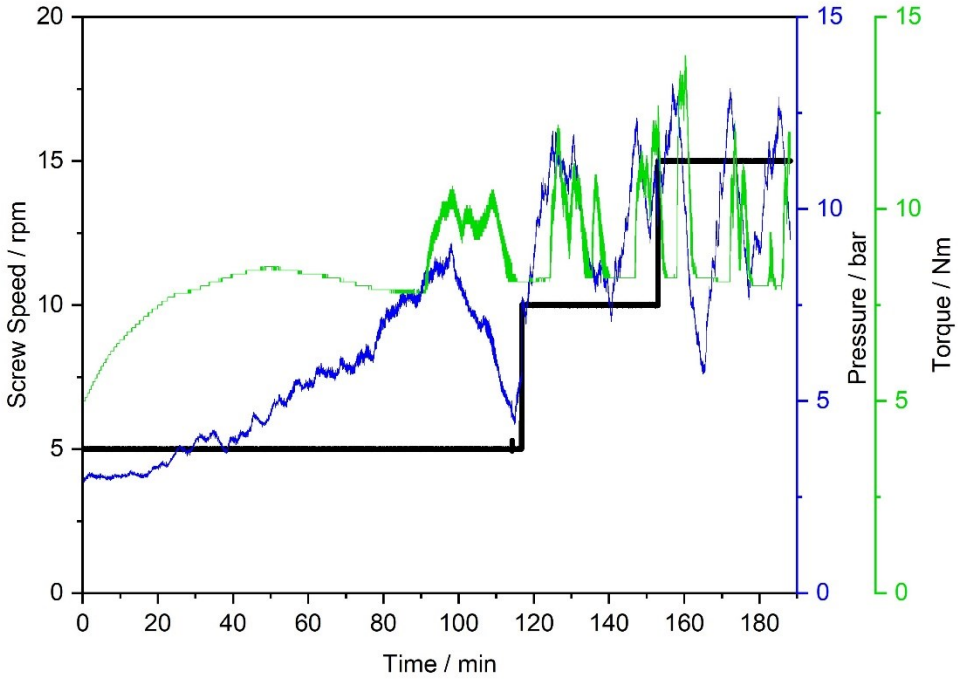

Figure 29: Measured process parameters torque and pressure during the extrusion time, exemplary for the extrusion with screw design A.

Figure 29 shows exemplary the monitored process parameters during the extrusion with screw design A. Process stability can be interpreted as a measure of the error bars.

The left diagram in Figure 30 shows the measured torque for the three screw designs (A, B and C) as a function of the applied screw speeds. It is clearly visible that the torque increases with the applied screw speed for all three screw designs. The smallest error bars and, thus, the most stable process, can be observed for all three screw designs at a low screw speed of 5 rpm. Here, screw design A shows the largest (± 0.82 N m) and screw design C shows the smallest (± 0.09 N m) error bar. At low screw speeds, the residence time of the material in the extruder barrel is longer than at higher screw speeds. The longer the residence time of PEO in the extruder barrel, the more time the PEO has to melt and to dissolve LiTFSI. This applies to all screw design. Due to the plasticizing effect of LiTFSI [154] and by enhancing the flowability of PEO, less energy is required to transfer the material through the barrel.

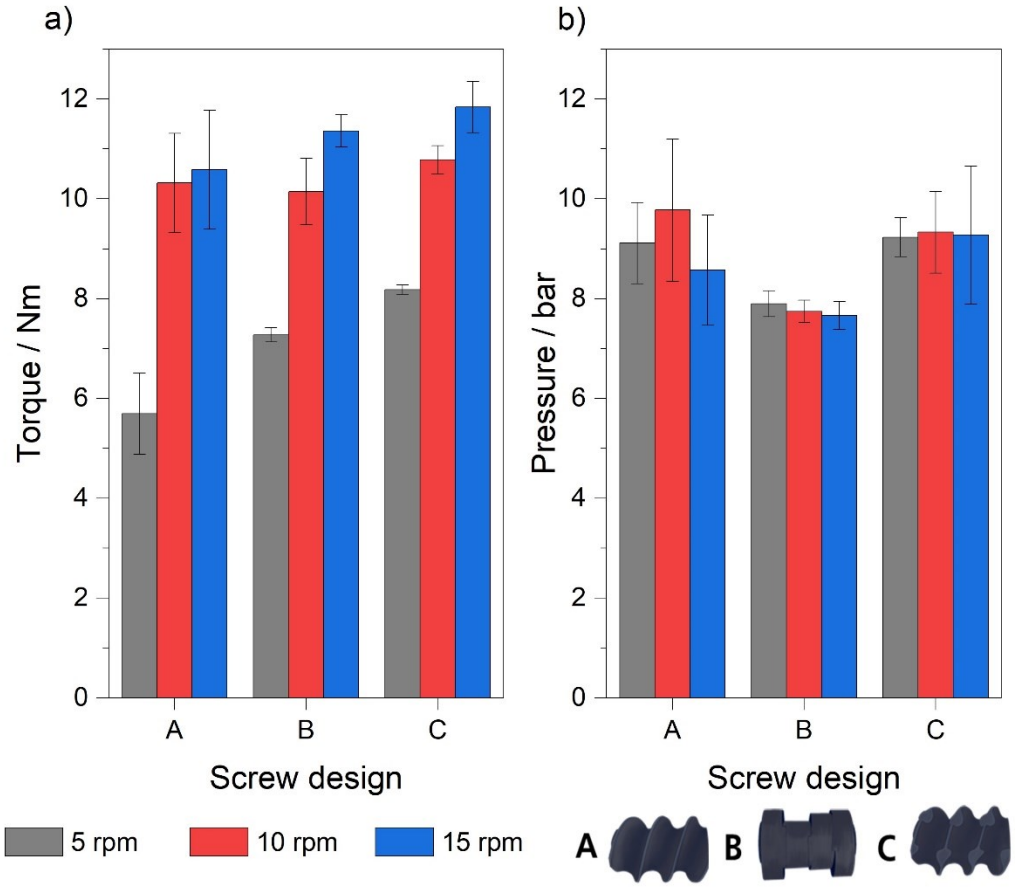

Figure 30: Measured torque (a) and pressure at the extruder die (b) during extrusion of a pre-mixed batch of PEO_{20}LiTFSI extracted from the last 10 minutes of the process dependent of the applied screw speed for each screw design.

The measured pressure at the extruder die is visualized in the right diagram in Figure 30 for all three screw designs as a function of the applied screw speed. The pressure does not show any significant change with the applied screw speed. Screw design B shows the lowest pressure with 7.7 – 7.9 bar, as well as the smallest error bar (< ± 3 N m) for all three screw speeds. The low pressure can be explained by the longer residence time of the material in the extruder barrel due to the kneading elements in the screw design and the associated plasticizing by mixing with LiTFSI. Kneading elements hold the material in front of each kneading block until there is sufficient material accumulation to push the material forward and overcome the retention force of the kneading block. In addition, dispersive mixing dominates around the kneading elements. Due to the higher shear effects, more energy is transferred into the polymer, resulting in a higher flowability of the material [155].

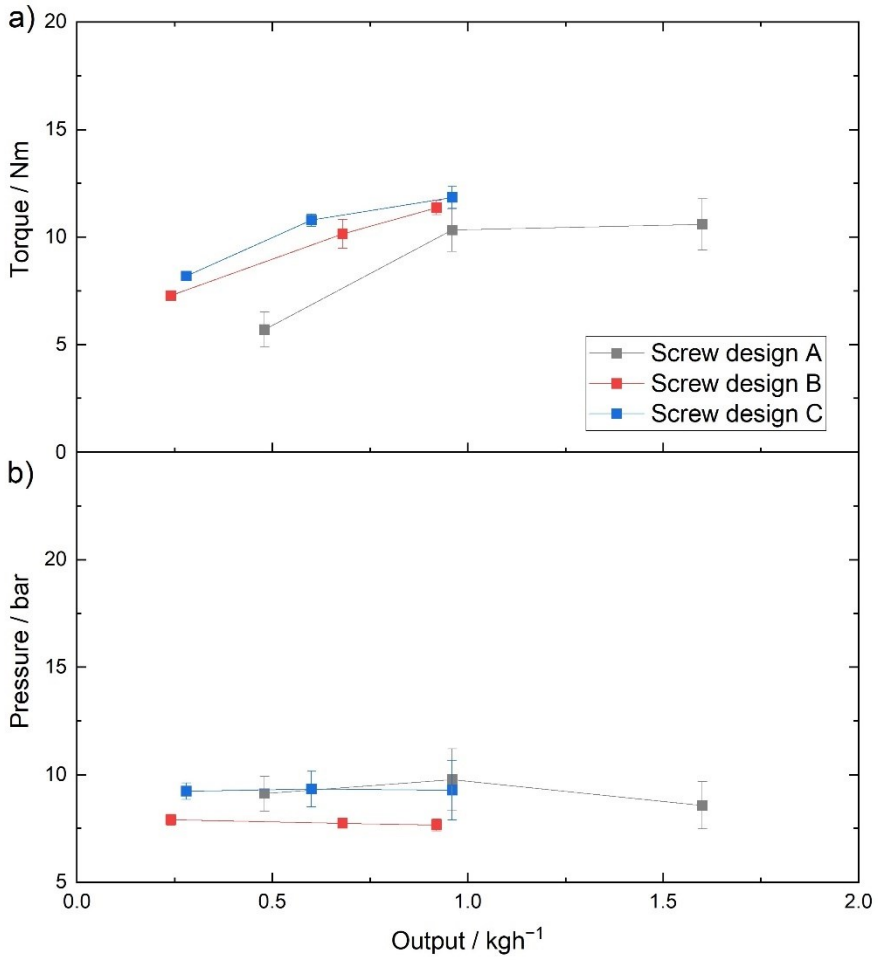

Figure 31: Correlation between extruder parameters measured during extrusion of a pre-mixed batch of PEO_{20}LiTFSI (E1) and material output.

As mentioned earlier the residence time plays an important role for the mixing. In this thesis, the residence time of the component is described by the material output. It is assumed that the higher the output per hour, the shorter the residence time. Furthermore, the output describes the upscaling capability for each screw design. Nevertheless, a good compromise must be found between high output and the material quality. Figure 31 shows the correlation between the measured process parameters and the material output. The diagram clearly shows that the output is strongly influenced by the screw design. Torque increases with higher output because the extruder engine must exert more energy to transport more material through the extruder. The pressure is more influenced by the screw designs themselves, resulting in lowest pressure for screw design B. As already mentioned earlier, screw design B has the longest residence time of the components characterized by the lowest overall output.

8.2 Product characterization

8.2.1 Digital microscopy observation

For product characterization, microscopic observations are made to determine the mixing and dissolution of LiTFSI into the polymer matrix during extrusion. Figure 32 shows microscopic images of extruded electrolytes as a function of the screw design used and the screw speed applied. For a better color representation, the RGB model of each sample is shown as a bar over the microscopic image. The samples show a color gradient indicating different mixing states depending on the screw design and applied screw speed. White PEO powder turns yellow after thermal treatment. As described in chapter 7.2.1, the darker the color, the more PEO is affected by degradation. The addition of LiTFSI causes the PEO to become wither and lighter in color. Therefore, the samples with a more yellowish hue are classified as poorly mixed and the samples with a whiter hue as well mixed.

All produced electrolytes show a smooth and shiny surface for all screw designs. This indicates that the polymeric material does not go through a degradation process during extrusion that damages the outer appearance of the material. All screw designs show different mixing results. The irregular shape of the extruded sample is a result of uneven pull-off during sample extraction. Since this does not affect the mixing during extrusion and the samples are post-processed by hot-pressing before electrochemical characterization, the shape of the sample is neglected in this work. Screw design A shows good mixing of the components at screw speeds of 5 and 15 rpm. The higher pressure at the extruder die at the

screw speed of 10 rpm (s. Figure 29) compared to the other screw speeds indicates that LiTFSI is not well dissolved in the PEO matrix. This is also indicated by the more yellowish color of the extruded electrolyte. While the mixing and dissolving of LiTFSI in the PEO matrix improves with higher screw speed for screw design B, the extruded electrolytes with screw design C show an opposite mixing and dissolving behavior.

The best mixing is shown for the screw design B with an applied screw speed of 15 rpm (Figure 32f)). Here, the kneading elements and the high shear stress improve the mixing and dissolution of LiTFSI in the PEO matrix, which is also characterized by the lowest pressure in Figure 29. In comparison, screw design C (Figure 32, i), with an applied screw speed of 15 rpm, shows the yellowest sample indicating poor mixing. Despite the use of mixing elements, this screw design does not seem to be suitable for the extrusion of PEO-based electrolytes, especially at high screw speeds.

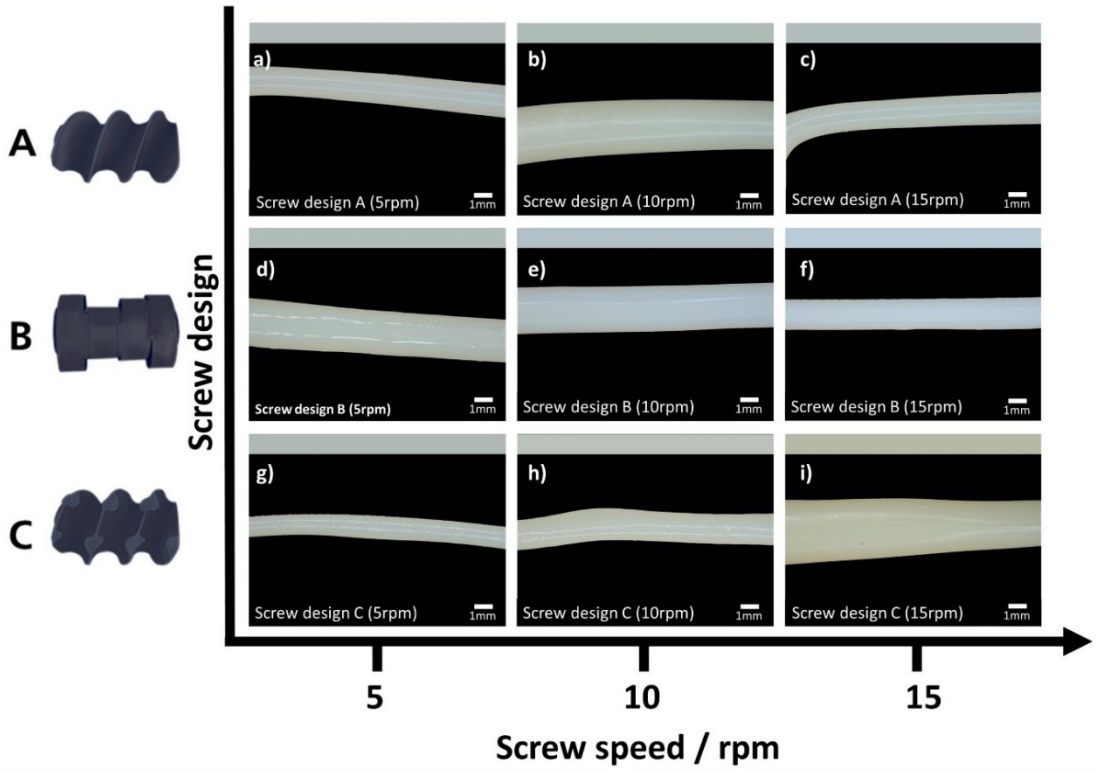

Figure 32: Digital microscopy images of extruded PEO-based electrolytes with different screw designs and applied screw speeds a)-c): screw design A, d)-f): screw design B and g)-i): screw design C. For a better determination of the color of each PEO-based electrolytes extruded with different screw designs and applied screw speeds white balancing was used. a)-c): screw design A at 5 – 15 rpm, d)-f): screw design B at 5 – 15 rpm and g)-i): screw design C at 5 – 15 rpm. The RGB model of each sample is shown as a bar over the microscopic image for a better color representation. Samples with a more yellowish hue are classified as poorly mixed and the samples with a whiter hue as well mixed.

8.2.2 Determination of molecular weight

The molecular weight (M_w) of the extruded polymer electrolytes is determined to determine whether the properties of the polymer are maintained or whether degradation in the form of chain scission occurs during extrusion. The M_w of each PEO-based electrolyte after extrusion is determined from the viscosity of a 5 wt %-aq. polymer solutions at 25 °C. The viscosity correlates with the determined M_w via GPC measurements from chapter 7.2.3 (p.62). By using this correlation it is possible to calculate the M_w from the viscosities of the electrolytes (s. Figure 18 from chapter 5.2.4.2, p.40).
Figure 33 shows a reduction in M_w after extrusion for all three screw designs and applied screw speeds. The extruded PEO-based electrolytes with screw design A show the largest reduction with 42 % (5 rpm). There is no real trend as a function of the screw speed. While screw design A shows no dependence on the screw speed, the M_w of PEO-based electrolytes decreases for screw design B to lower screw speeds and for screw design C at higher screw speeds.

Although Figure 29 shows a dependence of the measured torque and pressure on the applied screw speed, no correlation can be defined between the measured process parameter and the determined M_w for screw design A. This is different for the other two screw designs B and C. For screw design B, the measured process parameters indicate that more energy is transferred into the material with increasing screw speed, characterized by higher torque values and decreasing pressure at the die, but the determined M_w shows contradictory behavior. One would expect a similar dependence of M_w on the process parameters as seen for screw design C. Since the pressure at the extruder die does not depend on the screw speed, the dominant force is the torque of the screws themselves. As shown in Figure 29, the torque increases with rising screw speed, resulting in a decrease in M_w, indicating chain scission during extrusion. A reasonable explanation for the lower reduction in M_w is that LiTFSI is best dissolved with screw design B at 15 rpm, so that the TFSI-anion has the highest plasticizing effect. The extruded polymer electrolyte has a good flowability so that the polymer structure is not much destroyed by the kneading elements.

For a screw speed of 15 rpm, the M_w of the electrolytes shows that screw design B has the smallest reduction. This indicates that this extruder setup is the most suitable to maintain the polymer properties and at the same time, as shown in Figure 32 gives the best result in mixing the components while having the highest output for this screw design of 920 g (s, Table 1).

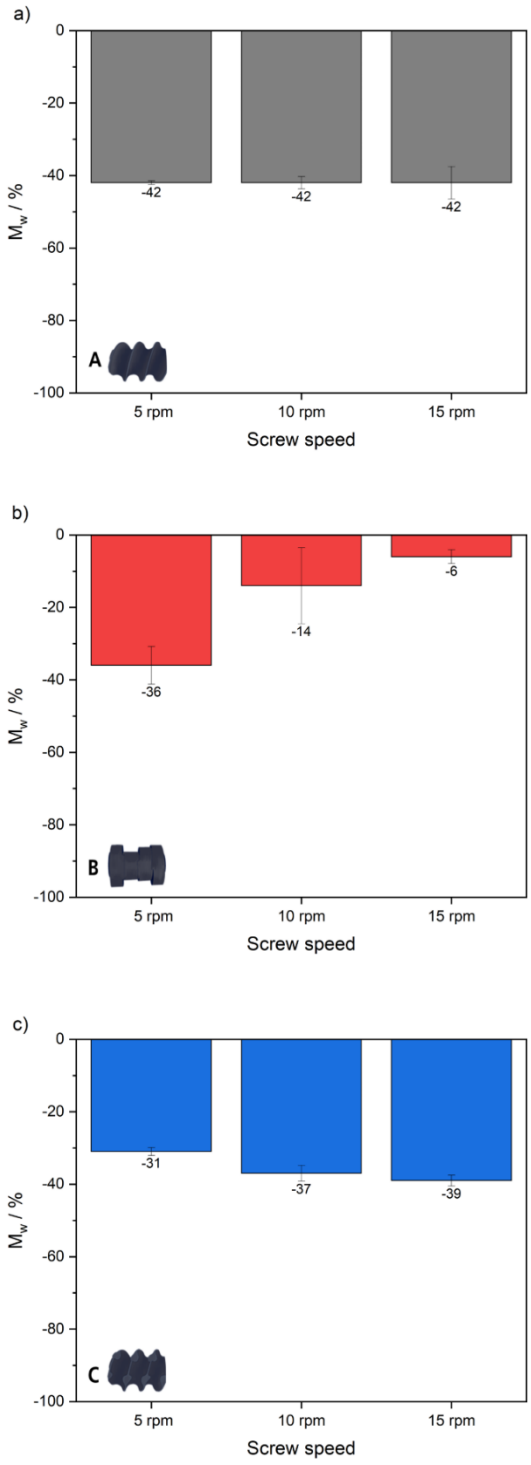

Figure 33: The percentage reduction in molecular weight of extruded PEO-based electrolytes dependent on the screw design. a) screw design A; b) screw design B; c) screw design C and the applied screw speed compared to the molecular weight of pristine PEO (pristine PEO= 0 %).

8.2.3 Thermo-mechanical properties

The thermo-mechanical properties of the electrolytes produced are an important parameter in terms of both process technology and application technology. For process technology it is important to know the mechanical strength of the electrolyte in order to set the correct parameters for pulling off the material with a winding machine, for example. For the application technology it is important to determine the mechanical strength at application temperature to better evaluate its performance in a full cell. Therefore, in this work the mechanical properties of the produced electrolytes are determined for a temperature range of 20 – 100 °C.

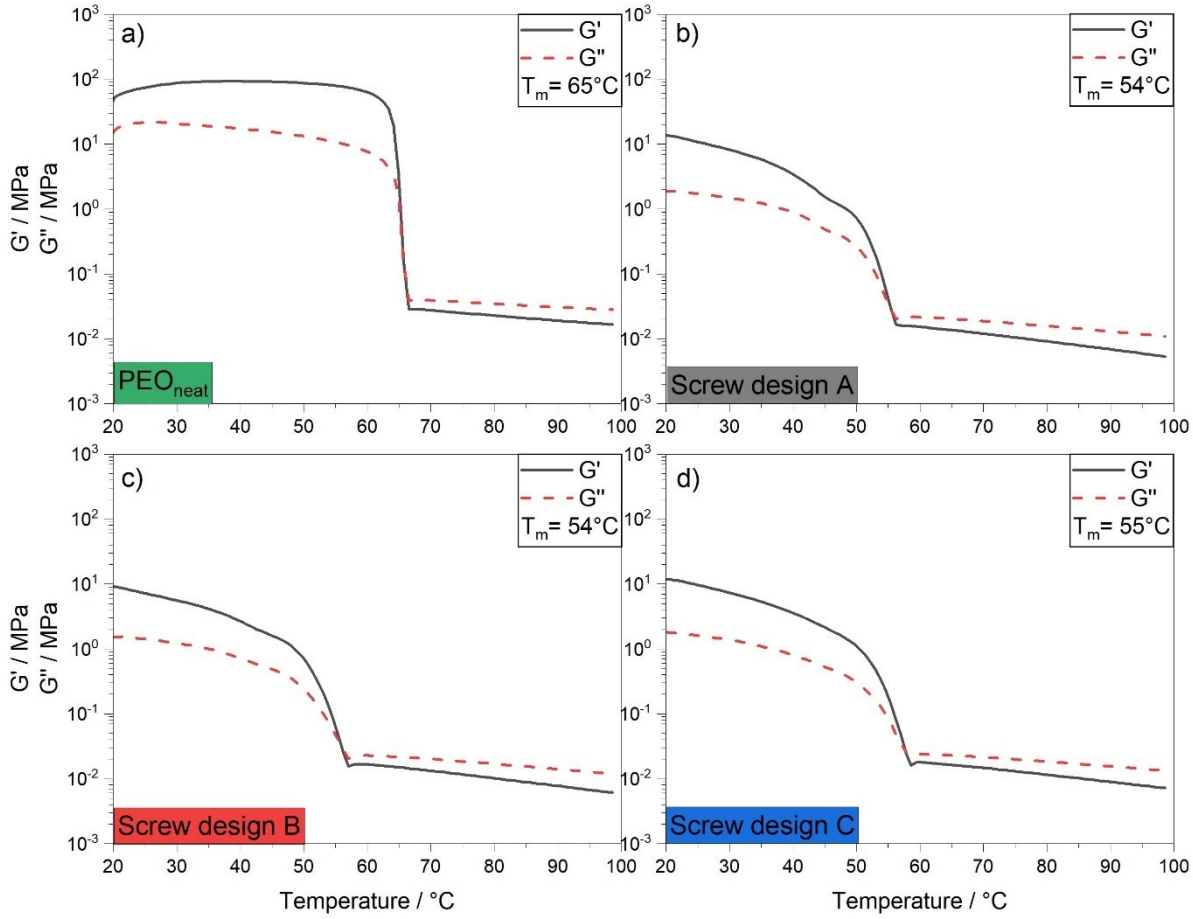

Figure 34: Temperature-dependent storage modulus G' (solid line) and loss modulus G" (dotted line) for neat PEO and extruded PEO-based electrolytes with different screw designs at a screw speed of 15 rpm. a) neat PEO; b) PEO-based electrolyte extruded with screw design A; c) PEO-based electrolyte extruded with screw design B; d) PEO-based electrolyte extruded with screw design C.

Figure 34 shows the determined temperature-dependent mechanical properties using DMA. The storage modulus (G') and the loss modulus (G') are depicted for neat PEO and the

extruded PEO-based electrolytes using different screw designs and a screw speed of 15 rpm. G' and G'' represent the elastic and viscous portion of the material, respectively. The melting temperature (T_m) of each sample is determined by the onset of the drop in the G' curve.

The curves of all investigated samples can be divided into two sections. The first section ($T < T_m$) is dominated by the elastic portion ($G' > G''$) of the materials. The samples are in solid-state. In the second section ($T > T_m$), the viscous portion ($G' < G''$) dominates. The samples are in liquid-state/molten-state. The melting of PEO is characterized by the large drop in both curves and in the huge loss of mechanical strength. The PEO-based electrolytes show a melting temperature 10°C lower than PEO without conducting salt. This is due to the incorporation of the conducting salt. In addition, all PEO-based electrolytes produced exhibit lower stiffness than pure PEO over the whole temperature range. This is also attributed to the conductive salt, which acts as a plasticizer and reduces the mechanical properties of the PEO. The stiffness in the melt is slightly different for all four samples. However, the PEO-based electrolyte produced with screw design C has higher G' and G'' values compared to the electrolytes produced with screw design A and B. This indicates that less LiTFSI is mixed into the polymer, making it less soft than the other electrolytes and reinforces the findings of the microscopic characterization (Figure 32, i)).

8.2.4 Electrochemical characterization

Electrochemical impedance spectroscopy at 80 °C is used to determine the ionic conductivity (σ_{ionic}) of the PEO-based electrolytes.

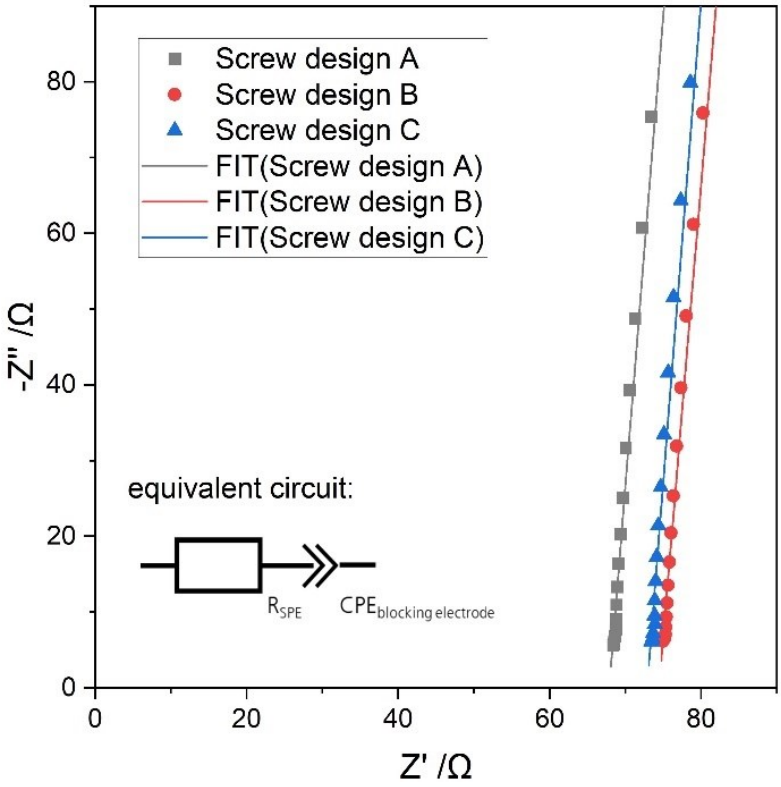

Figure 35: Exemplary Nyquist plot of impedance measurement of PEO-based electrolytes at 80 °C extruded with different screw designs and an applied screw speed of 15 rpm.

Figure 35 shows an exemplary Nyquist plot for PEO-based electrolytes at 80 °C as a function of different screw designs. As the measurement temperature is higher than the melting temperature of the produced electrolytes ($T_{measurement}$= 80 °C>>$T_{m\text{-}electrolyte}$= 54/55 °C, s. Figure 34), no semicircle is visible. For the determination of the intersection with the x-axis (Z'/Ω) an equivalent circuit consisting of just a R-element and a CPE-element is used for fitting. The resistance R_{SPE} is attributed to the ionic resistance originating from the polymer electrolyte and the CPE-element to the capacitive properties of blocking electrode. As shown in Figure 35 all Nyquist plots show low resistance (Z' < 80 Ω) due higher ion mobility in the polymer melt. The conductivity can be calculated with equation with r= 0.4 cm and the sample thickness (d_{SPE}) that was determined after EIS measurement.

$$\sigma_{ionic} = \frac{d_{SPE}}{\pi \times r^2} \times R_{SPE} \tag{8.1}$$

Figure 36 shows σ_{ionic} for PEO-based electrolytes as a function of their molar ratio (EO:Li) and their preparation extracted from literature [14,26,121,151,156–160]. All produced PEO-based electrolytes show σ_{ionic} of (1.1 x 10^{-4} – 1.8 x 10^{-4}) S cm^{-1} at 80 °C, which is comparable to literature indicating successful production of PEO-based electrolytes. The diagram clearly shows that solvent-based electrolyte preparation is still widely used in research as solvent-free preparation methods covering a wide range of mixing ratios. The solvent-based prepared electrolytes presented are generally prepared by solvent casting of dissolved PEO and LiTFSI in acetonitrile [151,152,159,160]. The solvent-free preparations are done by mechanical mixing or hot-pressing at 100 - 120 °C [26,121,157] or simple pressing [158] of the components. Nevertheless, the presented σ_{ionic} shows no clear trend depending on the sample preparation. Thus, that it is even possible to compare σ_{ionic} of electrolytes produced in this work with σ_{ionic} electrolyte prepared by solvent-based method from literature.

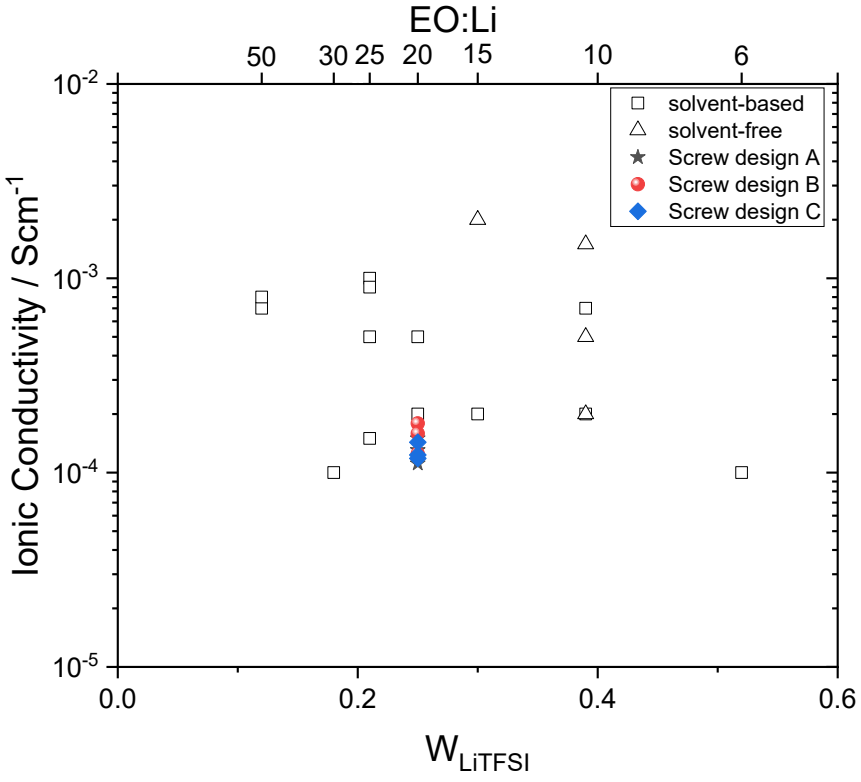

Figure 36: Ionic conductivity (σ_{ionic}) at 80 °C of extruded PEO-based electrolytes of the first extruder setup (E1) compared literature values of σ_{ionic} at 80 °C of PEO-based electrolytes produced solvent based (rectangles) [14,151,152,156,159,160] and solvent free (triangles) [26,121,157,158].

8.3 Conclusion

In this chapter, a pre-mixed batch of PEO and LiTFSI powders with a molar ratio of 20:1 (EO:Li) is successfully extruded at a process temperature of 90 °C to produce solvent-free PEO-based electrolytes. The extrusion experiments clearly show the effect of extruder setup on process and product quality, so that the following conclusions can be drawn:

- The monitored process parameters, torque, and pressure, show a dependence on the screw design and the applied speeds. While the torque increases with increasing screw speed and shows the smallest error at 5 rpm, the pressure at the extruder die shows no significant change with the applied screw speed.
- The most stable process, characterized by the smallest error bar of the monitored pressure, is achieved with screw design B.
- Microscopic observation shows that screw design B. achieves the best mixing of PEO and LiTFSI, especially at high screw speeds.
- The determination of M_w also shows that screw design B gives the best result at high screw speeds. Here, we see the least loss of M_w indicating that this screw design best maintains the polymer properties during extrusion.
- All produced PEO-based electrolytes exhibit an ionic conductivity of $(1.1 \times 10^{-4} – 1.8 \times 10^{-4})$ S cm^{-1} at 80 °C, which is comparable with the literature indicating successful extrusion of PEO-based solid electrolytes.

All in all, the comparison of the screw designs shows that the screw design B, which contains kneading elements, is the most promising candidate for upscaling dry production of polymer-based SEs by extrusion.

9. Extrusion of PEO-based electrolytes using two feeders

This chapter presents the results of the second extruder setup E2, where PEO and LiTFSI powders are added separately to the extrusion process. In contrast to the first extruder setup E1, the LiTFSI powder is added to the PEO melt via the second feeder. Adding the components through two feeders gives freedom to adjust the composition. In addition, this extruder setup does not require a pre-mixing step, which reduces production costs (slurry mixing: 7,396,000 $ per year (7.91 %) and 0.11 kWh per cell (0.83 %) [134]). These advantages make this extruder setup very promising for upscaling. It is therefore important to understand how a separate addition of the components, and thus different residence times of each material in the extruder barrel, affects the process and product quality.

9.1 Process characterization

As in the case of the pre-mixed PEO-based SE extruder experiments, the process parameters are continuously monitored after the extruder is started and the barrel is filled with both materials. Since the minimum residence time of 17 minutes at low kneading speed (5 min^{-1}, s. Figure 22 on p. 51) required for complete melting of PEO is known from the kneading experiments, the extraction of the torque and pressure data for the last 10 minutes remains the same as for E1. Again, the size of the error bars characterizes the process stability.

Figure 37 shows the measured process parameters for the three screw designs as a function of the applied screw speeds. The torque shown in the left diagram of Figure 37 is dependent on the applied screw speed. The torque increases with the applied screw speed for all three screw designs. When comparing the measured torque dependent on the screw design, screw design A shows the highest torque over all screw speeds. The largest different of 19 % is between screw design A and screw design C. It appears that with screw design A, the engine of the extruder requires more energy to move the material through the barrel. A possible cause is the overall shorter dissolution and mixing time of LiTFSI in PEO. Compared to the screw designs B and C, where the kneading and mixing elements transfer more energy into the material to improve the mixing, the screw design A consists only of conveying elements with lower energy transfer from the screws. The smallest error bars with < 0.55 N m and, thus, the most stable process can be observed for screw design B for all screw speeds. This indicates that LiTFSI is best dissolved and mixed into the polymer melt with kneading elements. Compared

to the other screw designs, screw design B obtains the lowest overall output at all screw speeds (Table 1, p. 32). As a result, the material remains in the extruder barrel the longest, which improves the mixing of the components.

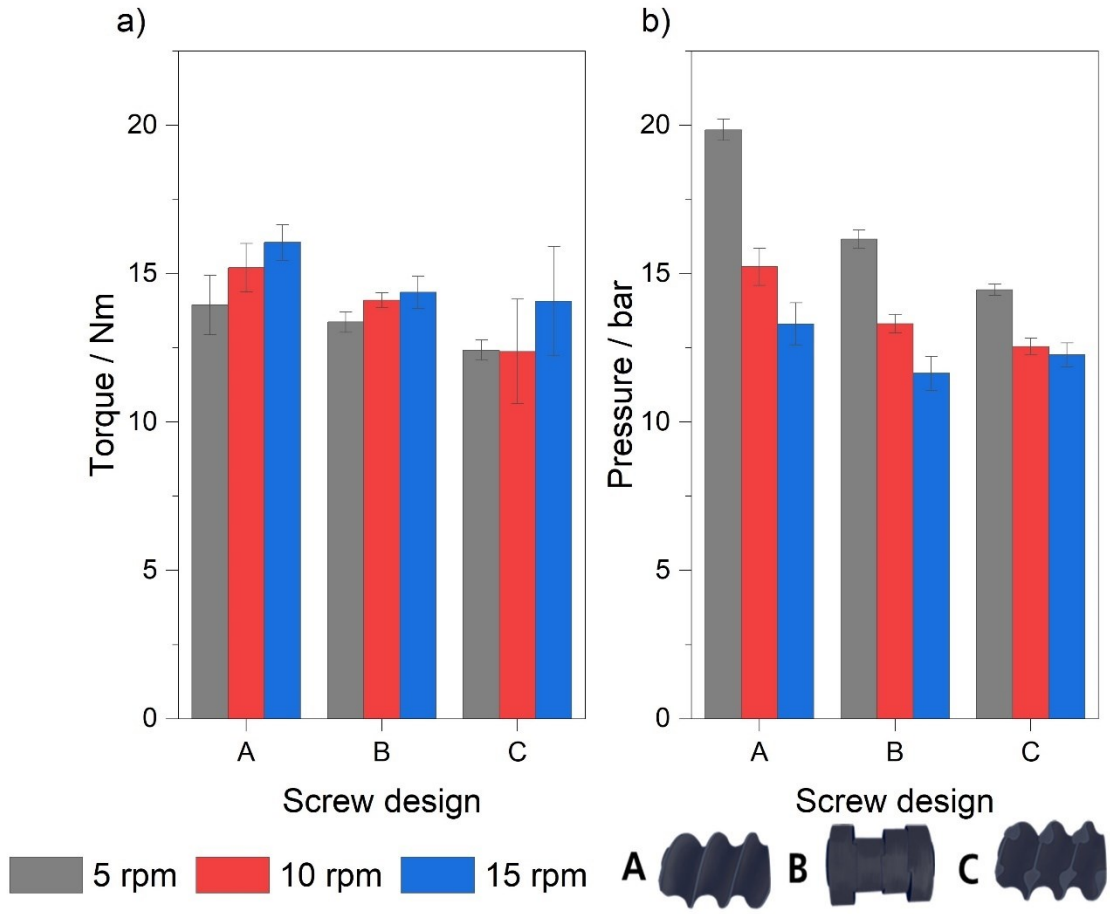

Figure 37: Measured torque a) and pressure at the extruder die b) during extrusion using two feeders extracted from the last 10 minutes of the process dependent of the applied screw speed for each screw design.

Comparing the measured torque with the extruder experiments of E1 from chapter 8.1 (s. Figure 30), the values measured here are higher for all screw designs. In general, screw design A shows the greatest difference at all screw speeds, with the highest distraction of 8.3 N m at a screw speed of 5 rpm. The shorter residence time of the materials is also noticeable here. While for the components of the pre-mixed batch have already undergone 30 minutes of energy input during mixing with the TURBULA® mixer, the components here are untreated without any energy input. Further, as known from the kneading experiments (chapter 7.1.2) LiTFSI acts as a plasticizer improving the flowability of PEO. Because the components are added separately, PEO is melted first and the plasticizing effect occurs only after LiTFSI is added, which is about halfway down the extruder barrel. The installation

position of the kneading and mixing elements for screw design B and C, respectively, after the filling position of LiTFSI, improves the mixing and dissolving of LiTFSI, which is characterized by a lower discrepancy (< 6 N m) compared to the first extruder setup. A higher screw speed also improves the mixing and hence the flowability of PEO. For example, for screw design A, the discrepancy is reduced from 8.3 N m (5 rpm) to 5.5 N m (15 rpm) and for the other screw design we see a reduction of the discrepancy by half. Although screw design C shows the smallest discrepancy to the torque values of the first extruder setup, the high fluctuation, especially at high screw speeds of 1.8 N m, does indicate an instable process. Furthermore, the microscopic observation of screw design C of E1 (Figure 32) shows an undesirable poor dissolution of LiTFSI in PEO. Thus, a small discrepancy between the monitored torque values of the different extruder setups is not a sufficient criterion. More important here is the stability of the process itself.

The right-hand diagram in Figure 37 shows the measured pressure at the extruder die for all three screw designs as a function of the applied screw speed. The pressure is influenced by both, the screw design and the applied screw speed. The pressure decreases at higher screw speeds for all screw designs. Here, at low screw speed (5 rpm), the highest pressure of 19.9 bar is achieved with screw design A and the lowest pressure (16.1 bar) is achieved with screw design C. At high screw speed of 15 rpm, the lowest pressure of 11.6 bar is achieved with screw design B. The decrease in pressure at high screw speed is in accordance with the measured torque and the accompanying higher energy transfer of the screws improving the flowability of PEO. All determined error bars are < 1 bar at screw speeds of 10 and 15 rpm, and at low screw speeds of 5 rpm the error is even < 0.5 bar for all screw designs. This indicates that adding the components separately does not affect the pressure as much as it does the torque. The pressure is measured at the extruder die, i.e. at the end of the extrusion process. As known from the microscopic observations of E1, Figure 32 on p, 69, LiTFSI should be dissolved and homogenously mixed in the PEO matrix at the end of extrusion. Thus, the pressure indicates the flowability of the polymer melt and how evenly LiTFSI has been added and dissolved along the PEO string. In addition, a stable pressure also indicates a stable material output.

Compared to the measured pressure of E1 (Chapter 8.1, Figure 30), the measured pressure is overall higher for all screw designs. While the pressure does not show any real dependence on the applied screw speeds for extruder setup one, it shows that the screw speeds have a stronger influence on the material flowability and dissolution of LiTFSI when the components

are added separately. The plasticizing effect of LiTFSI becomes stronger with higher applied screw speed. The measured pressure at low screw speed (5 rpm) shows the highest discrepancy (screw design A: 54%; screw design B: 51%; screw design C: 36%) between the two extruder setups. This discrepancy between the two experiments is reduced for all screw designs (screw design A: 36%; screw design B: 34%; screw design C: 24%) at higher screw speeds. On the one hand, the high pressure results from the shorter residence time of both materials in the extruder barrel for mixing and dissolving. Therefore, the flowability of the PEO is generally lower compared to E1, which can also be observed by the torque, which characterizes the energy required from the extruder engine to rotate the screws and move the material along the extruder. On the other hand, the flowability of the PEO and the mixing of LiTFSI is strongly influenced by the screw speed. At low screw speed, the energy input appears to be insufficient to improve the flowability of the PEO. This energy input with increasing screw speed that improves the flowability and the mixing and dissolving of LiTFSI.

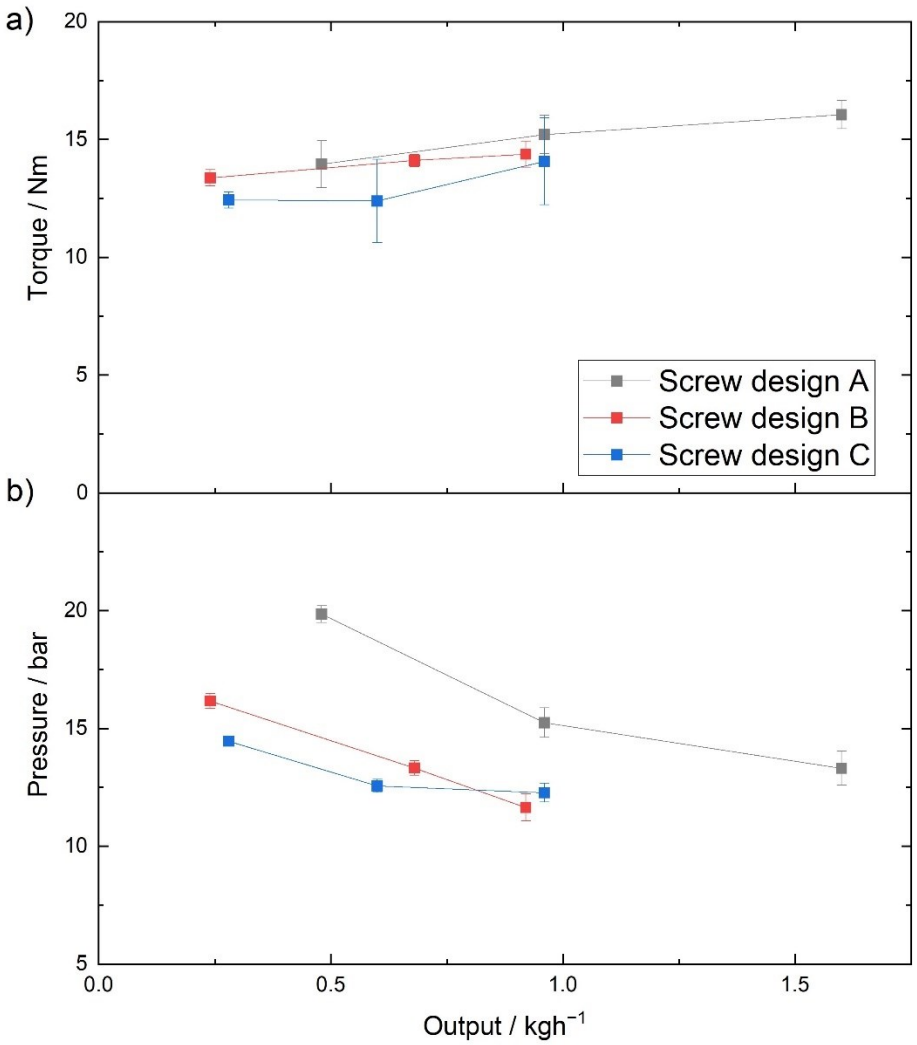

Figure 38: Correlation between extruder parameters measured during extrusion of separate addition of PEO and LiTFSI and material output.

As described in extruder experiment E1, the residence time plays an important role in the mixing, which is characterized by the material output depending on the screw speed. Figure 38 shows the measured process parameters as a function of the material output. The dependency between torque and output stays the same as for the extruder setup E1 since the overall output is unchanged. The torque increases with higher output because more energy is required to transport the material. The relation between pressure and output differs from extruder setup E1, due to the strong effect of the screw speed on the pressure and its influence on the flowability of the PEO. The flowability is more influenced due to the separate material addition of the components. So, the plasticizing effect of LiTFSI occurs later and it is more affected by the screw speed. Further, the replacement of the conveying elements with a kneading or mixing element reduces the pressure up to 5.1 bar when comparing screw design

A with C at 5 rpm. Screw design A has the highest overall pressure because it transports more material through the extruder barrel at given screw speed, as shown Figure 38.

9.2 Product characterization

9.2.1 Digital microscopy observation

An independent material addition of the components using feeders at different position strongly affects the mixing time of the components compared to a pre-mixed batch. The components have less time in the barrel to get mixed. Therefore, product characterization, such as the microscopy used here, is important to evaluate whether the mixing time is sufficient for good dissolution of LiTFSI in the polymer matrix and homogeneous mixing of the components.

Figure 39 shows the microscopic images of the extruded PEO-based electrolytes using an independent material addition as a function of the screw design and the applied screw speed. As for microscopic observation of the first extrusion experiments (s. chapter 8.2.1) the RGB model represents the color as a bar over each image. Again, the samples with a more yellowish hue are classified as poorly mixed and the samples with a whiter hue as well mixed.

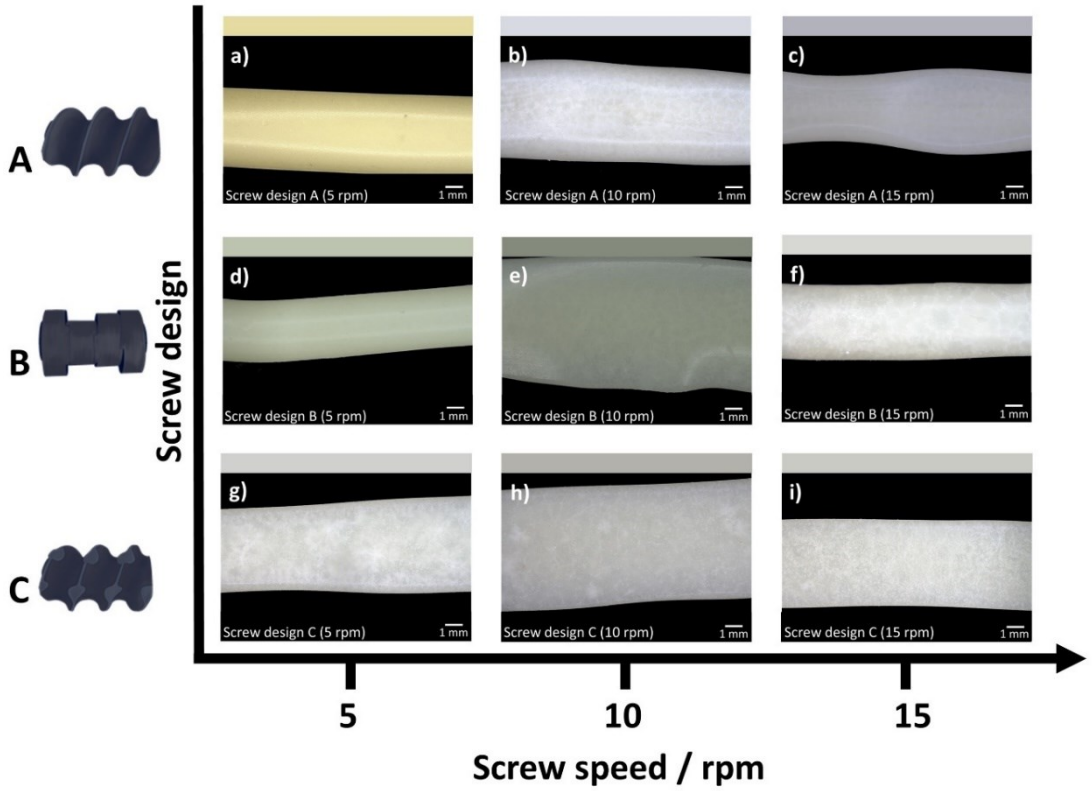

Figure 39: Digital microscopy images of extruded PEO-based electrolytes using two feeders for independent material addition (E2). For a better determination of the color of each PEO-based electrolytes extruded with different screw designs and applied screw speeds white balancing was used. a)-c): screw design A at 5 – 15 rpm, d)-f): screw design B at 5 – 15 rpm and g)-i): screw design C at 5 – 15 rpm. The RGB model of each sample is shown as a bar over the microscopic image for a better color representation. Samples with a more yellowish hue are classified as poorly mixed and the samples with a whiter hue as well mixed.

Microscopic images show that all produced PEO-based electrolytes have a smooth and shiny surface for all screw designs and screw speeds applied. There is no visible degradation or melt fracture occurs during extrusion to change the material appearance. As for the extruded pre-mixed batches, all screw designs show different mixing results. The shape of the produced electrolytes is neglected due to their uneven pull-off during sample extraction.

Screw design A (Figure 39, b) & c)) shows good mixing of the components at screw speeds of 10 and 15 rpm. The extruded electrolyte at 5 rpm (Figure 39, a)) has a very yellow color indicating that LiTFSI is not well dissolved and mixed into the polymer matrix. It appears that the time was not sufficient for a good mixing. This is also confirmed by the pressure measured during extrusion, which is relatively high at 19.9 ± 0.4 bar compared to the pressure measured at higher screw speeds.

For the screw designs B and C, none of the extruded PEO-based electrolytes show the yellow color of the electrolyte extruded with screw design A at 5 rpm (Figure 39, a). Although there is a slight difference in color and light is visible, it can be stated that LiTFSI is dissolved in all extruded PEO-based electrolytes with both screw designs B and C. The best dissolution and mixing are achieved with high screw speed of 15 rpm for both screw designs. This indicates that kneading or mixing elements are necessary for extrusion process with independent material addition to extend the residence time of the components and transfer more energy into the material to improve the mixing. Further, high screw speeds increase the energy transfer of these elements enhancing the dissolution and mixing. These findings are supported by the measured process parameters in Figure 37. Here, the better energy transfer and dissolution of LiTFSI is characterized by the decrease in pressure with increasing screw speed for both screw designs. However, screw design B shows the most stable process, which makes it more suitable for the extrusion process with independent material addition and gives a chance to scale up the process with higher screw speed.

Comparing the microscopic images in Figure 39 of E2 with those of E1 (s. Figure 32), it can be observed that the extruded PEO-based electrolytes with independent material addition show a white pattern along the sample, especially at high screw speeds for screw designs A and B (Figure 39, b)+c); e)+f)) and for all screw speeds for screw design C (Figure 39, g)-i)). This white pattern can be not well dissolved LiTFSI, indicating that the residence time is too short for a proper dissolution of LiTFSI. However, the regularity of the pattern suggests homogenous distribution of LiTFSI within the polymer matrix. Since this phenomenon occurs with all screw designs, they are not sufficient for proper dissolution of LiTFSI into the PEO matrix using independent material addition in their current setup. It is suggested that the screw designs need to be optimized by adding more kneading elements or reversing screw elements to extend the residence time and to improve the dissolution and mixing of LiTFSI [161]. When evaluating the given screw designs in their current setup, screw design B appears to be the most suitable for the dry production of PEO-based electrolytes.

9.2.2 Determination of the molecular weight

As with the mixing quality (s. chapter 9.2.1), the different sample preparation and the independent addition to the extrusion process, and thus the different residence time of the components, may affect the product stability of PEO during the extrusion. To evaluate the material stability during extrusion and the effect of different extruder setup, the M_w is determined by rheology measurement as described in chapter 5.2.4.2.

Figure 40 shows the percentage reduction in M_w for all PEO-based electrolytes produced using an independent material addition compared to neat PEO. A reduction in M_w is observed for all applied screw speeds for all screw designs. For screw design A (Figure 40 a)) and screw design B (Figure 40 b)), the reduction in M_w is the greatest at higher screw speeds. This dependence is particularly pronounced for screw design A. The extruded PEO-based electrolyte at 5 rpm shows the smallest overall reduction in M_w of 7 % compared to the high screw speed (15 rpm) which shows a reduction in M_w of 29 %. On the one hand, this difference in M_w is due to the lower shear stresses transferred to the polymeric material at lower screw speeds. On the other hand, as shown in the microscopic images in Figure 39 (a), d), g)), less LiTFSI is dissolved in the PEO matrix at low screw speed. The overlapping effects of plasticization and degradation, as shown in the kneading experiments (s. chapter 7.2.3), are therefore less pronounced at lower screw speeds.

Compared to screw design A, screw design B shows a less pronounced relationship between the reduction in M_w and the applied screw speed. Already at low screw speed, the extruded PEO-based electrolyte shows a reduction in M_w of 22 %. The reduction at high screw speed (15 rpm) of 31 % is similar to that of the extruded electrolyte with screw design A. The overall more pronounced reduction in M_w is due to the higher shear rate of the kneading element in the screw design. This leads to a better dissolution of the LiTFSI into the polymer matrix (s. Figure 39, b), e) and h)) at all applied screw speeds and at the same time the higher energy input into the material could lead to a higher degradation of the polymer itself.

In contrast to the described screw designs, screw design C (Figure 40 c)) shows a completely different material behavior. All produced PEO-based electrolytes show a reduction in M_w of 28 % compared to neat PEO. For screw design C, the material stability is independent of the applied screw speed. Although, the process parameters presented in chapter 9.1 show a similar dependency on the applied screw speeds as the other screw designs, indicating better

mixing and dissolution at higher screw speeds, the influence of the mixing elements on the material stability remains unchanged.

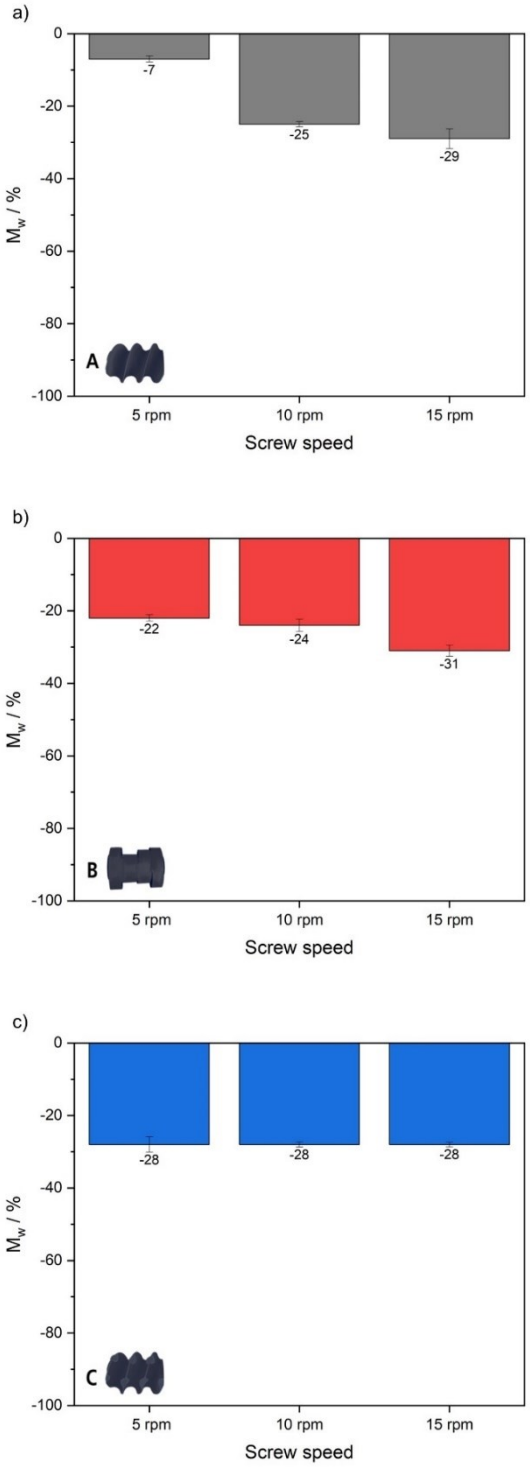

Figure 40: The percentage reduction in molecular weight of extruded PEO-based electrolytes using two feeders for independent material addition dependent on the screw design (a) screw design A; b) screw design B; c) screw design C) and the applied screw speed compared to the molecular weight of pristine PEO.

The comparison between the screw designs also shows that the implementation of kneading and mixing elements provokes more degradation of the polymer at low screw speeds. The similar M_w loss at 15 rpm for all screw designs suggests a maximum expected M_w reduction at higher screw speeds. Thus, the used screw designs in this work are suitable for upscaling the process by increasing the screw speed.

Comparing the calculated M_w of E2 with the calculated M_w of the first extruder setup E1, it appears that the material addition also affects the material stability during the extrusion. While the M_w of each extruded electrolyte of the premixed batch with screw configuration A (Figure 33, a)) shows an overall a reduction of 42 % independent of the screw speed, the M_w of the extruded electrolyte using the independent material addition shows a dependence on the applied screw speed. The reduction increases from 7 % to 29 % with increasing screw speed. On the one hand side, this indicates that the premixed batch is more sensitive to thermal processing than when the components are added separately to the process. On the other hand, it also indicates that the screw speeds have a greater effect on the material stability when they are added separately. A possible reason for the different material stability can be the different length of common time of the materials. In the premixed batch, the materials have already spent time together during the mixing step and are exposed towards mechanical stresses together during the rotational mixing. Further, the mixed powders are then exposed to thermal and mechanical stresses together during the whole extrusion time. So LiTFSI has more time to get dissolved and to plasticized PEO.

For screw design B a different effect of the material addition is observed. The materials stability shows a reversed dependence of the screw speeds. Whereas for E1 setup the M_w the screw speed leads to less reduction (36 % (5 rpm) to 6 % (15 rpm), Figure 33,b)) the screw speed for the E2 leads to more reduction in M_w (22 % (5rpm) to 31 % (15 rpm). Figure 40 b)). One reason for this material behavior may be the common time of the materials and the resulting better dissolution of LiTFSI as mentioned above. Another reason may be that the kneading elements have a greater effect on the PEO due to the less dissolved LiTFSI and plasticized PEO. With less LiTFSI dissolved in the PEO matrix, the polymer has less flowability than in E1. Therefore, the shear forces of the kneading elements cannot be dissipated as well as in E1, leading to higher degradation processes, especially at high screw speeds.

Comparing the M_w of the third screw design C, Figure 33 c) with Figure 40 c), another material behavior can be observed. While M_w shows a slightly reduction with increasing screw speed for E1 (31 % (5 rpm) to 39 % (15 rpm)), the M_w for E2 shows an overall reduction of 28 % for all screw speeds. This indicates that the mixing elements have a higher impact on the pre-mixed batch than on the separately added materials.

In general, the comparison of the two extruder setups shows that the material addition affects the material stability during the extrusion process as well as its sensitivity to the screw design used and the screw speed. However, for E2, the effect of screw design seems to have no influence on the material stability at high screw speed. This is very promising in terms of upscaling and gives some freedom in screw design for the production of PEO-based electrolytes. Nevertheless, a reduction in molar mass and thus a loss of mechanical properties must always be expected, regardless of the material feed. This means that a good compromise must be found in the extruder setup in order to achieve high throughput with little loss of mechanical stability.

9.2.3 Thermo-mechanical properties

The thermo-mechanical properties are determined exemplary for the electrolytes produced at a screw speed of 15 rpm. As for E1, G' and G'' provide information about the elastic and viscous nature of the electrolyte dependent on the temperature, as well as thermal properties such as T_m of the produced electrolytes.

The determined temperature-dependent mechanical properties of the produced electrolytes compared to neat PEO are shown in Figure 41. As for E1, the melting temperature (T_m) of each sample is determined by the onset of the drop in the G' curve. The curves also can be divided by T_m in two sections: 1st section: $T < T_m$ and 2nd section: $T < T_m$. Below T_m of each electrolyte, the samples are in solid-state characterized by G' > G''. At temperature above T_m the viscous portion (G'') of the material is more pronounced and the samples are in liquid-state/molten-state. For all samples the melting of PEO is characterized by the large drop in G' and G'' and their huge loss in mechanical strength. The electrolytes produced with screw design A and C show a T_m around 10 °C lower than neat PEO. The electrolyte produced with screw design B shows with T_m= 43 °C the largest discrepancy to neat PEO. The reduction in M_w determined for all samples in the previous chapter 9.2.2 is not significantly different.

Thus, it cannot be the reason for the large reduction of T_m of the electrolytes produced with screw design B. The monitored pressure from chapter 9.1 and the microscopic observations from Figure 39 show that screw design B provides a better LiTFSI incorporation into the polymer characterized by lower pressure in the process parameters and lighter appearance of the electrolyte produced. This leads to a greater plasticizing effect and inhibition of crystallization of PEO by the TFSI-anion. These two effects reasonably explain the greater reduction in T_m for screw design B.

In addition, all PEO-based electrolytes produced exhibit lower stiffness than pure PEO over the whole temperature range. This is also attributed to the conductive salt, which acts as a plasticizer and reduces the mechanical properties of the PEO. The stiffness in the melt is slightly different for all four samples.

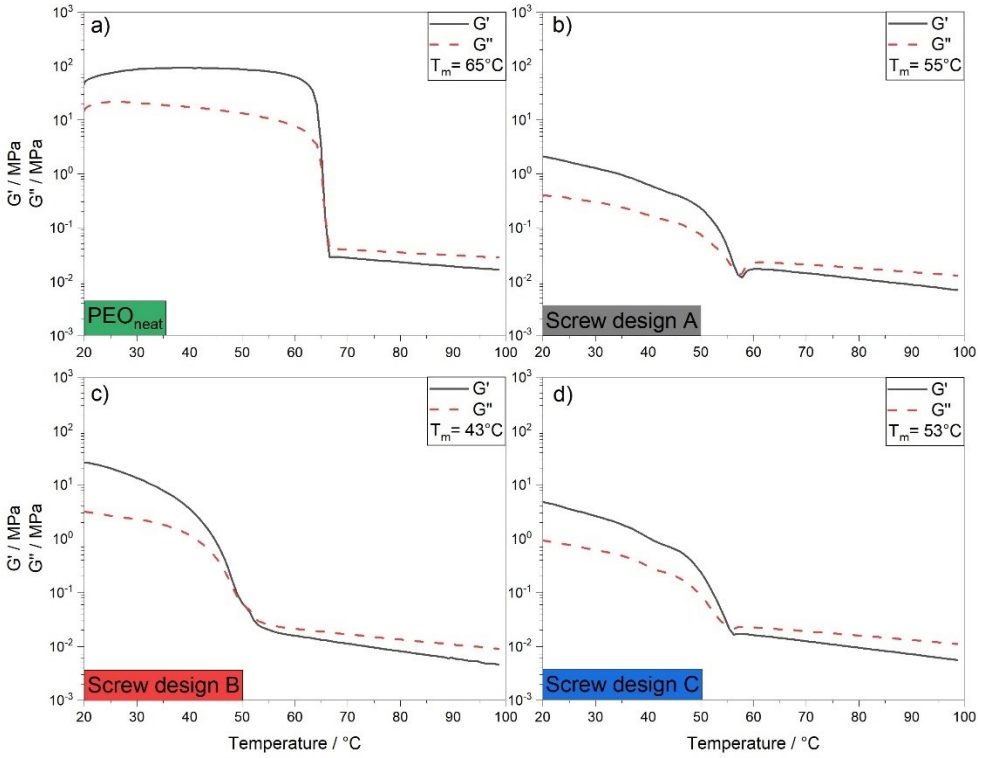

Figure 41: Temperature-dependent storage modulus G' (solid line) and loss modulus G" (dotted line) for neat PEO and extruded PEO-based electrolytes of E2 with different screw designs at a screw speed of 15 rpm. a) neat PEO; b) PEO-based electrolyte extruded with screw design A; c) PEO-based electrolyte extruded with screw design B; d) PEO-based electrolyte extruded with screw design C.

9.2.4 Electrochemical characterization

As with the extruded PEO-based electrolytes of the first extruder setup E1, EIS is used to determine the σ_{ionic} of the electrolytes. In addition, σ_{ionic} was determined every 10 °C from 80 °C to 20 °C to investigate the temperature dependence of the σ_{ionic}. The electrolyte was heated up to 80 °C and equilibrated for 55 minutes prior to measurement. The σ_{ionic} is expected to decrease at lower temperature due to the increasing resistance resulting from the recrystallization processes of PEO.

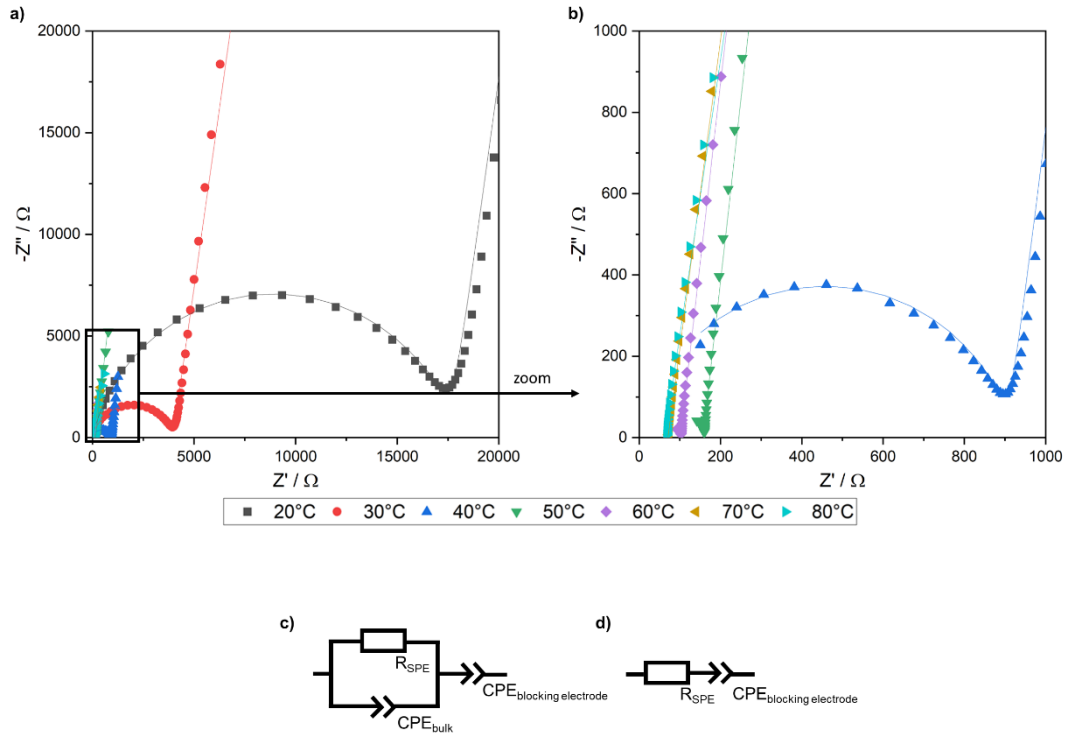

Figure 42: Exemplary temperature-dependent Nyquist plot of PEO-based electrolyte produced with screw configuration A at 15 rpm. a) Nyquist plot of the whole temperature range 20 to 80 °C; b) zoom of the Nyquist plot for the temperature 40 to 80 °C.

Figure 42 shows the Nyquist plot exemplary for the extruded electrolyte with screw design A and at a screw speed of 15 rpm as a function of temperature. For $T \ll T_m$ the Nyquist plot exhibit a visible high-frequency semicircle and a low-frequency straight line. These Nyquist plots are fitted with an equivalent circuit (Figure 42c)) consisting of a parallel RCPE-element and a CPE-element. The RCPE-element is commonly attributed to the ionic resistance of the polymer electrolyte and the capacitive properties of the electrolyte bulk, respectively. The CPE-element is attributed to the capacitive properties of the ion-blocking Al electrodes. It is visible that the semicircle shifts to higher frequencies, and it becomes smaller until it disappears at higher temperatures. As the temperature increases, the ion mobility increases

due to melting of the polymer. This results to a decrease in the resistance of the polymer and of the semicircle. For high temperatures, where no semicircle is visible, the Nyquist plots are fitted with an equivalent circuit (Figure 42d)) consisting of just a R-element (resistance of the electrolyte) and a CPE-element (capacitive properties of blocking electrode) to properly determine the intersection with the x-axis (Z'/Ω). The σ_{ionic} for all temperatures is then calculated as for E1 from the determined R_{SPE}, using equation 8.1 from chapter 8.2.4.

The σ_{ionic} at 80 °C of the PEO-based electrolytes produced at a screw speed of 15 rpm can be taken from Table 5. The σ_{ionic} are in good agreement with σ_{ionic} from other works proofing the production of functional electrolytes.

Table 5: Calculated σ_{ionic} exemplary for 80 °C of extruded PEO-based electrolytes using independent material addition for all three used screw design at a screw speed of 15 rpm

Screw design	Ionic conductivity σ_{ionic} (80 °C)
A	$5.5 \pm 0.5 \times 10^{-4}$ S cm^{-1}
B	$8.4 \pm 0.2 \times 10^{-4}$ S cm^{-1}
C	$1.3 \pm 0.9 \times 10^{-4}$ S cm^{-1}

Figure 43 shows the Arrhenius plot of extruded PEO-based electrolytes with different screw designs, exemplary for 15 rpm. The plot shows the temperature dependence of the determined σ_{ionic}, which can be divided into two sections (section 1: $T \leq 40$ °C and section 2: 50 °C $\leq T$). Between 40 °C and 50 °C a stepwise decrease of σ_{ionic} is observed for all screw designs. This stepwise decrease indicates a sudden increase in resistance, which is also visible in the shown Nyquist plot in Figure 42b). The increase in resistance is attributed to the crystal growth within the polymer during cooling. This is in good accordance with the determined T_m of the electrolytes with DMA (Figure 41), which is in the range of 43 – 55 °C. In general, the extruded PEO-based electrolyte with screw design B shows the best σ_{ionic}. The lowest σ_{ionic} with the highest deviation is determined for the PEO-based electrolyte over the entire temperature range with screw design C. This finding supports the microscopic images (Figure 39 g)-i)) indicating that LiTFSI is not properly added and dissolved during the extrusion process as well as the high deviation in the measured torque during extrusion (Figure 37a)).

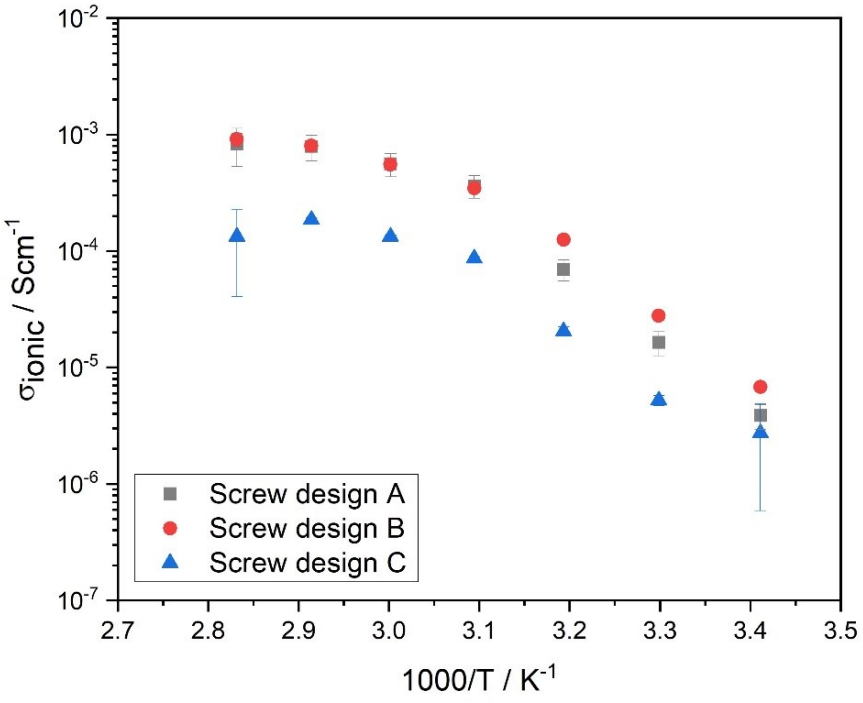

Figure 43: Arrhenius plot of extruded PEO-based electrolytes of E2 with different screw design exemplary for 15 rpm.

In order to have a better overview of how the calculated σ_{ionic} at 80° C fits with σ_{ionic} data from other works, the σ_{ionic} is compared in Figure 44 with the same values from the literature [14,26,121,151,156–160] as the PEO-based electrolyte from E1. As for E1, the determined σ_{ionic} of all produced electrolytes from E2 fits well with the extracted data from literature.

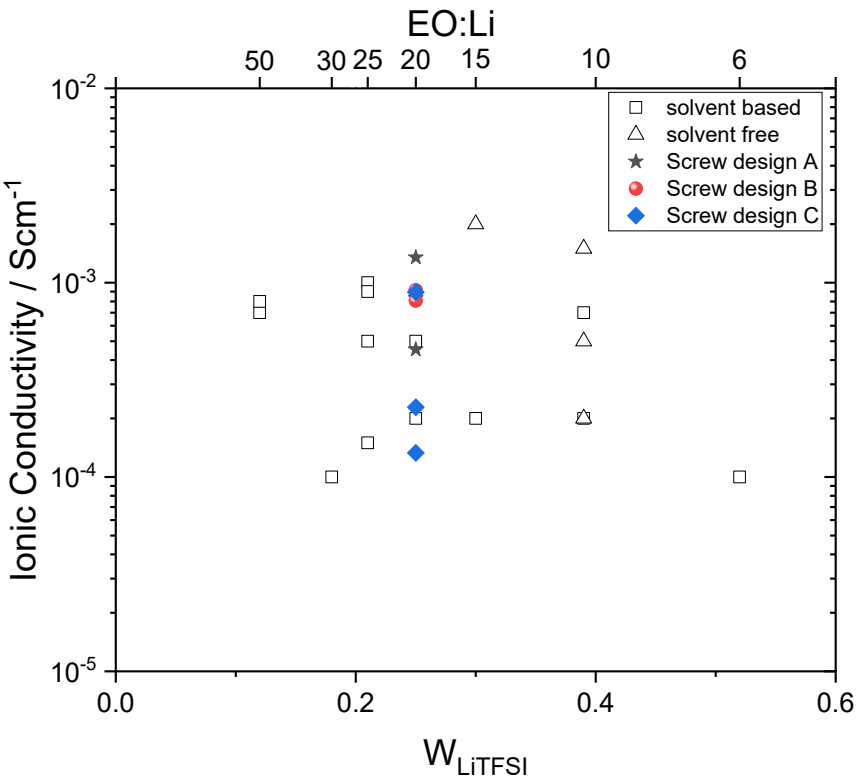

Figure 44: Ionic conductivity (σ_{ionic}) at 80 °C of extruded PEO-based electrolytes of the second extruder setup compared literature values of σ_{ionic} at 80 °C of PEO-based electrolytes produced solvent based (rectangles) [14,151,152,156,159,160] and solvent free (triangles) [26,121,157,158].

To compare the determined σ_{ionic} of the PEO-based electrolytes from the two extruder setups, σ_{ionic} is presented in Figure 45 as a function of M_w for all three screw designs, exemplarily for a screw speed of 15 rpm. From literature it is known that the σ_{ionic} shows a dependence on the M_w, when $M_w < 2{,}000$ g mol^{-1} characterized by an exponential increase of σ_{ionic} [94]. The increase in σ_{ionic} is a result of shorter polymer chains and a higher chain mobility. Despite the observed reduction in M_w for all produced PEO-based electrolytes (s. Figure 33 and Figure 40), the M_w is still high enough that it does not affect the σ_{ionic} of the electrolytes. Nevertheless, a little change in σ_{ionic} is visible comparing the extruder setups and screw designs in the given figure. Since the electrolyte produced in E1 with screw design B (s. Figure 33) has the smallest reduction in M_w of 6 % and by that the smallest effect on σ_{ionic} is expected due to chain scission, it is used as reference for comparison. The electrolytes of E1 produced with screw designs A and C show similar σ_{ionic} at lower M_w. These two electrolytes also show higher reduction in M_w by rheology measurements (s. Figure 33). As shown in Figure 40 the electrolytes of E2 produced with screw design A and B also show reduction in M_w. Different to the electrolytes of E1 they show higher σ_{ionic} than the reference.

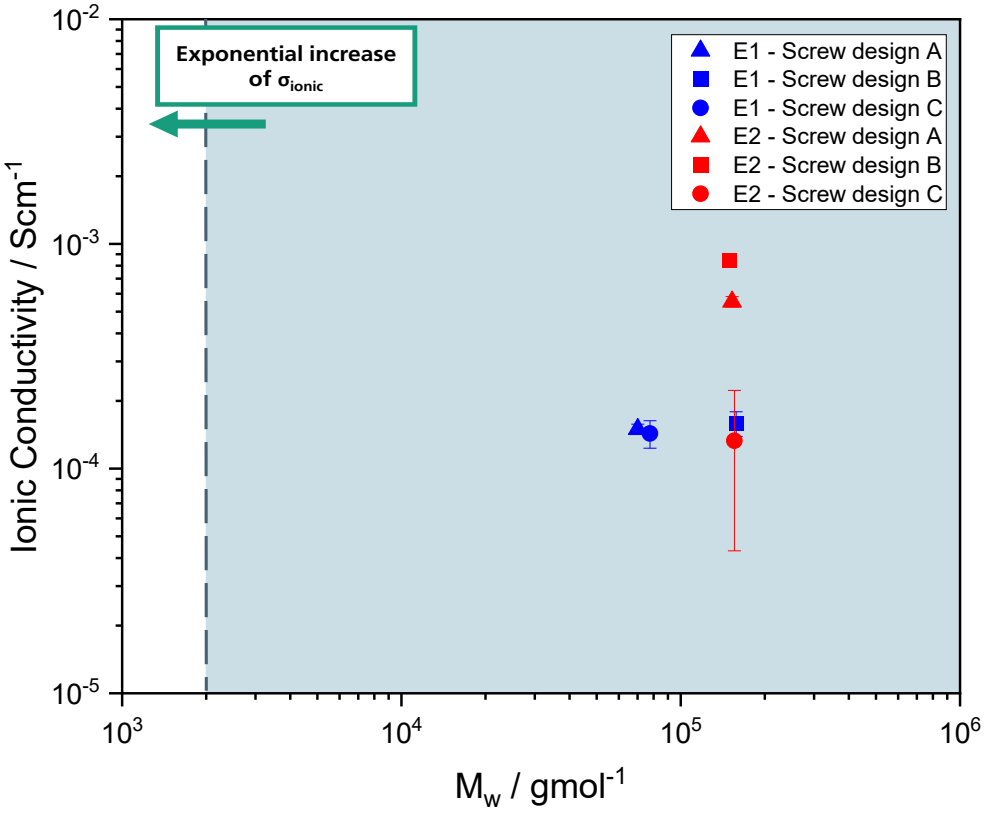

Figure 45: σ_{ionic} at 80 °C of the produced PEO-based electrolytes as a function of its M_w, comparison of σ_{ionic} of the extruded sample with both extruder setups (E1: premixed batch and E2: independent material addition) for each screw design exemplary for 15 rpm. From literature it is known that the σ_{ionic} shows a dependence on the M_w, when $M_w < 2{,}000$ g mol^{-1} characterized by an exponential increase of σ_{ionic} [94]. In the blue area ($M_w > 2{,}000$g mol^{-1}), the σ_{ionic} should be independent of M_w.

It might be important to know how the polymer chains break during extrusion for a better understanding in the resulting σ_{ionic}.

For the PEO-based electrolytes of E1, a uniform chain scission in the middle of the chain would be plausible. This means that larger chain segments of similar length and mobility as in the reference are still present and therefore do not significantly affect the σ_{ionic}. For the PEO-based electrolytes of E2, on the other hand, an irregular chain scission at the beginning or at the end of the polymer chain would be possible. This chain scission would result in many small chain segments and larger chain segments similar to the reference. In contrast to E1, the smaller chain segments would lead to an increase in chain mobility and thus an increase in σ_{ionic}. The possible chain scission is shown in the Figure 46.

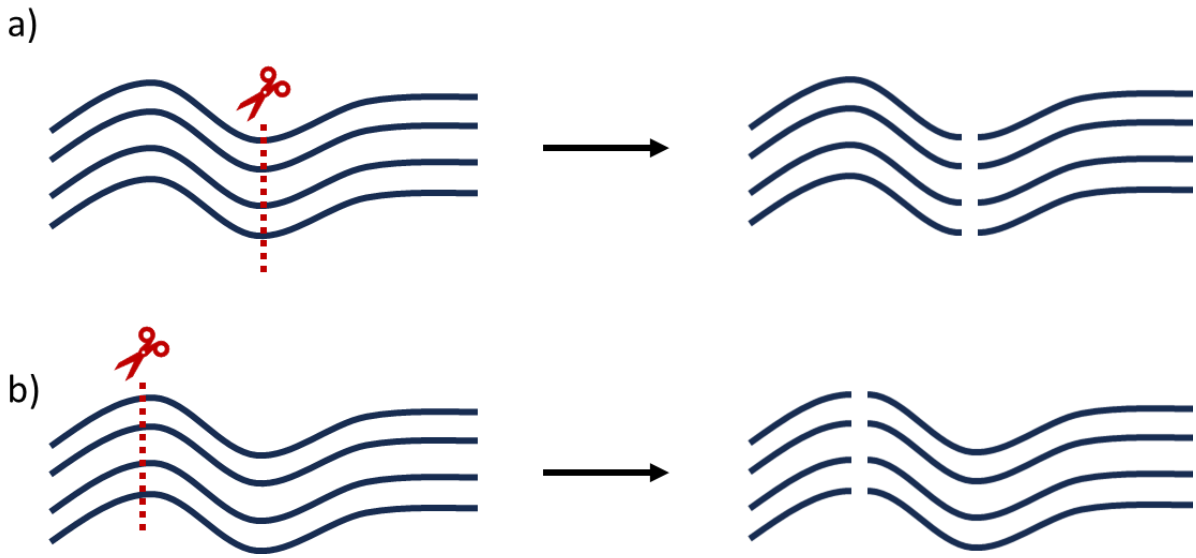

Figure 46: Sketch of possible chain scission of PEO during extrusion; a) chain scission in the middle of the polymer chain resulting in unchanged ionic conductivity; b) chain scission at the beginning or at the end of the polymer chain resulting in an increase of ionic conductivity due to higher chain mobility of smaller chain segments.

Also noticeable in the Figure 45 is the high standard deviation of the σ_{ionic} of the PEO-based electrolyte produced in E2 with screw design C. This could be due to an irregular Li distribution within the produced PEO-based electrolyte string, which was already suspected from the recorded process parameters in chapter 9.1 and microscopy images in Figure 39. In addition to chain scission, the high conductivity of electrolytes produced in E2 may also be caused by a higher Li concentration in the PEO-based electrolyte due to the automated addition of the conductive salt. Due to the complexity of determining the Li concentration, this measurement method was not part of this thesis. However, a suitable measurement method should be evaluated and implemented in future work for a better assessment.

From this comparison, it is not only necessary to determine the absolute M_w, but also the M_w distribution. Therefore, a measurement method must be used to determine the type of chain scission to better understand the relationship between the reduction in M_w during processing and the resulting conductivity of the electrolyte.

All in all, the extrusion process is a suitable processing method to produce PEO-based electrolytes without the use of solvent.

9.3 Conclusion

In this chapter, the two feeders of the extruder were used to add PEO and LiTFSI powders separately and automatically to the extrusion process. Therefore, PEO was added to the extruder first, and then LiTFSI was added directly into the polymer melt from the second feeding unit. The given results show the successful extrusion of PEO-based electrolytes using this experimental setup and a process temperature of 90 °C. Furthermore, the experiments also show both the effect of the extruder setup as well as the effect of the material addition on the process and product quality, so that the following conclusions can be drawn:

- The monitored process parameters, torque, and pressure, show a dependence on the screw design and the applied screw speed. While the torque increases with increasing screw speed, the pressure at the extruder die decreases with the applied screw speed. In general, the measured process parameters are higher than for the first extruder setup, because the overall residence time of both material during the extrusion is shorter. Therefore, the dissolution and the plasticizing effect of LiTFSI occurs later. In addition, the results indicate that the use of kneading and mixing elements is recommended to improve the mixing of PEO and LiTFSI.
- The microscopic observation of the produced PEO-based electrolytes supports the findings from the measured process parameters. The best mixing results are achieved with kneading and mixing elements at high screw speed. Nonetheless, a white pattern along all sample indicates that LiTFSI is not completely dissolved into the polymer matrix.
- The determination of M_w shows a different relationship between process parameter and material stability than seen for E1. The choice of material addition affects the material stability as well as its sensitivity to the screw design used and the screw speed.
- All produced PEO-based electrolytes exhibit an ionic conductivity of $(1.3 \pm 0.9) \times 10^{-4} – (8.4 \pm 0.2) \times 10^{-4}$ S cm^{-1} at 80 °C, which is comparable with the literature indicating successful extrusion of PEO-based solid electrolytes.

Overall, the comparison of the extruder setups shows that the material addition, whether the components are pre-mixed or are added separately to the process, has a major impact on the extrusion process and on the material properties. In addition, the second extruder setup needs to be improved by implementing more kneading or mixing elements to increase the residence

time of the components, thereby increasing the mixing time and improving the dissolution of LiTFSI into the polymer matrix. Nonetheless, this extruder setup gives good perspective for an upscaled and automated dry process of polymer-based electrolytes. And with its independently operating feeders, it also offers the freedom to adjust the composition without much effort.

10. Summary and Outlook

This thesis deals with the scaling of polymer-based solid electrolytes based on PEO. With respect to the various influences of solvent-based manufacturing processes, both at the process and material level, only thermal and thus solvent-free manufacturing processes were considered in this thesis. The aim of this thesis was to investigate the dry and thermal processing of PEO-based SEs using extrusion and to implement a suitable method for this investigation. The experimental matrix developed in this thesis, from the laboratory kneader for the investigation of thermal processing with small sample quantities (g) to the transfer to a twin-screw extruder with larger sample quantities (kg), accompanied by process monitoring and various characterizations to check and determine the process and product quality, respectively, helps to build up a better understanding of the process and to understand the relationship between product quality and process setup.

Kneading experiments

In the first step, kneading experiments were performed to investigate the material behavior during the dry and thermal processing of PEO-based solid electrolytes. Kneading experiments offer the possibility to make first conclusions about the material behavior with smaller sample volumes than required for the extrusion process and to determine suitable process parameters. PEO100k and PEO600k are investigated to determine which molecular weight is more suitable for the dry process. Kneading experiments were conducted at kneading temperatures of 90 and 100 °C and the screw speeds varied from 5 to 20 min^{-1}. The kneading experiments showed that care must be taken in the choice of process parameters for both molecular weights during the thermal processing of PEO. LiTFSI acts as a plasticizer that improves the flowability of PEO. However, despite the improved flowability, GPC measurements showed that for both molecular weights degradation occurs simultaneously with softening of PEO and even intensifies the degradation of long chains of PEO. Although for both molecular weights thermal and mechanical load affect the thermal stability and the kneading behavior of PEO, PEO100k behaves more stable during the kneading time and shows the most homogeneous LiTFSI distribution. The knowledge gained about the material behavior and the choice of parameters was then transferred to the extrusion process.

Extrusion of a pre-mixed PEO_{20}LiTFSI powder batch

In the second step, extrusion experiments of a pre-mixed batch of PEO and LiTFSI with a molar ratio of 20:1 (EO:Li) were examined. A co-rotating twin-screw extruder was used in an Argon filled glovebox. The process temperature of 90 °C was adopted from the kneading experiments. Screw speeds were varied from 5 to 15 rpm. To investigate the effect of screw elements on the mixing behavior of PEO and LiTFSI the screw designs were varied with conveying, kneading and mixing elements. The monitored process parameters, torque and pressure, show a dependence on the screw design and applied screw speeds, i.e. for screw design B the torque shows an increase up to 36 % whereas the pressure shows a reduction of 3 %. Here the most stable process is achieved with kneading elements, i.e. the torque fluctuates only by 2 %. Microscopic observations, i.e. color grading, and the determination of the M_w of the extruded electrolytes (i.e. -6 %) underline the use of kneading elements by showing the best mixing and dissolution of LiTFSI in the polymer matrix, recognizable by digital microscopy and DMA measurements, while maintaining the best polymer properties, i.e. the M_w of 203,000 $gmol^{-1}$ during extrusion. The improvement of this behavior at high screw speeds (15 rpm) offers the possibility of upscaling the process. EIS measurements proved the successful extrusion of functional PEO-based solid electrolytes with an ionic conductivity of (1.1 – 1.8) x 10^{-4} S cm^{-1} at 80 °C.

Extrusion with independent material addition

The third step was to investigate feasibility of adding the PEO and LiTFSI powders separately and automatically to the extrusion process. This not only eliminates an additional process step (pre-mixing of the components) and thus reduces the costs, but also offers the possibility to vary the composition of the extruded polymer electrolytes due to the independently operating feeders. For this extruder setup, PEO was added to the extruder first, and LiTFSI powder was added to the polymer melt second. Here, the implementation of kneading and mixing elements is recommended to improve the mixing of PEO and LiTFSI. These findings are supported by the microscopic observations. Here, the best mixing results are obtained with kneading and mixing elements at high screw speed. The white pattern observed along all samples indicates that LiTFSI was not completely dissolved, so that the residence time is too short. The determination of M_w also show that the choice of material addition affects the material stability as well as its sensitivity to the screw design and the screw speed used. EIS measurements proved successful dry production of functional PEO-based electrolytes using

two independent operating feeders for separate material addition with an ionic conductivity of $(1.3 \pm 0.9) \times 10^{-4} – (8.4 \pm 0.2) \times 10^{-4}$ S cm^{-1} at 80 °C. The two used extruder setups in this work are then compared to determine how the material addition affects the process and product quality. The monitored process parameters indicate that the residence time of the components plays an important role in the product quality. Since the residence time of PEO and LiTFSI is shorter in the second extruder setup than in the first, LiTFSI has less time to dissolve, and the plasticizing effect occurs later.

All in all, this thesis shows the upscaling potential of polymer-based SEs using PEO and LiTFSI as precursors. Dry processing of polymer-based SEs not only offers new processing methods, such as extrusion, to be implemented in battery manufacturing, but also offers the opportunity to produce battery components more sustainably and on a larger scale by eliminating the need for solvents as in conventional slurry processes. Eliminating solvents from the process not only saves material costs, but also production costs such as premixing and drying in long drying ovens. However, the work also highlights the sensitive material behavior during dry processing. It is therefore particularly important to maintain material properties during the scaling of the extrusion process, which corresponds to higher screw speeds and thus higher shear forces into the material. Nevertheless, the extrusion process and the test matrix developed in this thesis can be applied to other material systems such as electrodes of conventional LIBs and composite cathodes for ASSBs. This allows the dry processing by extrusion and the suitability for scaling of these systems to be investigated in a structured and analytical manner.

Outlook

This thesis shows not only the importance of the choice of material and process parameters for thermal stability during processing, but also the impact of the addition of the conductive salt on the processability.

However, optimized production of separators requires mixing as well as shaping. Therefore, both further investigation of direct mixing by using two feeders and the direct shaping of the electrolyte material into foil form for application as separator are necessary. For production of separator foils and a better sample handling during extrusion the current extruder setup needs to be optimized. It is also recommended to add further analytic measurements for a better description of the relationship between process and product.

Further characterization methods should be added to the test matrix are needed to evaluate the direct mixing process and product quality. To evaluate the automatic material dosing employing two feeders, a suitable method needs to be found to determine the real amount of Li-salt in the electrolyte. To support the evaluation of mixing, qualitative and quantitative analytical measurements, such as FTIR spectroscopy, are recommend for investigating the dissociation of Li-salt. Last, the electrochemical performance of the produced separators needs to be tested in cycling tests in full cells. Since the so far produced electrolytes show low mechanical strength, it is recommended to optimize the mechanical properties of the electrolyte prior to cycling.

When looking towards the entire separator production chain, extrusion offers the possibility to combine mixing and shaping. Therefore, as next steps, not only the mixing but also the following steps should be looked at. A conveying belt should be added to the extruder setup for a controlled sample extraction and cooling. The conveyer belt also makes it possible to use another die for shaping such as a slot die for sheet production. Therefore, the slot die must be designed according to the melt viscosity of the separator at the die to ensure uniform shaping and prevent melt breakage. For the production of a higher output and a better handling for post-processing a winding machine is helpful, which can be implemented at the end of the conveyer belt.

References

1. United Nations, Department of Economic and Social Affairs, Population Division. World Population Prospects: The 2017 Revision, Key Findings and Advance Tables. Available online: https://population.un.org/wpp/publications/files/wpp2017_keyfindings.pdf (accessed on 8 January 2024).

2. Moodley, P.; Trois, C. Lignocellulosic biorefineries: the path forward. In *Sustainable Biofuels*: *Opportunities and Challenges*; Ramesh C. Ray, Ed.; Elsevier, 2021; pp 21–42, ISBN 9780128202975.

3. Wille-Haussmann, B.; Biener, W.; Brandes, J.; Jülch, V.; Wittwer, C. Kurzstudie: Batteriespeicher an ehemaligen Kraftwerksstandorten. Positionspapier. Available online: https://www.ise.fraunhofer.de/content/dam/ise/de/documents/publications/studies/Fraunhofer-ISE-Batteriespeicher-an-ehemaligen-Kraftwerkstandorten.pdf (accessed on 8 January 2024).

4. Schmaltz, T.; Wicke, T.; Weymann, L.; Voß, P.; Neef, C.; Thielmann, A. Solid-State Battery Roadmap 2035+. Available online: https://www.isi.fraunhofer.de/content/dam/isi/dokumente/cct/2022/SSB_Roadmap.pdf (accessed on 8 January 2024).

5. Bundesministerium für Wirtschaft und Klimaschutz. Klimaschutz. Available online: https://www.bmwk.de/Redaktion/DE/Textsammlungen/Industrie/klimaschutz.html#:~:text=Bis%202040%20m%C3%BCssen%20die%20Treibhausgase,Landwirtschaft%20und%20Abfall)%20wurden%20versch%C3%A4rft. (accessed on 29 October 2023).

6. Horstmann, W.; Breyer, A. Richtlinie zu einer gemeinsamen Förderinitiative zur Förderung von Forschung und Entwicklung im Bereich der Elektromobilität. Available online: https://www.bmwk.de/Redaktion/DE/Downloads/F/foerderrichtlinie-elektromobilitaet.pdf?__blob=publicationFile&v=1 (accessed on 29 October 2023).

7. Bundesministerium für Wirtschaft und Klimaschutz. Schlaglichter der Witschaftspolitik: Mehr E-Autos für den Klimaschutz. Available online: https://www.bmwk.de/Redaktion/DE/Infografiken/Schlaglichter/2022/02/13-mehr-e-autos.pdf?__blob=publicationFile&v=1 (accessed on 29 October 2023).

8. Bundesministerium für Wirtschaft und Klimaschutz. Batterien für die Mobilität von morgen. Available online: https://www.bmwk.de/Redaktion/DE/Artikel/Industrie/batteriezellfertigung.html (accessed on 29 October 2023).

9. Bundesministerium für Wirtschaft und Klimaschutz. Batterieprojekt von Northvolt in Deutschland macht wichtige Fortschritte – Bundesregierung und Landesregierung planen Unterstützung von Gigafabrik in Heide. Available online: https://www.bmwk.de/Redaktion/DE/Pressemitteilungen/2023/05/20230512-batterieprojekt-von-northvolt-in-deutschland.html (accessed on 29 October 2023).

10. Janek, J.; Zeier, W.G. A solid future for battery development. *Nat Energy* **2016**, *1*, doi:10.1038/nenergy.2016.141.

11. Arya, A.; Sharma, A.L. Polymer electrolytes for lithium ion batteries: a critical study. *Ionics* **2017**, *23*, 497–540, doi:10.1007/s11581-016-1908-6.

12. Mauger, A.; Armand, M.; Julien, C.M.; Zaghib, K. Challenges and issues facing lithium metal for solid-state rechargeable batteries. *Journal of Power Sources* **2017**, *353*, 333–342, doi:10.1016/j.jpowsour.2017.04.018.

13. Wu, Y.; Wang, S.; Li, H.; Chen, L.; Wu, F. Progress in thermal stability of all-solid-state-Li-ion-batteries. *InfoMat* **2021**, *3*, 827–853, doi:10.1002/inf2.12224.

14. Yue, L.; Ma, J.; Zhang, J.; Zhao, J.; Dong, S.; Liu, Z.; Cui, G.; Chen, L. All solid-state polymer electrolytes for high-performance lithium ion batteries. *Energy Storage Materials* **2016**, *5*, 139–164, doi:10.1016/j.ensm.2016.07.003.

15. Placke, T.; Kloepsch, R.; Dühnen, S.; Winter, M. Lithium ion, lithium metal, and alternative rechargeable battery technologies: the odyssey for high energy density. *Journal of Solid State Electrochem* **2017**, 1939–1964, doi:10.1007/s10008-017-3610-7.

16. Schnell, J.; Günther, T.; Knoche, T.; Vieider, C.; Köhler, L.; Just, A.; Keller, M.; Passerini, S.; Reinhart, G. All-solid-state lithium-ion and lithium metal batteries – paving the way to large-scale production. *Journal of Power Sources* **2018**, *382*, 160–175, doi:10.1016/j.jpowsour.2018.02.062.

17. Yang, J.; Wang, X.; Zhang, G.; Ma, A.; Chen, W.; Le Shao; Shen, C.; Xie, K. High-Performance Solid Composite Polymer Electrolyte for all Solid-State Lithium Battery Through Facile Microstructure Regulation. *frontiers in chemistry* **2019**, *7*, 388, doi:10.3389/fchem.2019.00388.

18. Jinisha, B.; Anilkumar, K.M.; Manoj, M.; Pradeep, V.S.; Jayalekshmi, S. Development of a novel type of solid polymer electrolyte for solid state lithium battery applications based on lithium enriched poly (ethylene oxide) (PEO)/poly (vinyl pyrrolidone) (PVP) blend polymer. *Electrochimica Acta* **2017**, *235*, 210–222, doi:10.1016/j.electacta.2017.03.118.

19. Chen, F.; Yang, D.; Zha, W.; Zhu, B.; Zhang, Y.; Li, J.; Gu, Y.; Shen, Q.; Zhang, L.; Sadoway, D.R. Solid polymer electrolytes incorporating cubic Li7La3Zr2O12 for all-solid-state lithium rechargeable batteries. *Electrochimica Acta* **2017**, *258*, 1106–1114, doi:10.1016/j.electacta.2017.11.164.

20. Kimura, K.; Yajima, M.; Tominaga, Y. A highly-concentrated poly(ethylene carbonate)-based electrolyte for all-solid-state Li battery working at room temperature. *Electrochemistry Communications* **2016**, *66*, 46–48, doi:10.1016/j.elecom.2016.02.022.

21. Polu, A.R.; Rhee, H.-W.; Kim, D.K. New solid polymer electrolytes (PEO20–LiTDI–SN) for lithium batteries: structural, thermal and ionic conductivity studies. *J Mater Sci: Mater Electron* **2015**, *26*, 8548–8554, doi:10.1007/s10854-015-3527-9.

22. Zhang, X.; Wang, S.; Xue, C.; Xin, C.; Lin, Y.; Shen, Y.; Li, L.; Nan, C.-W. Self-Suppression of Lithium Dendrite in All-Solid-State Lithium Metal Batteries with Poly(vinylidene difluoride)-Based Solid Electrolytes. *Adv. Mater.* **2019**, *31*, e1806082, doi:10.1002/adma.201806082.

23. Miao, R.; Liu, B.; Zhu, Z.; Liu, Y.; Li, J.; Wang, X.; Li, Q. PVDF-HFP-based porous polymer electrolyte membranes for lithium-ion batteries. *Journal of Power Sources* **2008**, *184*, 420–426, doi:10.1016/j.jpowsour.2008.03.045.

24. Foran, G.; Mankovsky, D.; Verdier, N.; Lepage, D.; Prébé, A.; Aymé-Perrot, D.; Dollé, M. The Impact of Absorbed Solvent on the Performance of Solid Polymer Electrolytes for Use in Solid-State Lithium Batteries. *iScience* **2020**, *23*, 101597, doi:10.1016/j.isci.2020.101597.

25. Appetecchi, G.B.; Hassoun, J.; Scrosati, B.; Croce, F.; Cassel, F.; Salomon, M. Hot-pressed, solvent-free, nanocomposite, PEO-based electrolyte membranes. *Journal of Power Sources* **2003**, *124*, 246–253, doi:10.1016/S0378-7753(03)00611-6.

26. F. M. Gray, J. R. MacCallum and C. A. Vincent. Poly(ethylene oxide)-LiCF3SO3-polystyrene electrolyte systems. *Solid State Ionics* **1986**, 282–286, doi:10.1016/0167-2738(86)90127-X.

27. Wang, L.; Li, X.; Yang, W. Enhancement of electrochemical properties of hot-pressed poly(ethylene oxide)-based nanocomposite polymer electrolyte films for all-solid-state lithium polymer batteries. *Electrochimica Acta* **2010**, *55*, 1895–1899, doi:10.1016/j.electacta.2009.11.003.

28. Mejía, A.; Devaraj, S.; Guzmán, J.; Del Lopez Amo, J.M.; García, N.; Rojo, T.; Armand, M.; Tiemblo, P. Scalable plasticized polymer electrolytes reinforced with surface-modified sepiolite fillers – A feasibility study in lithium metal polymer batteries. *Journal of Power Sources* **2016**, *306*, 772–778, doi:10.1016/j.jpowsour.2015.12.099.

29. Helmers, L.; Froböse, L.; Friedrich, K.; Steffens, M.; Kern, D.; Michalowski, P.; Kwade, A. Sustainable Solvent-Free Production and Resulting Performance of Polymer Electrolyte-Based All-Solid-State Battery Electrodes. *Energy Technol.* **2021**, *9*, 2000923, doi:10.1002/ente.202000923.

30. Froboese, L.; Groffmann, L.; Monsees, F.; Helmers, L.; Loellhoeffel, T.; Kwade, A. Enhancing the Lithium Ion Conductivity of an All Solid-State Electrolyte via Dry and Solvent-Free Scalable Series Production Processes. *J. Electrochem. Soc.* **2020**, *167*, 20558, doi:10.1149/1945-7111/ab6f77.

31. Edman, L.; Ferry, A.; Doeff, M.M. Slow recrystallization in the polymer electrolyte system poly(ethylene oxide)n–LiN(CF3SO2)2. *J. Mater. Res.* **2000**, 1950–1954, doi:10.1557/JMR.2000.0281.

32. Marzantowicz, M.; Dygas, J.R.; Krok, F.; Nowiński, J.L.; Tomaszewska, A.; Florjańczyk, Z.; Zygadło-Monikowska, E. Crystalline phases, morphology and conductivity of PEO:LiTFSI electrolytes in the eutectic region: Bearbeitet. *Journal of Power Sources* **2006**, *159*, 420–430, doi:10.1016/j.jpowsour.2006.02.044.

33. Zhang, H.; Liu, C.; Zheng, L.; Xu, F.; Feng, W.; Li, H.; Huang, X.; Armand, M.; Nie, J.; Zhou, Z. Lithium bis(fluorosulfonyl)imide/poly(ethylene oxide) polymer electrolyte. *Electrochimica Acta* **2014**, *133*, 529–538, doi:10.1016/j.electacta.2014.04.099.

34. Nair, J.R.; Imholt, L.; Brunklaus, G.; Winter, M. Lithium Metal Polymer Electrolyte Batteries: Opportunities and Challenges. *The Electrochemical Society Interface* **2019**, 55–61, doi:10.1149/2.F05192if.

35. Crowley, M.M. *Physiochemical and Mechanical Characterization of Hot-Melt Extruded Dosage Forms*. PhD Dissertation; The University of Texas at Austin, Austin, TX, USA, 2003.

36. Crowley, M.M.; Zhang, F.; Koleng, J.J.; McGinity, J.W. Stability of polyethylene oxide in matrix tablets prepared by hot-melt extrusion. *Biomaterials* **2002**, *23*, 4241–4248, doi:10.1016/S0142-9612(02)00187-4.

37. Fenton, D.E.; Parker, J.M.; Wright, P.V. Complexes of alkali metal ions with poly(ethylene oxide). *Polymer* **1973**, *14*, 589, doi:10.1016/0032-3861(73)90146-8.

38. Marzantowicz, M.; Dygas, J.R.; Krok, F.; Nowiński, J.L.; Tomaszewska, A.; Florjańczyk, Z.; Zygadło-Monikowska, E. Crystalline phases, morphology and conductivity of PEO:LiTFSI electrolytes in the eutectic region. *Journal of Power Sources* **2006**, *159*, 420–430, doi:10.1016/j.jpowsour.2006.02.044.

39. APB Corporation. All Polymer Battery. Available online: https://apb.co.jp/en/all_polymer_battery/ (accessed on 11 January 2024).

40. APB Corporation. Factory: The next-gen power module factory proposed by APB. Available online: https://apb.co.jp/en/factory/ (accessed on 11 January 2024).

41. BlueSolutions, Bolloré. *Make a solid choice*: *We are the world leader in solid-state batteries, better we mass produce them.*, 2021. Available online: https://www.blue-solutions.com/app/assets-bluesolutions/uploads/2021/04/0414_bsol_2102265_brochure_16_pages_gb.pdf (accessed on 25 September 2023).

42. Deschamps, M. Lithium Metal Polymer battery: its specifities and its application. Nice, France, October 2, 2018.

43. Reddy, M.V.; Mauger, A.; Julien, C.M.; Paolella, A.; Zaghib, K. Brief History of Early Lithium-Battery Development. *Materials (Basel)* **2020**, *13*, doi:10.3390/ma13081884.

44. *Handbuch Lithium-Ionen-Batterien;* Korthauer, R., Ed.; Springer Vieweg: Berlin Heidelberg, 2013, ISBN ISBN 978-3-642-30652-5.

45. Py, M.A.; Haering, R.R. Structural destabilization induced by lithium intercalation in MoS 2 and related compounds. *Can. J. Phys.* **1983**, *61*, 76–84, doi:10.1139/p83-013.

46. Goodenough, J.B.; Mizushima, K.; Wiseman, P.J. Electrochemical cell and method of making ion conductors for said cell (0 017 400 B1).

47. Janek, J.; Zeier, W.G. Challenges in speeding up solid-state battery development. *Nat Energy* **2023**, 230–240, doi:10.1038/s41560-023-01208-9.

48. Chen, Y.; Kang, Y.; Zhao, Y.; Wang, L.; Liu, J.; Li, Y.; Liang, Z.; He, X.; Li, X.; Tavajohi, N.; et al. A review of lithium-ion battery safety concerns: The issues, strategies, and testing standards. *Journal of Energy Chemistry* **2021**, *59*, 83–99, doi:10.1016/j.jechem.2020.10.017.

49. Nitta, N.; Wu, F.; Lee, J.T.; Yushin, G. Li-ion battery materials: present and future. *Materials Today* **2015**, *18*, 252–264, doi:10.1016/j.mattod.2014.10.040.

50. Ezhyeh, Z.N.; Khodaei, M.; Torabi, F. Review on doping strategy in Li4Ti5O12 as an anode material for Lithium-ion batteries. *Ceramics International* **2023**, *49*, 7105–7141, doi:10.1016/j.ceramint.2022.04.340.

51. Laheäär, A.; Kurig, H.; Jänes, A.; Lust, E. LiPF6 based ethylene carbonate–dimethyl carbonate electrolyte for high power density electrical double layer capacitor. *Electrochimica Acta* **2009**, *54*, 4587–4594, doi:10.1016/j.electacta.2009.03.059.

52. Li, Q.; Chen, J.; Fan, L.; Kong, X.; Lu, Y. Progress in electrolytes for rechargeable Li-based batteries and beyond. *Green Energy & Environment* **2016**, *1*, 18–42, doi:10.1016/j.gee.2016.04.006.

53. Xu, K. Nonaqueous Liquid Electrolytes for Lithium-Based Rechargeable Batteries. *ChemInform* **2004**, *35*, doi:10.1002/chin.200450271.

54. Kim, K.; Park, I.; Ha, S.-Y.; Kim, Y.; Woo, M.-H.; Jeong, M.-H.; Shin, W.C.; Ue, M.; Hong, S.Y.; Choi, N.-S. Understanding the thermal instability of fluoroethylene carbonate in LiPF 6 -based electrolytes for lithium ion batteries. *Electrochimica Acta* **2017**, *225*, 358–368, doi:10.1016/j.electacta.2016.12.126.

55. Åvall, G.; Wallenstein, J.; Cheng, G.; Gering, K.L.; Johansson, P.; Abraham, D.P. Highly Concentrated Electrolytes: Electrochemical and Physicochemical Characteristics of LiPF 6 in Propylene Carbonate Solutions. *J. Electrochem. Soc.* **2021**, *168*, 50521, doi:10.1149/1945-7111/abfdc3.

56. Lebedeva, N.P.; Boon-Brett, L. Considerations on the Chemical Toxicity of Contemporary Li-Ion Battery Electrolytes and Their Components. *J. Electrochem. Soc.* **2016**, *163*, A821-A830, doi:10.1149/2.0171606jes.

57. LEI, T.; YANG, Z.; LIN, Z.; ZHANG, X. State of art on energy management strategy for hybrid-powered unmanned aerial vehicle. *Chinese Journal of Aeronautics* **2019**, *32*, 1488–1503, doi:10.1016/j.cja.2019.03.013.

58. Xia, Y.; Fujieda, T.; Tatsumi, K.; Prosini, P.P.; Sakai, T. Thermal and electrochemical stability of cathode materials in solid polymer electrolyte. *Journal of Power Sources* **2001**, *92*, 234–243, doi:10.1016/S0378-7753(00)00533-4.

59. Nie, K.; Wang, X.; Qiu, J.; Wang, Y.; Yang, Q.; Xu, J.; Yu, X.; Li, H.; Huang, X.; Chen, L. Increasing Poly(ethylene oxide) Stability to 4.5 V by Surface Coating of the Cathode. *ACS Energy Lett.* **2020**, *5*, 826–832, doi:10.1021/acsenergylett.9b02739.

60. Kaihui Nie, Yanshuai Hong, Jiliang Qiu, Qinghao Li, Xiqian Yu, Hong Li and Liquan Chen. Interfaces Between Cathode and Electrolyte in Solid State Lithium Batteries: Challenges and Perspectives. *frontiers in chemistry* **2018**, doi:10.3389/fchem.2018.00616.

61. Goodenough, J.B.; Kim, Y. Challenges for Rechargeable Li Batteries. *Chemistry of Materials* **2010**, 587–603, doi:10.1021/cm901452z.

62. Kerman, K.; Luntz, A.; Viswanathan, V.; Chiang, Y.-M.; Chen, Z. Review—Practical Challenges Hindering the Development of Solid State Li Ion Batteries. *J. Electrochem. Soc.* **2017**, *164*, A1731-A1744, doi:10.1149/2.1571707jes.

63. Varzi, A.; Raccichini, R.; Passerini, S.; Scrosati, B. Challenges and prospects of the role of solid electrolytes in the revitalization of lithium metal batteries. *J. Mater. Chem. A* **2016**, *4*, 17251–17259, doi:10.1039/C6TA07384K.

64. Ren, Y.; Chen, K.; Chen, R.; Liu, T.; Zhang, Y.; Nan, C.-W. Oxide Electrolytes for Lithium Batteries. *J. Am. Ceram. Soc.* **2015**, *98*, 3603–3623, doi:10.1111/jace.13844.

65. Lau, J.; DeBlock, R.H.; Butts, D.M.; Ashby, D.S.; Choi, C.S.; Dunn, B.S. Sulfide Solid Electrolytes for Lithium Battery Applications. *Adv. Energy Mater.* **2018**, *8*, 1800933, doi:10.1002/aenm.201800933.

66. Yoshio, M.; Brodd, R.J.; Kozawa, A. *Lithium-Ion Batteries;* Springer New York: New York, NY, 2009, ISBN 978-0-387-34444-7.

67. Agrawal, R.C.; Pandey, G.P. Solid polymer electrolytes: materials designing and all-solid-state battery applications: an overview. *J. Phys. D: Appl. Phys.* **2008**, *41*, 223001, doi:10.1088/0022-3727/41/22/223001.

68. Watanabe, M.; Nagaoka, K.; Kanba, M.; Shinohara, I. Ionic Conductivity of Polymeric Solid Electrolytes Based on Poly(propylene oxide) or Poly(tetramethylene oxide). *Polym J* **1982**, *14*, 877–886, doi:10.1295/polymj.14.877.

69. Armand, M.B.; Bruce, P.G.; Forsyth, M.; Scrosati, B.; Wieczorek, W. Polymer Electrolytes. In *Energy Materials*; Bruce, D.W., O'Hare, D., Walton, R.I., Eds.; Wiley, 2011; pp 1–31, ISBN 9780470997529.

70. Ito, Y.; Kanehori, K.; Miyauchi, K.; Kudo, T. Ionic conductivity of electrolytes formed from PEO-LiCF3SO3 complex low molecular weight poly(ethylene glycol). *J Mater Sci* **1987**, *22*, 1845–1849, doi:10.1007/BF01132415.

71. Sabrina, Q.; Sohib, A.; Lestariningsih, T.; Nuryadin, B.W. Polyethylene glycol incorporation on doctor blade and screen printing cast solid polymer electrolyte based PVDF HFP– LiBOB. *IOP Conf. Ser.: Mater. Sci. Eng.* **2019**, *509*, 12114, doi:10.1088/1757-899X/509/1/012114.

72. Zewde, B.W.; Carbone, L.; Greenbaum, S.; Hassoun, J. A novel polymer electrolyte membrane for application in solid state lithium metal battery. *Solid State Ionics* **2018**, *317*, 97–102, doi:10.1016/j.ssi.2017.12.039.

73. Pignanelli, F.; Romero, M.; Faccio, R.; Mombrú, Á.W. Short- and long-range structure correlations with ionic transport near the glass transition for lithium-ion polyacrylonitrile-based electrolytes using DMSO plasticizer. *Journal of Non-Crystalline Solids* **2021**, *561*, 120744, doi:10.1016/j.jnoncrysol.2021.120744.

74. Li, W.; Pang, Y.; Liu, J.; Liu, G.; Wang, Y.; Xia, Y. A PEO-based gel polymer electrolyte for lithium ion batteries. *RSC Adv.* **2017**, *7*, 23494–23501, doi:10.1039/C7RA02603J.

75. Chen, P.; Liang, X.; Wang, J.; Di Zhang; Yang, S.; Wu, W.; Zhang, W.; Fan, X.; Zhang, D. PEO/PVDF-based gel polymer electrolyte by incorporating nano-TiO2 for electrochromic glass. *J Sol-Gel Sci Technol* **2017**, *81*, 850–858, doi:10.1007/s10971-016-4235-5.

76. Jie, J.; Liu, Y.; Cong, L.; Zhang, B.; Lu, W.; Zhang, X.; Liu, J.; Xie, H.; Sun, L. High-performance PVDF-HFP based gel polymer electrolyte with a safe solvent in Li metal polymer battery. *Journal of Energy Chemistry* **2020**, *49*, 80–88, doi:10.1016/j.jechem.2020.01.019.

77. Periasamy, P.; Tatsumi, K.; Shikano, M.; Fujieda, T.; Saito, Y.; Sakai, T.; Mizuhata, M.; Kajinami, A.; Deki, S. Studies on PVdF-based gel polymer electrolytes. *Journal of Power Sources* **2000**, *88*, 269–273, doi:10.1016/S0378-7753(99)00348-1.

78. Tan, L.; Deng, Y.; Cao, Q.; Jing, B.; Wang, X.; Liu, Y. Gel electrolytes based on polyacrylonitrile/thermoplastic polyurethane/polystyrene for lithium-ion batteries. *Ionics* **2019**, *25*, 3673–3682, doi:10.1007/s11581-019-02940-7.

79. Kufian, M.Z.; Aziz, M.F.; Shukur, M.F.; Rahim, A.S.; Ariffin, N.E.; Shuhaimi, N.; Majid, S.R.; Yahya, R.; Arof, A.K. PMMA–LiBOB gel electrolyte for application in lithium ion batteries. *Solid State Ionics* **2012**, *208*, 36–42, doi:10.1016/j.ssi.2011.11.032.

80. Guan, S.; Wang, W.; Zheng, J.; Xu, C. A method to achieve full incorporation of PMMA-based gel electrolyte in fiber-structured PVB for solid-state electrochromic device fabrication. *Electrochimica Acta* **2020**, *354*, 136702, doi:10.1016/j.electacta.2020.136702.

81. Hosseinioun, A.; Paillard, E. In situ crosslinked PMMA gel electrolyte from a low viscosity precursor solution for cost-effective, long lasting and sustainable lithium-ion batteries. *Journal of Membrane Science* **2020**, *594*, 117456, doi:10.1016/j.memsci.2019.117456.

82. Qian, X.; Gu, N.; Cheng, Z.; Yang, X.; Wang, E.; Dong, S. Plasticizer effect on the ionic conductivity of PEO-based polymer electrolyte. *Materials Chemistry and Physics* **2002**, *74*, 98–103, doi:10.1016/S0254-0584(01)00408-4.

83. Angell, C.A.; Xu, K.; Zhang, S.-S.; Videa, M. Variations on the salt-polymer electrolyte theme for flexible solid electrolytes. *Solid State Ionics* **1996**, *86-88*, 17–28, doi:10.1016/0167-2738(96)00088-4.

84. Soo, P.P.; Huang, B.; Jang, Y.-I.; Chiang, Y.-M.; Sadoway, D.R.; Mayes, A.M. Rubbery Block Copolymer Electrolytes for Solid-State Rechargeable Lithium Batteries. *J. Electrochem. Soc.* **1999**, *146*, 32–37, doi:10.1149/1.1391560.

85. Zheng, X. Novel “Rubber” electrolyte will be applied to long-lasting, safer future EV batteries. *Advanced Sensor and Energy Materials* **2022**, *1*, 100002, doi:10.1016/j.asems.2022.100002.

86. Lee, M.J.; Han, J.; Lee, K.; Lee, Y.J.; Kim, B.G.; Jung, K.-N.; Kim, B.J.; Lee, S.W. Elastomeric electrolytes for high-energy solid-state lithium batteries. *Nature* **2022**, *601*, 217–222, doi:10.1038/s41586-021-04209-4.

87. Zhai, H.; Gong, T.; Xu, B.; Cheng, Q.; Paley, D.; Qie, B.; Jin, T.; Fu, Z.; Tan, L.; Lin, Y.-H.; et al. Stabilizing Polyether Electrolyte with a 4 V Metal Oxide Cathode by Nanoscale Interfacial Coating. *ACS Appl. Mater. Interfaces* **2019**, *11*, 28774–28780, doi:10.1021/acsami.9b04932.

88. Yu, J.; Wang, C.; Li, S.; Liu, N.; Zhu, J.; Lu, Z. Li+ -Containing, Continuous Silica Nanofibers for High Li+ Conductivity in Composite Polymer Electrolyte. *Small* **2019**, *15*, e1902729, doi:10.1002/smll.201902729.

89. Arya, A.; Sharma, A.L. Structural, microstructural and electrochemical properties of dispersed-type polymer nanocomposite films. *J. Phys. D: Appl. Phys.* **2018**, *51*, 45504, doi:10.1088/1361-6463/aa9f69.

90. Meng, N.; Zhu, X.; Lian, F. Particles in composite polymer electrolyte for solid-state lithium batteries: A review. *Particuology* **2022**, *60*, 14–36, doi:10.1016/j.partic.2021.04.002.

91. Nagajothi, A.J.; Kannan, R.; Thanikaikarasan, S.; Sebastian, P.J. Electrochemical and Thermal Properties of PEO-LITFSI based Gel Polymer Electrolytes with the Effect of Plasticizer and Filler for Lithium-sulfur Batteries. *J. New Mat. Electrochem. Sys.* **2018**, *21*, 29–32, doi:10.14447/jnmes.v21i1.518.

92. Das, S.; Ghosh, A. Ion conduction and relaxation in PEO-LiTFSI-Al2O3 polymer nanocomposite electrolytes. *Journal of Applied Physics* **2015**, *117*, doi:10.1063/1.4919721.

93. Xue, Z.; He, D.; Xie, X. Poly(ethylene oxide)-based electrolytes for lithium-ion batteries. *J. Mater. Chem. A* **2015**, *3*, 19218–19253, doi:10.1039/C5TA03471J.

94. Hallinan, D.T.; Balsara, N.P. Polymer Electrolytes. *Annu. Rev. Mater. Res.* **2013**, *43*, 503–525, doi:10.1146/annurev-matsci-071312-121705.

95. An, Y.; Han, X.; Liu, Y.; Azhar, A.; Na, J.; Nanjundan, A.K.; Wang, S.; Yu, J.; Yamauchi, Y. Progress in Solid Polymer Electrolytes for Lithium-Ion Batteries and Beyond. *Small* **2022**, doi:10.1002/smll.202103617.

96. Gadjourova, Z.; Andreev, Y.G.; Tunstall, D.P.; Bruce, P.B. Ionic conductivity in crystalline polymer electrolytes. *Nature* **2001**, 520-523, doi:10.1038/35087538.

97. Armand, M.B. Polymer Electrolytes. *Ann. Rev. Mater. Sci.* **1986**, 245–261, doi:10.1146/annurev.ms.16.080186.001333.

98. Golodnitsky, D.; Livshits, E.; Peled, E. Highly conductive oriented PEO-based polymer electrolytes. *Macromol. Symp.* **2003**, 27–45, doi:10.1002/masy.200351303.

99. Borodin, O.; Smith, G.D. Mechanism of Ion Transport in Amorphous Poly(ethylene oxide)/LiTFSI from Molecular Dynamics Simulations. *Macromolecules* **2006**, *39*, 1620–1629, doi:10.1021/ma052277v.

100. Mark, J.E. *Polymer Data Handbook;* Oxford Univ. Press, 1999, ISBN 9780195181012.

101. Ferloni, P.; Chiodell, G.; Magistris, A.; Sanesi, M. Ion transport and thermal properties of poly(ethylene oxide) - LiClO4 Polymer electrolytes. *Solid State Ionics* **1986**, 265–270, doi:10.1016/0167-2738(86)90124-4.

102. Angulakshmi, N.; Nahm, K.S.; Nair, J.R.; Gerbaldi, C.; Bongiovanni, R.; Penazzi, N.; Stephan, A.M. Cycling profile of MgAl2O4-incorporated composite electrolytes composed of PEO and LiPF6 for lithium polymer batteries. *Electrochimica Acta* **2013**, *90*, 179–185, doi:10.1016/j.electacta.2012.12.003.

103. Ibrahim, S.; Yassin, M.M.; Ahmad, R.; Johan, M.R. Effects of various LiPF6 salt concentrations on PEO-based solid polymer electrolytes. *Ionics* **2011**, *17*, 399–405, doi:10.1007/s11581-011-0524-8.

104. Magistris, A.; Mustrarelli, P.; Quartarone, E.; Tomasi, C. Transport and thermal properties of (PEO)n–LiPF6 electrolytes for super-ambient applications. *Solid State Ionics* **2000**, 1241–1247, doi:10.1016/S0167-2738(00)00594-4.

105. Boise, A.C.; Tambelli, C.C.; Franco, R.W.A.; Donoso, J.P.; Magon, C.J.; Souza, M.F.; Rosario, A.V.; Pereira, E.C. Nuclear magnetic resonance study of PEO-based composite polymer electrolytes. *Electrochimica Acta* **2001**, 1571–1579, doi:10.1016/S0013-4686(00)00755-6.

106. Kalita, M.; Bukat, M.; Ciosek, M.; Siekierski, M.; Chung, S.H.; Rodríguez, T.; Greenbaum, S.G.; Kovarsky, R.; Golodnitsky, D.; Peled, E.; et al. Effect of calixpyrrole in PEO–LiBF4 polymer electrolytes. *Electrochimica Acta* **2005**, *50*, 3942–3948, doi:10.1016/j.electacta.2005.02.067.

107. Appetecchi, G.B.; Henderson, W.; Villano, P.; Berrettoni, M.; Passerini, S. PEO-LiN(SO2CF2CF3)2 Polymer Electrolytes I. XRD, DSC, and Ionic Conductivity Characterization. *Journal of the Electrochemical Society*, *2001*, A1171-A1178, doi:10.1149/1.1403728.

108. Appetecchi, G.B.; Shin, J.H.; Alessandrini, F.; Passerini, S. 0.6 Ah Li/V2O5 battery prototypes based on solvent-free PEO–LiN(SO2CF2CF3)2 polymer electrolytes. *Journal of Power Sources* **2005**, 236–242, doi:10.1016/j.jpowsour.2004.11.039.

109. Shin, J.H.; Alessandrini, F.; Passerini, S. Comparison of Solvent-Cast and Hot-Pressed P(EO)20LiN(SO2CF2CF3)2 Polymer Electrolytes Containing Nanosized SiO2. *Journal of the Electrochemical Society* **2005**, A283-A288, doi:10.1149/1.1846713.

110. Villano, P.; Carewska, M.; Appetecchi, G.B.; Passerini, S. PEO-LiN(SO2CF2CF3)2 Polymer Electrolytes III. Test in Batteries. *Journal of the Electrochemical Society* **2002**, A1282-A1285, doi:10.1149/1.1502688.

111. Vallee, A.; Besner, S.; Prud'homme, J. Comparative study of poly(ethylene oxide) electrolytes made with LiN(CF3SO2)2, LiCF3SO3 and LiClO4 : Thermal properties and conductivity behaviour. *Electrochimica Acta*, *1992*, 1579–1583, doi:10.1016/0013-4686(92)80115-3.

112. Gomez, E.D.; Panday, A.; Feng, E.H.; Chen, V.; Stone, G.M.; Minor, A.M.; Kisielowski, C.; Downing, K.H.; Borodin, O.; Smith, G.D.; et al. Effect of ion distribution on conductivity of block copolymer electrolytes. *Nano Lett.* **2009**, *9*, 1212–1216, doi:10.1021/nl900091n.

113. Uno, T.; Kawaguchi, S.; Kubo, M.; Itoh, T. Ionic conductivity and thermal property of solid hybrid polymer electrolyte composed of oligo(ethylene oxide) unit and butyrolactone unit. *Journal of Power Sources* **2008**, 716–722, doi:10.1016/j.jpowsour.2007.11.088.

114. Qiu, Z.; Ikehara, T.; Nishi, T. Miscibility and crystallization in crystalline/crystalline blends of poly(butylene succinate)/poly(ethylene oxide). *Polymer* **2003**, *44*, 2799–2806, doi:10.1016/S0032-3861(03)00149-6.

115. Alloin, F.; Sanchez, J.-Y. New solvating polyether networks. *Electrochimica Acta* **1995**, 2269–2276, doi:10.1016/0013-4686(95)00175-E.

116. Stephan, A.M. Review on gel polymer electrolytes for lithium batteries. *European Polymer Journal* **2006**, 21–42, doi:10.1016/j.eurpolymj.2005.09.017.

117. Polu, A.R.; Rhee, H.-W. Ionic liquid doped PEO-based solid polymer electrolytes for lithium-ion polymer batteries. *International Journal of Hydrogen Energy* **2017**, *42*, 7212–7219, doi:10.1016/j.ijhydene.2016.04.160.

118. Utpalla, P.; Sharma, S.K.; Deshpande, S.K.; Bahadur, J.; Sen, D.; Sahu, M.; Pujari, P.K. Role of free volumes and segmental dynamics on ion conductivity of PEO/LiTFSI solid polymer electrolytes filled with SiO2 nanoparticles: a positron annihilation and broadband dielectric spectroscopy study. *Phys. Chem. Chem. Phys.* **2021**, *23*, 8585–8597, doi:10.1039/d1cp00194a.

119. Appetecchi, G.B.; Croce, F.; Hassoun, J.; Scrosati, B.; Salomon, M.; Cassel, F. Hot-pressed, dry, composite, PEO-based electrolyte membranes I. Ionic conductivity characterization. *Journal of Power Sources* **2003**, 105–112, doi:10.1016/S0378-7753(02)00543-8.

120. Golodnitsky, D. Ion-transport phenomena in concentrated PEO-based composite polymer electrolytes. *Solid State Ionics* **2002**, *147*, 141–155, doi:10.1016/S0167-2738(01)01036-0.

121. Kim, Y.-T.; Smotkin, E.S. The effect of plasticizers on transport and electrochemical properties of PEO-based electrolytes for lithium rechargeable batteries. *Solid State Ionics* **2002**, *149*, 29–37, doi:10.1016/S0167-2738(02)00130-3.

122. Xie, J.; Duan, R.G.; Han, Y.; Kerra, J.B. Morphological, Rheological and Electrochemical Studies of Poly(Ethylene Oxide) Electrolytes Containing Fumed Silica Nanoparticles. *Solid State Ionics* **2004**, 755–758, doi:10.1016/j.ssi.2003.10.021.

123. Heimes, H.H.; Kampker, A.; Wennemar, S.; Scheibe, A.; Plumeyer, J.F.; Michaelis, S.; Schütrumpf, J. Produktion einer All-solid-state-Batteriezelle. *PEM der RWTH Aachen & VDMA* **2023**.

124. Duffner, F.; Kronemeyer, N.; Tübke, J.; Leker, J.; Winter, M.; Schmuch, R. Post-lithium-ion battery cell production and its compatibility with lithium-ion cell production infrastructure. *Nat Energy* **2021**, *6*, 123–134, doi:10.1038/s41560-020-00748-8.

125. Duffner, F.; Mauler, L.; Wentker, M.; Leker, J.; Winter, M. Large-scale automotive battery cell manufacturing: Analyzing strategic and operational effects on manufacturing costs. *International Journal of Production Economics* **2021**, doi:10.1016/j.ijpe.2020.107982.

126. JunJung, Y.S.; Oh, D.Y.; Nam, Y.J.; Park, K.H. Issues and Challenges for Bulk-Type All-Solid-State Rechargeable Lithium Batteries using Sulfide Solid Electrolytes. *Isr. J. Chem.* **2015**, *55*, 472–485, doi:10.1002/ijch.201400112.

127. Hayashi, A.; Muramatsu, H.; Ohtomo, T.; Hama, S.; Tatsumisago, M. Improvement of chemical stability of Li3PS4 glass electrolytes by adding MxOy (M ¼ Fe, Zn, and Bi) nanoparticles. *Journal of Materials Chemistry A* **2013**, 6320–6326, doi:10.1039/C3TA10247E.

128. Muramatsu, H.; Hayashi, A.; Ohtomo, T.; Hama, S.; Tatsumisago, M. Structural change of Li2S–P2S5 sulfide solid electrolytes in the atmosphere. *Solid State Ionics* **2011**, 116–119, doi:10.1016/j.ssi.2010.10.013.

129. Lu, X.; Camara, O.; Liu, Z.; Windmüller, A.; Tsai, C.-L.; Tempel, H.; Yu, S.; Kungl, H.; Eichel, R.-A. Tuning the moisture stability of multiphase β-Li3PS4 solid electrolyte materials. *Electrochemical Science Advances* **2022**, doi:10.1002/elsa.202100208.

130. Ohtomo, T.; Hayashi, A.; Tatsumisago, M.; Kawamoto, K. Suppression of H2S gas generation from the 75Li2S*25P2S5 glass electrolyte by additives. *J. Mater. Sci.* **2013**, 4137–4142, doi:10.1007/s10853-013-7226-8.

131. Schnell, J.; Tietz, F.; Singer, C.; Hofer, A.; Billot, N.; Reinhart, G. Prospects of production technologies and manufacturing costs of oxide-based all-solid-state lithium batteries. *Energy Environ. Sci.* **2019**, *12*, 1818–1833, doi:10.1039/C8EE02692K.

132. Miara, L.; Windmüller, A.; Tsai, C.-L.; Richards, W.D.; Ma, Q.; Uhlenbruck, S.; Guillon, O.; Ceder, G. About the Compatibility between High Voltage Spinel Cathode Materials and Solid Oxide Electrolytes as a Function of Temperature. *ACS Appl. Mater. Interfaces* **2016**, *8*, 26842–26850, doi:10.1021/acsami.6b09059.

133. Kwade, A.; Haselrieder, W.; Leithoff, R.; Modlinger, A.; Dietrich, F.; Droeder, K. Current status and challenges for automotive battery production technologies: Bearbeitet. *Nat Energy* **2018**, *3*, 290–300, doi:10.1038/s41560-018-0130-3.

134. Liu, Y.; Zhang, R.; Wang, J.; Wang, Y. Current and future lithium-ion battery manufacturing. *iScience* **2021**, *24*, 102332, doi:10.1016/j.isci.2021.102332.

135. Appetecchi, G.B.; Carewska, M.; Alessandrini, F.; Prosini, P.P.; Passerini, S. Characterization of PEO-Based Composite Cathodes. I. Morphological, Thermal, Mechanical, and Electrical Properties. *J. Electrochem. Soc.* **2000**, *147*, 451, doi:10.1149/1.1393217.

136. Haarmann, M.; Grießl, D.; Kwade, A. Continuous Processing of Cathode Slurry by Extrusion for Lithium-Ion Batteries. *Energy Technol.* **2021**, *9*, doi:10.1002/ente.202100250.

137. Seeba, J.; Reuber, S.; Heubner, C.; Müller-Köhn, A.; Wolter, M.; Michaelis, A. Extrusion-based fabrication of electrodes for high-energy Li-ion batteries. *Chemical Engineering Journal* **2020**, *402*, 125551, doi:10.1016/j.cej.2020.125551.

138. Haarmann, M.; Haselrieder, W.; Kwade, A. Extrusion-Based Processing of Cathodes: Influence of Solid Content on Suspension and Electrode Properties: Bearbeitet. *Energy Technol.* **2020**, *8*, 1801169, doi:10.1002/ente.201801169.

139. Hawley, W.B.; Li, J. Electrode manufacturing for lithium-ion batteries—Analysis of current and next generation processing. *Journal of Energy Storage* **2019**, *25*, 100862, doi:10.1016/j.est.2019.100862.

140. Bauer, W.; Nötzel, D. Rheological properties and stability of NMP based cathode slurries for lithium ion batteries. *Ceramics International* **2014**, *40*, 4591–4598, doi:10.1016/j.ceramint.2013.08.137.

141. Sliz, R.; Valikangas, J.; Silva Santos, H.; Vilmi, P.; Rieppo, L.; Hu, T.; Lassi, U.; Fabritius, T. Suitable Cathode NMP Replacement for Efficient Sustainable Printed Li-Ion Batteries. *ACS Appl. Energy Mater.* **2022**, *5*, 4047–4058, doi:10.1021/acsaem.1c02923.

142. El Khakani, S.; Verdier, N.; Lepage, D.; Prébé, A.; Aymé-Perrot, D.; Rochefort, D.; Dollé, M. Melt-processed electrode for lithium ion battery. *Journal of Power Sources* **2020**, *454*, 227884, doi:10.1016/j.jpowsour.2020.227884.

143. Astafyeva, K.; Dousset, C.; Bureau, Y.; Stalmach, S.-L.; Dufour, B. High Energy Li-Ion Electrodes Prepared via a Solventless Melt Process. *Batteries & Supercaps* **2020**, *3*, 341–343, doi:10.1002/batt.201900187.

144. Wang, C.; Sakai, T.; Watanabe, O.; Hirahara, K.; Nakanishi, T. All Solid-State Lithium-Polymer Battery Using a Self-Cross-Linking Polymer Electrolyte. *Journal of the Electrochemical Society* **2003**, *150*, A1166-A1170, doi:10.1149/1.1593652.

145. Borghini, M.C.; Mastragostino, M.; Passerini, S.; Scrosati, B. Electrochemical Properties of Polyethylene Oxide - Li [(CF 3 SO 2) 2 N] - Gamma - LiAlO2 Composite Polymer Electrolytes. *J. Electrochem. Soc.* **1995**, *142*, 2118–2121, doi:10.1149/1.2044260.

146. *Der gleichläufige Doppelschneckenextruder*: *Grundlagen, Technologie, Anwendungen;* Kohlgrüber, K., Ed., 2., neu bearbeitete und erweiterte Auflage; Hanser: München, 2016, ISBN 9783446435971.

147. Koltzenburg, S.; Maskos, M.; Nuyken, O.; Mülhaupt, R. *Polymere: Synthese, Eigenschaften und Anwendungen;* Springer Berlin Heidelberg; Imprint: Springer Spektrum: Berlin, Heidelberg, 2014, ISBN 978-3-642-34772-6.

148. Alfonso, G.C.; Russell, T.P. Kinetics of crystallization in semicrystalline/amorphous polymer mixtures. *Macromolecules* **1986**, *19*, 1143–1152, doi:10.1021/ma00158a036.

149. Magill, J.H. Review Spherulites: A personal perspective. *JOURNAL OF MATERIALS SCIENCE* **2001**, 3143–3164, doi:10.1023/A:1017974016928.

150. Vrandečić, N.S.; Erceg, M.; Jakić, M.; Klarić, I. Kinetic analysis of thermal degradation of poly(ethylene glycol) and poly(ethylene oxide)s of different molecular weight: Bearbeitet. *Thermochimica Acta* **2010**, *498*, 71–80, doi:10.1016/j.tca.2009.10.005.

151. Marzantowicz, M.; Dygas, J.R.; Krok, F.; Florjańczyk, Z.; Zygadło-Monikowska, E. Influence of crystallization on dielectric properties of PEO:LiTFSI polymer electrolyte. *Journal of Non-Crystalline Solids* **2006**, *352*, 5216–5223, doi:10.1016/j.jnoncrysol.2006.02.161.

152. Marzantowicz, M.; Dygas, J.R.; Krok, F.; Łasińska, A.; Florjańczyk, Z.; Zygadło-Monikowska, E.; Affek, A. Crystallization and melting of PEO:LiTFSI polymer electrolytes investigated simultaneously by impedance spectroscopy and polarizing microscopy. *Electrochimica Acta* **2005**, *50*, 3969–3977, doi:10.1016/j.electacta.2005.02.053.

153. Lascaud, S.; Perrier, M.; Vallee, A.; Besner, S.; Prud'homme, J.; Armand, M. Phase Diagrams and Conductivity Behavior of Poly(ethylene oxide)-Molten Salt Rubbery Electrolytes. *Macromolecules* **1994**, *27*, 7469–7477, doi:10.1021/ma00103a034.

154. Mindemark, J.; Lacey, M.J.; Bowden, T.; Brandell, D. Beyond PEO—Alternative host materials for Li + -conducting solid polymer electrolytes. *Progress in Polymer Science* **2018**, *81*, 114–143, doi:10.1016/j.progpolymsci.2017.12.004.

155. *Co-rotating twin-screw extruders*: *Applications;* Kohlgrüber, K., Ed.; Hanser Publishers; Hanser Publications: Munich, Cincinnati, 2021, ISBN 978-1-56990-781-8.

156. Devaux, D.; Bouchet, R.; Glé, D.; Denoyel, R. Mechanism of ion transport in PEO/LiTFSI complexes: Effect of temperature, molecular weight and end groups. *Solid State Ionics* **2012**, *227*, 119–127, doi:10.1016/j.ssi.2012.09.020.

157. Kim, G.T.; Appetecchi, G.B.; Carewska, M.; Joost, M.; Balducci, A.; Winter, M.; Passerini, S. UV cross-linked, lithium-conducting ternary polymer electrolytes containing ionic liquids. *Journal of Power Sources* **2010**, *195*, 6130–6137, doi:10.1016/j.jpowsour.2009.10.079.

158. Graebe, H.; Netz, A.; Baesch, S.; Haerdtner, V.; Kwade, A. A Solvent-Free Electrode Coating Technique for All Solid State Lithium Ion Batteries. *ECS Trans.* **2017**, *77*, 393–401, doi:10.1149/07711.0393ecst.

159. Maurel, A.; Armand, M.; Grugeon, S.; Fleutot, B.; Davoisne, C.; Tortajada, H.; Courty, M.; Panier, S.; Dupont, L. Poly(Ethylene Oxide)−LiTFSI Solid Polymer Electrolyte Filaments for Fused Deposition Modeling Three-Dimensional Printing. *J. Electrochem. Soc.* **2020**, *167*, 70536, doi:10.1149/1945-7111/ab7c38.

160. Abels, G. *Grenzschichtverhalten von Polymerelektrolyten gegenüber Elektrodenmaterialien für zukünftige Hochenergie-Lithium-Ionen Sekundärbatterien*. PhD Dissertation; Universität Bremen, 2022.

161. Wu, M.; Sun, D.; Zhang, T.; Zhou, C.; Zhang, B. Study on the Function of Conveying, Kneading Block and Reversing Elements on the Mixing Efficiency and Dispersion Effect inside the Barrel of an Extruder with Numerical Simulation. *Foods* **2023**, *12*, doi:10.3390/foods12183503.

Appendix A

Karl-Fischer-Titration of produced PEO-based electrolytes

Table 6: Water content of the extruded pre-mixed PEO-based electrolytes dependent on screw design and screw speed

Screw design	**5 rpm** water content [ppm]	**10 rpm** water content [ppm]	**15 rpm** water content [ppm]
A	502 ± 45	834 ± 121	782 ± 38
B	764 ± 75	452 ± 88	533 ± 124
C	720 ± 26	409 ± 18	843 ± 59

Table 7: Water content of the extruded PEO-based electrolytes using two feeders dependent on screw design and screw speed.

Screw design	**5 rpm** water content [ppm]	**10 rpm** water content [ppm]	**15 rpm** water content [ppm]
A	205 ± 1	152 ± 21	159 ± 19
B	126 ± 4	435 ± 26	450 ± 33
C	676 ± 33	569 ± 20	388 ± 16

Appendix A. Karl-Fischer-Titration of produced PEO-based electrolytes

Appendix B

Electrochemical characterization

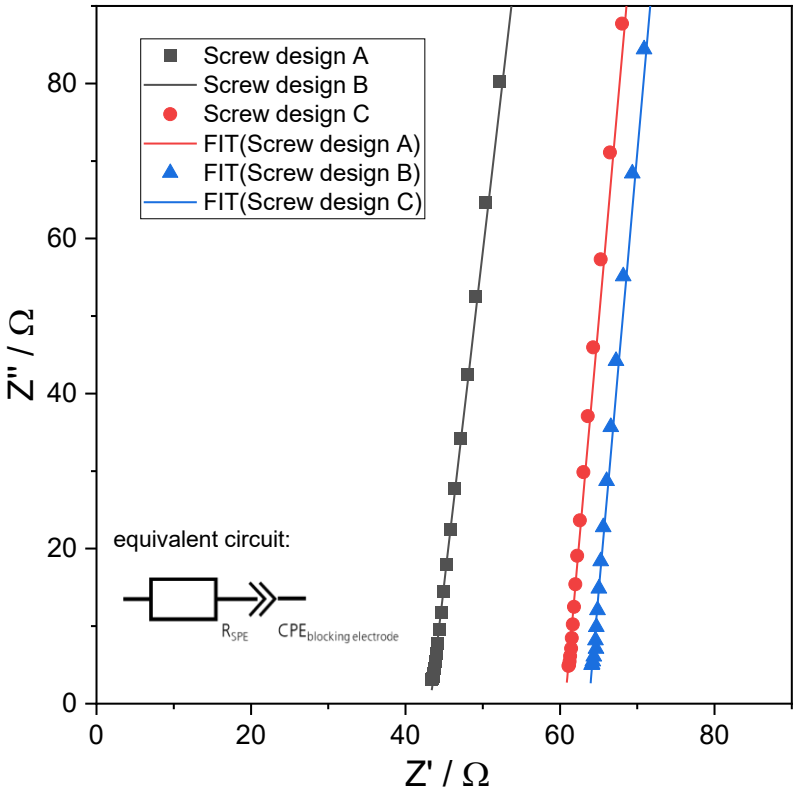

Figure 47: Exemplary Nyquist plot of impedance measurement of PEO-based electrolytes at 80 °C extruded with different screw designs and an applied screw speed of 5 rpm from E1.

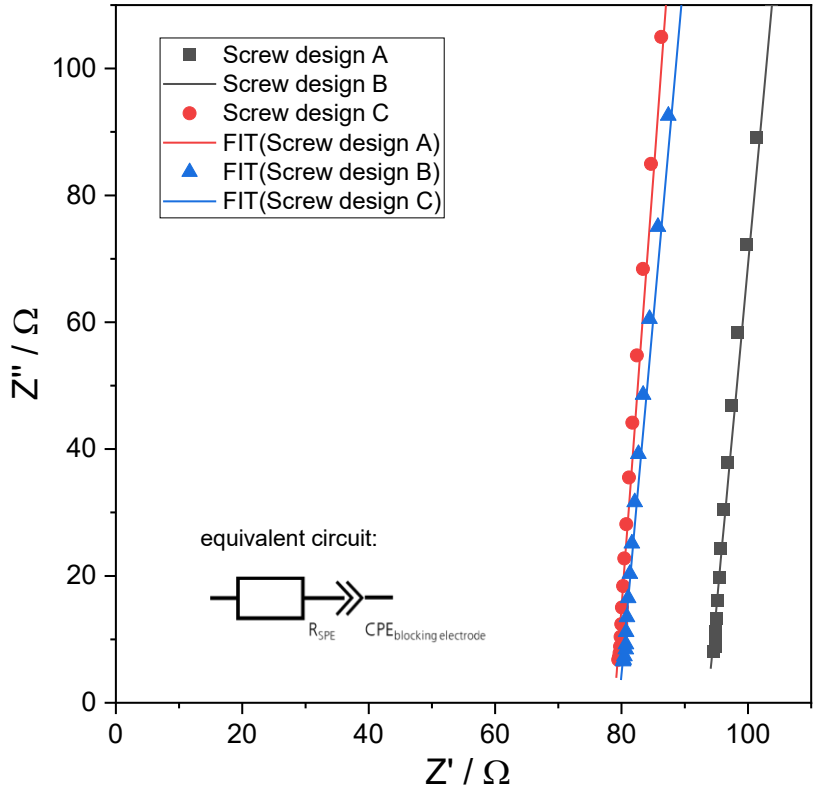

Figure 48: Exemplary Nyquist plot of impedance measurement of PEO-based electrolytes at 80 °C extruded with different screw designs and an applied screw speed of 10 rpm from E1.

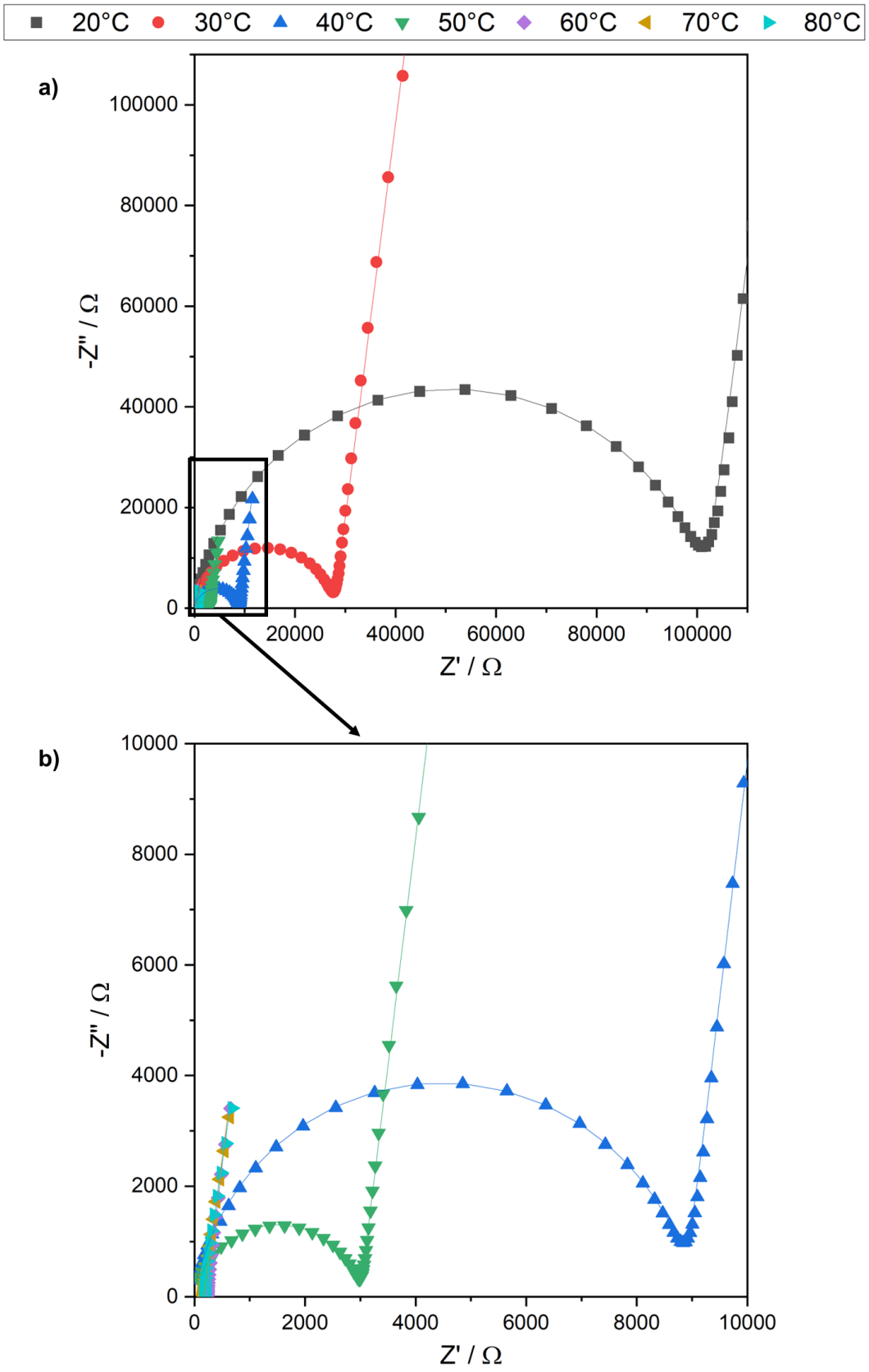

Figure 49: Temperature-dependent Nyquist plot of impedance measurement of PEO-based electrolytes extruded with screw designs A and an applied screw speed of 10 rpm from E2.

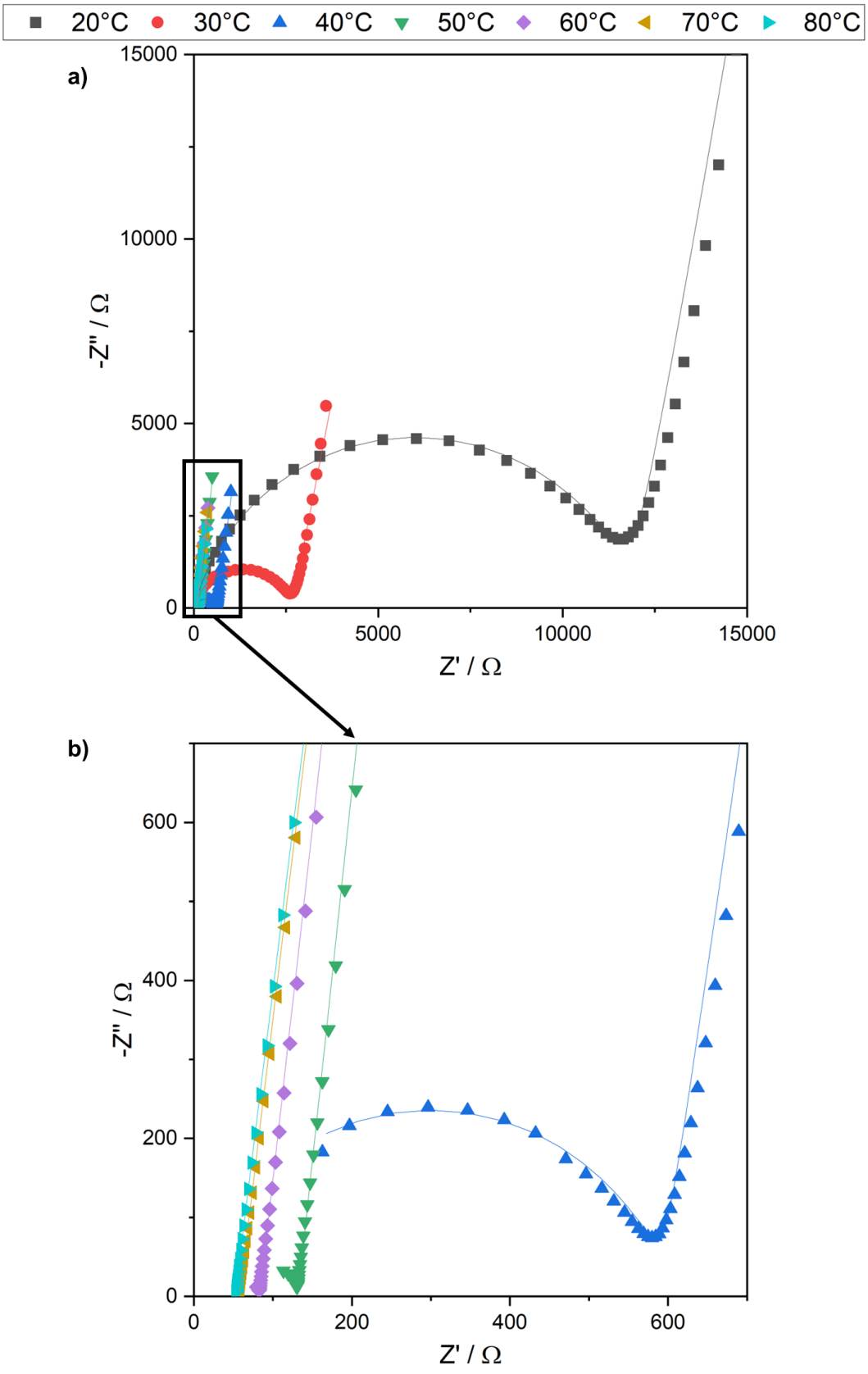

Figure 50: Temperature-dependent Nyquist plot of impedance measurement of PEO-based electrolytes extruded with screw designs A and an applied screw speed of 10 rpm from E2.

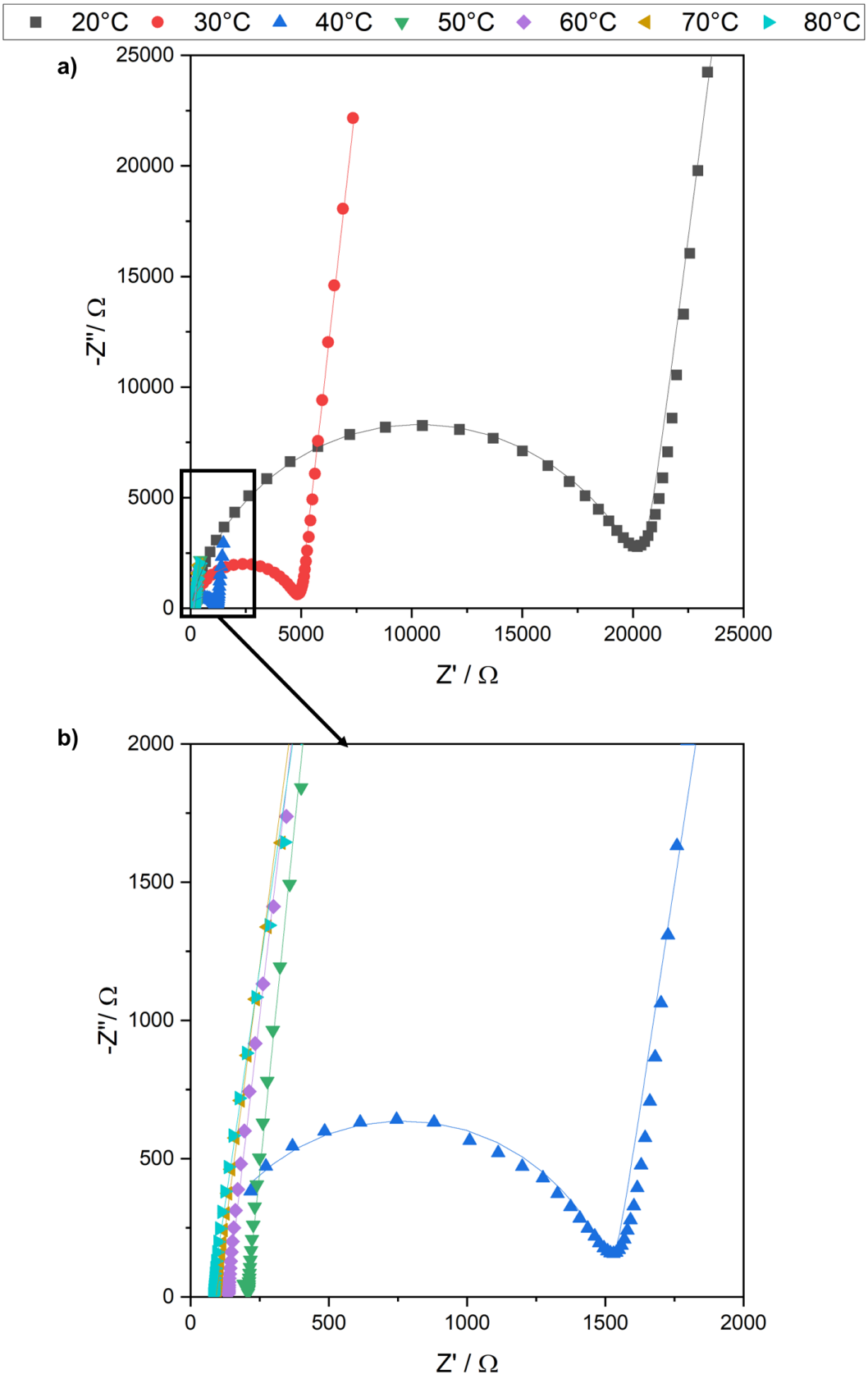

Figure 51: Temperature-dependent Nyquist plot of impedance measurement of PEO-based electrolytes extruded with screw designs B and an applied screw speed of 5 rpm from E2.

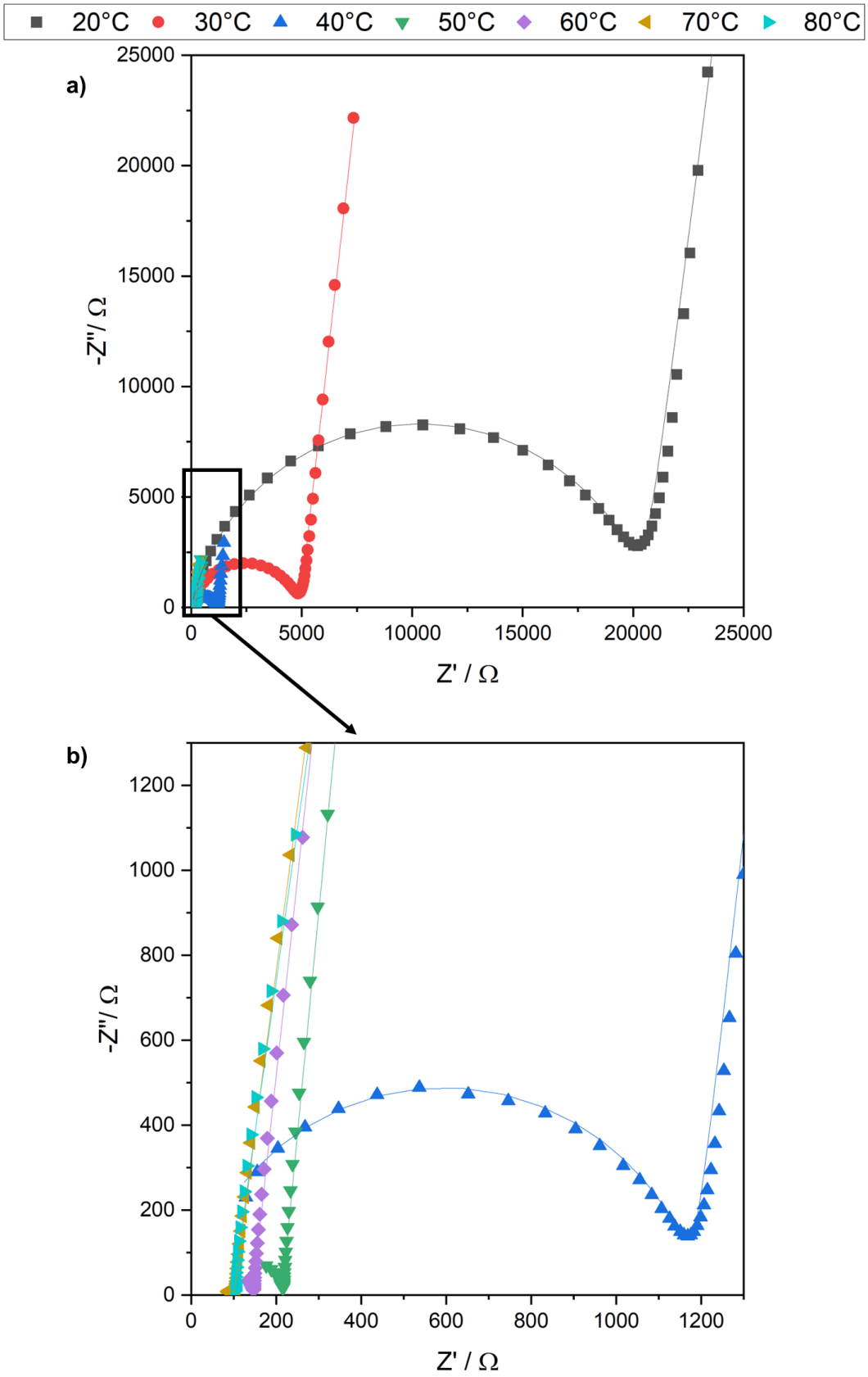

Figure 52: Temperature-dependent Nyquist plot of impedance measurement of PEO-based electrolytes extruded with screw designs B and an applied screw speed of 10 rpm of E2.

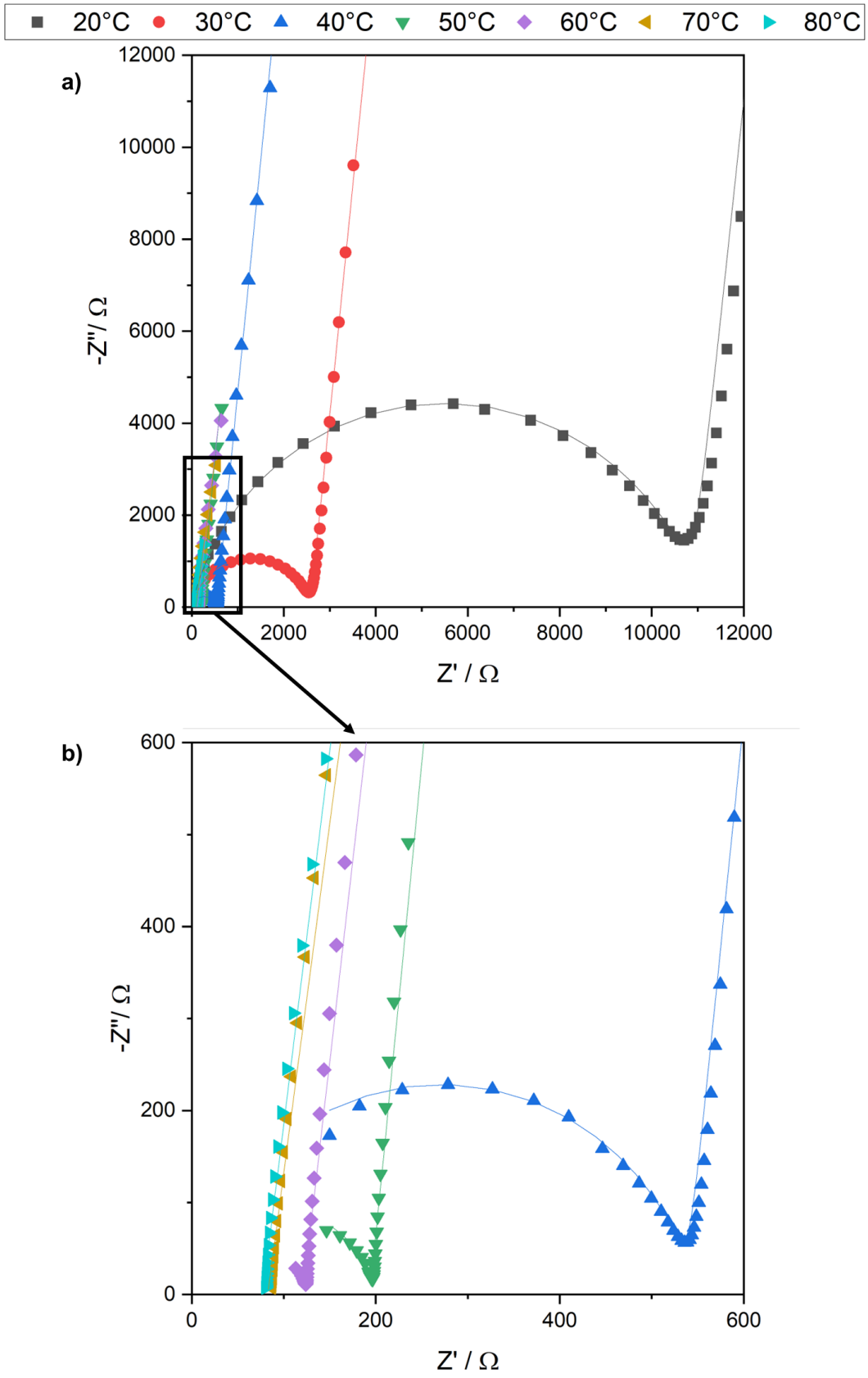

Figure 53: Temperature-dependent Nyquist plot of impedance measurement of PEO-based electrolytes extruded with screw designs B and an applied screw speed of 15 rpm of E2.

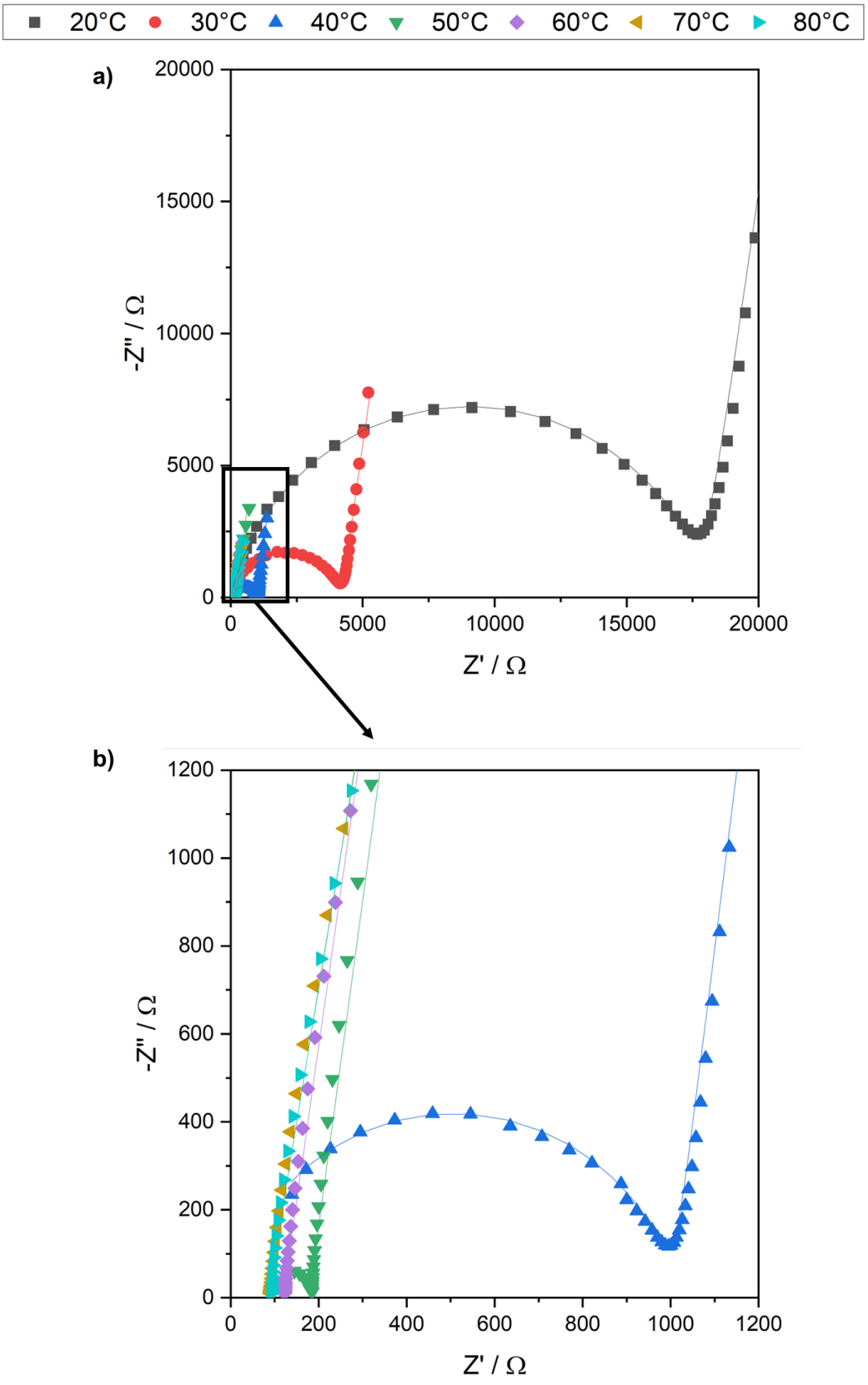

Figure 54: Temperature-dependent Nyquist plot of impedance measurement of PEO-based electrolytes extruded with screw designs C and an applied screw speed of 5 rpm of E2.

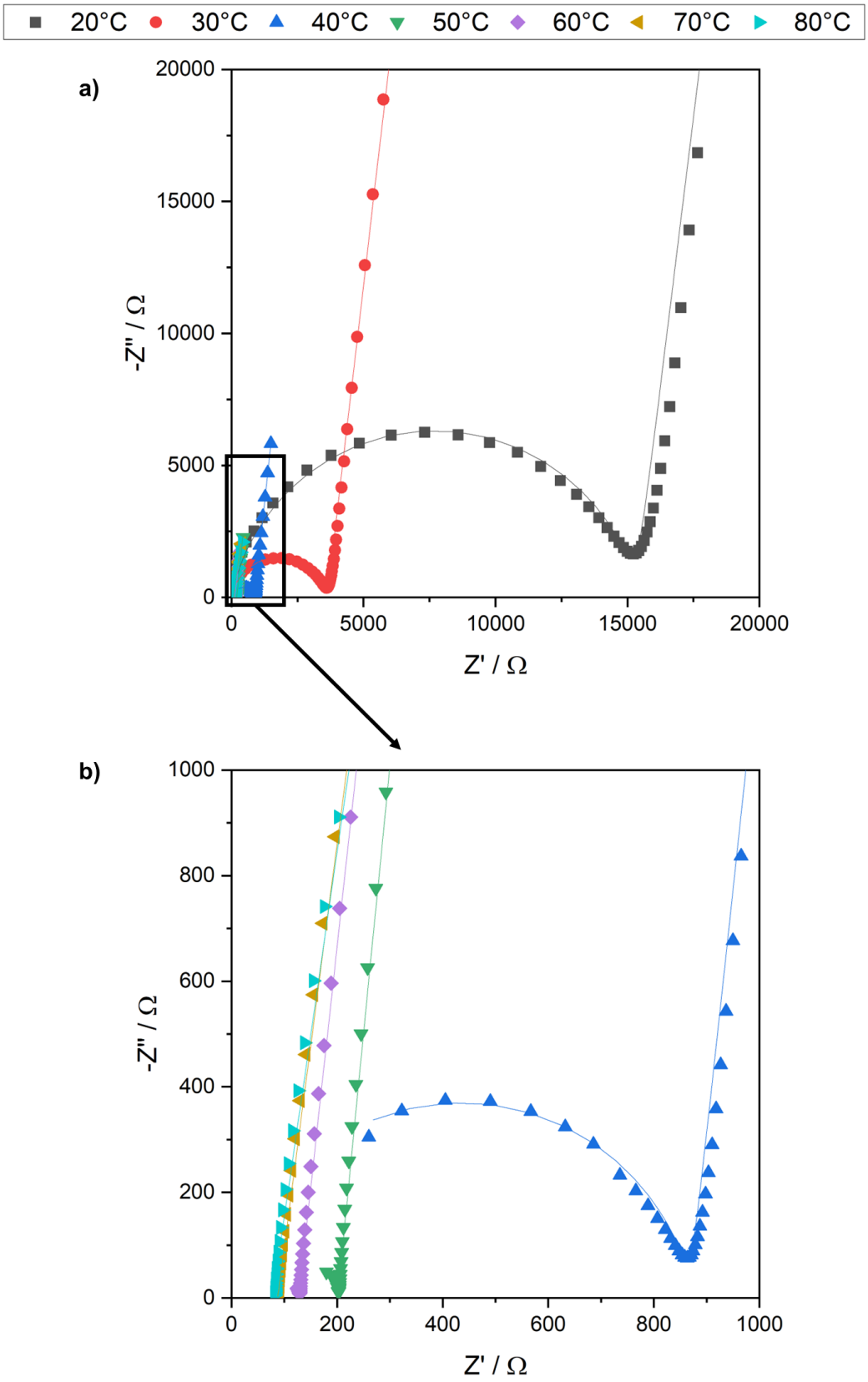

Figure 55: Temperature-dependent Nyquist plot of impedance measurement of PEO-based electrolytes extruded with screw designs C and an applied screw speed of 10 rpm of E2.

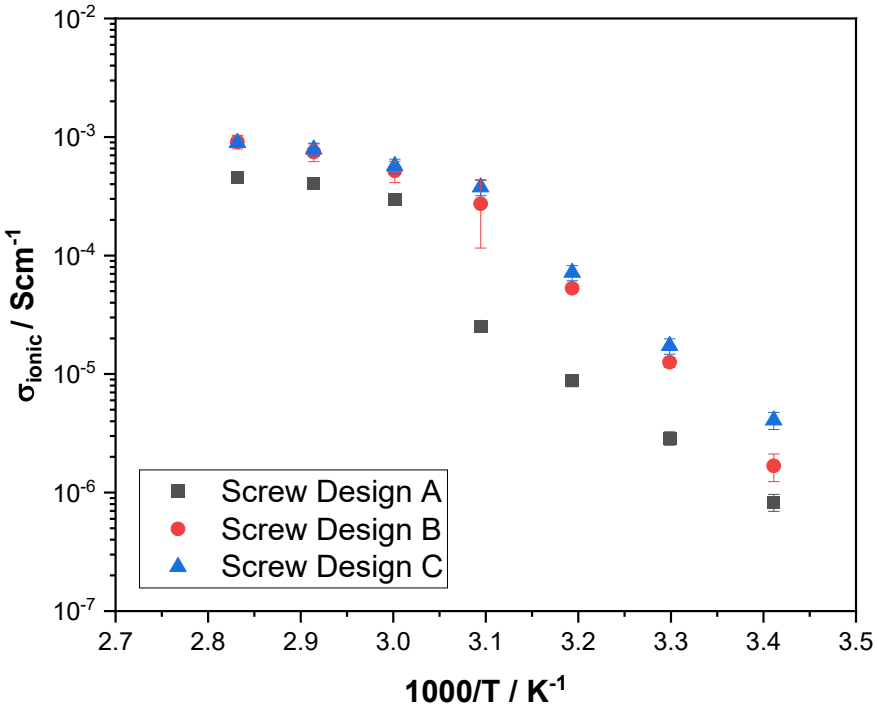

Figure 56: Arrhenius plot of extruded PEO-based electrolytes of E2 with different screw design exemplary for 5 rpm of E2.

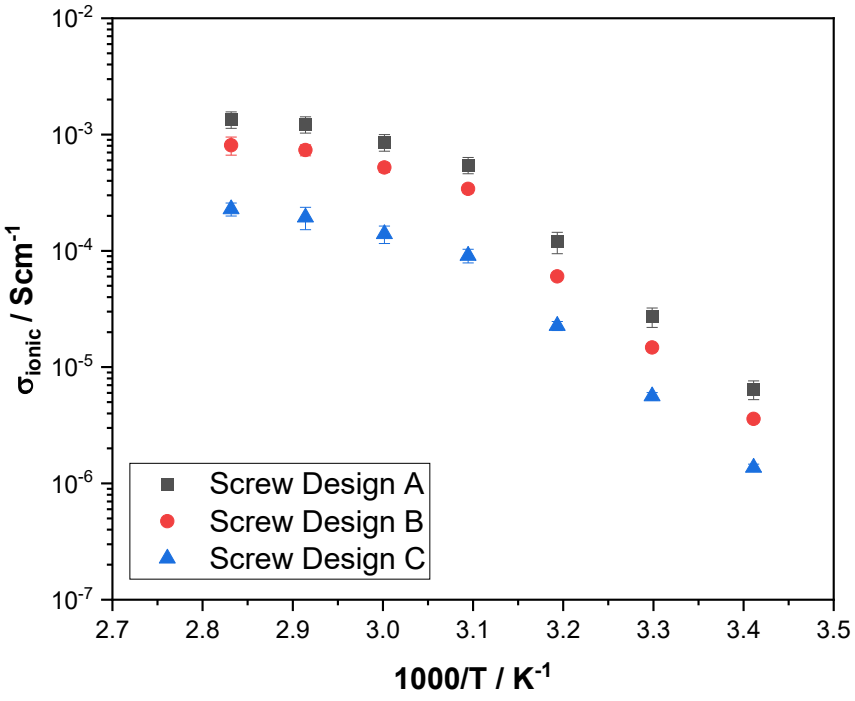

Figure 57: Arrhenius plot of extruded PEO-based electrolytes of E2 with different screw design exemplary for 10 rpm of E2.

Publications

Parts of this thesis have been published in the following peer-reviewed scientific journals.

1. K. Platen, F. Langer, R. Bayer, R. Hollmann, J. Schwenzel, M. Busse: Influence of molecular weight and Lithium bis(trifluoro-2 methanesulfonyl)imide on the thermal processability of 3 Poly(ethylene oxide) for solid-state electrolytes, Polymers, 2023, *15*(16), 3375.

2. K. Platen, F. Langer, J. Schwenzel: Influence of Screw Design and Process Parameters on the Product Quality of PEO:LiTFSI Solid Electrolytes using Solvent-Free Melt Extrusion, Batteries, **2024**, 10(*6*), 183.